CONTROL APPLICATIONS TO BIOFUEL ENGINES

By

Xuefei Chen

A DISSERTATION

Submitted to
Michigan State University
in partial fulfillment of the requirements
for the degree of

DOCTOR OF PHILOSOPHY

Mechanical Engineering

2012

ABSTRACT

CONTROL APPLICATIONS TO BIOFUEL ENGINES

BY

Xuefei Chen

Biofuel, a form of renewable fuel, has a promising future, especially as an alternative fuel for transportation. Biofuel is usually blended with petroleum fuel and used in flex fuel engines. Since the characteristics of biofuel are quite different from those of the petroleum based fuel, it is very important to optimize the combustion properties for biofuel engines under different fuel blends. This research focuses on biofuel content detection and combustion control of biofuel engines under different biofuel contents.

The first part of this research is the utilization of the ionic polymer-metal composite (IPMC) material as a sensing element of a flow and fluid property sensor for flex fuel engines. This research is motivated by the IPMC's intrinsic sensing characteristic that an IPMC beam is capable of producing an electric signal closely correlated to its mechanical movement due to the redistribution of mobile ions inside the IPMC material. The IPMC beam is modeled as multiple rigid elements connected by rotational springs and dampers in this study. The fluid properties are estimated by using the least-squares approach based upon the developed finite element model. The proposed estimation scheme was validated in experiments under different fluid media, and it was found that the estimated fluid properties have fairly good agreement with their actual values. This research is very important for automotive applications where the characteristics of the fuel blend need to be identified in real time.

The second part of the research is targeted at the optimal tracking control of the desired air-to-fuel ratio (AFR) based upon adaptively estimated biofuel content for internal combustion

engines equipped with lean NOx trap (LNT) aftertreatment systems. The biofuel content is adaptively estimated based upon the oxygen sensor signal. The engine system was approximated by a third order linear system. A linear quadratic optimal tracking controller was developed to track the desired engine AFR during the LNT regeneration period. The robust stability of the closed loop system with the biofuel content estimation is guaranteed over the entire biofuel content range by using the robust stability criteria for the LPV (linear parameter variation) system, where the biofuel gain and the engine speed are considered as the variable parameters. Several adaptive control schemes were studied through simulations, and then the selected control strategies were evaluated through dynamometer tests for a lean burn spark ignition (SI) engine. The best performance was achieved by the gain-scheduled adaptive scheme.

The third part of the research is detection of the combustion phase and estimation of biodiesel content using traditional knock sensors. Existing approaches for the combustion phase detection of a diesel engine are mainly based upon the high cost in-cylinder pressure sensor. This study focuses on developing a method to estimate the point of 75% of mass faction burned (MFB75) by using the traditional knock sensor signal. It was observed through experimental data that the knock signal can be correlated to MFB75 location well. Therefore, an MFB75 estimation method was proposed based upon the integrated knock signal over each crank angle. The proposed approach was validated using the experimental data and consistently provided accurate estimation of MFB75. In addition, the study also demonstrates the feasibility of using the knock sensor signal to provide a secondary estimation of fuel content.

TO MY PARENTS AND FAMILY

ACKNOWLEDGEMENTS

Four years ago, a mail contained an offer was sent to me. Four years later, a Ph.D dissertation is about completed. Four year is a long journey, because it consists of a lot of hard work; four year is also a short ride, because I have not got enough time to enjoy the happiest and best time that we shared together yet. But it is time to express my heartfelt appreciations to those who helped me during my journey of the four year PhD study.

First and foremost, I want to thank my advisor Dr. Guoming Zhu. To me, he is not only my advisor, but one of my best friends. I just could not have enough words to express my gratitude to him for everything he did for me. The completion of this dissertation would be impossible without his patient guidance and continuous support for my research, as well as his help for my life. I just could not image having a better advisor for my Ph.D study, and a better mentor for my life.

I would also like to express my profound gratitude to my committee members: Dr. Elias Strangas, Dr. Jonguen Choi, and Dr. Harold Schock, for their helpful discussions and insightful comments during my dissertation work, as well as their knowledge shared with me during their lectures and meetings that were essential for me to make progress throughout my PhD program. It is my great honor to have this committee.

My sincere thanks also go to Dr. Xiaobo Tan, Dr. Yueyun Wang, and Dr. Ibrahim Haskara. They gave me a lot of constructive suggestions during my academic research. It is my honor to work with them.

Further appreciations are extended to past and current students and other lab personnel who helped me considerably with many aspects of my research work: Xiaojian Yang, Zhen Ren, Andrew White, Stephen Pace, Andrew Huijen, Cody Squibb, Peter Dolce, Taotao Jin, Ping Mi, Shupeng Zhang, Jie Yang, Yingxu Wang, Chao Cheng, Tom Stuecken, Kevin Moran, Gary Keeny, Jeff Higel, Trevor Ruckle, Edward Timm, Elisa Toulson, Aida Montalvo, and Melissa Jopke.

Of course, special thanks should be sent to my parents and my wife, for their never-ending love and encouragement. I love them so much. I would not make this far without them. I also want to dedicate this dissertation to my precious daughter, Amy Chen, and wish her a splendid future.

TABLE OF CONTENTS

LIST OF TABLES

LIST OF FIGURES

KEY TO ABBREVIATIONS

Symbol	Description
IPMC	Ionic polymer-metal composite
AFR	Air-to-fuel ratio
LNT	Lean NOx trap
LPV	Linear parameter variations
SI	Spark ignition
MFB	Mass fraction burned
HHV	Higher heating value
SOC	Start of combustion
LQG	Linear quadratic Gaussian
EMS	Engine management system
MAF	Mass air flow
MAP	Manifold air pressure
K_i	Rotational stiffness (K_e) on i^{th} joint
H_i	Rotational damping (H_e) on i^{th} joint
J_i	Moment of inertia (J_e) of i^{th} beam element
θ_i	Absolute angular displacement (θ) of i^{th} beam element
$\dot{\theta}_i$	Absolute angular velocity ($\dot{\theta}$) of i^{th} beam element
$\ddot{\theta}_i$	Absolute angular acceleration ($\ddot{\theta}$) of i^{th} beam element
a_{ix}	Acceleration of i^{th} beam element in x direction

a_{iy}	Acceleration of i^{th} beam element in y direction
F_{ix}	Reaction force on i^{th} joint in x direction
F_{iy}	Reaction force on i^{th} joint in y direction
m_i	Effective mass of i^{th} beam element
l	Beam element length
b	Beam element width
c	Beam element thickness
ρ_e	Beam element effective density
ρ	Fluid density
V_0	Fluid velocity
V_{xi}	Linear velocity of i^{th} beam element (V_i) in x direction
$\hat{V}_i$	Beam velocity of i^{th} beam element relative to fluid velocity
V_{tip}	Beam tip velocity
i_{short}	Beam short-circuit current signal
P_{bi}	i^{th} mode shape (P_b, coordinate transformation matrix)
w_i	i^{th} mode frequency
R_e	Reynolds number
PM	Particulate matter
$\dot{m}_{fuel}$	Fuel mass
$\dot{\hat{m}}_{air}$	Measured air charge mass
$\hat{\alpha}$	Estimated fuel gain (α)

$\underline{\alpha}$	Lower bound of the estimated fuel gain (α)
$\bar{\alpha}$	Upper bound of the estimated fuel gain (α)
Φ	Equivalence fuel-to-air ratio
σ_{DS}	Stoichiometric air-to-fuel ratio
λ	Normalized air-to-fuel ratio
σ_{DS}	Stoichiometric air-to-fuel ratio for petroleum based fuel
σ_{BD}	Stoichiometric air-to-fuel ratio for biofuel blend
τ_1	Time constant for the transport delay
τ_2	Time constant for exhaust manifold filling dynamics
τ_3	Time constant for the oxygen sensor dynamics
Γ	Adaptive control gain
Γ_b	Torque vector induced by the fluid flow
ε_{air}	Air mass estimation error
δ	Uncertainty introduced by the estimation error of the fuel gain and air
τ_{id}	Ignition delay
P_a	In-cylinder pressure
T_a	In-cylinder temperature
E_a	Activation energy
R_u	Universal gas constant
CN	Cetane number
EGR	Exhaust gas recirculation
IMEP	Indicated mean effective pressure

BTDC	Before top dead center
ATDC	After top dead center
MAD	Mean absolute deviation
B0	Petroleum diesel
B50	Fifty percent biodiesel
B100	One hundred percent biodiesel

CHAPTER 1 INTRODUCTION

1.1 Background and Motivation

Today, eighty-five percent of the world's energy demand is provided by fossil fuels [1]. The critical consequences of the future energy supply shortage and environmental degradation (climate change and air pollution) have motivated many nations to develop and use renewable fuels (biofuels), such as ethanol and biodiesel. The advantages of utilizing biofuels stem from the fact that biofuels are mainly produced from large, under-utilized biomass resources that are sustainable and renewable in a closed carbon cycle that reduces environment impact. For example, today, ethanol is made from starches and sugars, while biodiesel is made from vegetable oil, animal fat, or recycled cooking grease [2].

For automotive engine applications, biofuel is mostly used in flex fuel engines and as blending agent with gasoline or diesel, for example, E85 contains 85% of ethanol with 15% gasoline, and B20 contains 20% of biodiesel with 80% of petroleum-based diesel. Since the energy density and the combustion characteristic for different fuels vary from fuel to fuel, (the higher heating value (HHV) of biodiesel is 39-41 MJ/kg, 46MJ/kg for gasoline, 43MJ/kg for petrodiesel [3],) it is very important to detect the fuel content for flex fuel engines, so that the control system can optimize the combustion by adjusting the fuel quantity, fuel injection timing, and so on.

Researchers have studied several approaches to estimate the biofuel content. For example, the oxygen sensor signal was used to detect the fuel content in [4]-[6], the in-cylinder pressure signal can also be used to detect fuel information [7], as well as the ionization signal [8]. In this research, an ionic polymer-metal composite (IPMC) beam fuel flow sensor was developed to detect the fuel content by identifying the fuel viscosity based upon the fact that different fuels have different fluid viscosities. It is motivated by the unique characteristic of IPMC beam, which is capable of producing an electric signal closely correlated with its mechanical movement [9]-[10]. The other advantage of the IPMC beam flow sensor is that it also has the potential ability of detecting fuel flow rate close to fuel injector location, which is critical for accurate air-to-fuel ratio (AFR) control.

Currently, most engine control systems rely on the oxygen sensor signals to regulate the AFR [7]. The AFR on gasoline engines is usually maintained at stoichiometric level through closed loop control, while the AFR usually runs in open loop operation on diesel or lean burn engines. In order to meet the emission regulation for lean burn engines equipped with the lean NOx trap (LNT) aftertreatment systems [11], there is a period of LNT regeneration. During the regeneration period, the AFR is controlled in a closed loop [12]. The second part of this research presented an optimal control method of tracking the desired AFR based upon the adaptively estimated biofuel content during the LNT regeneration for lean burn flex fuel engines.

With the specific emphasis on biodiesel, detecting the combustion phase of diesel engines is of great interest to researchers, because the combustion phase directly determines the combustion efficiency and the exhaust emissions of diesel engines, as well as its indirect effect on engine noise and pollutant formation [13]. Most studies have concentrated on the estimation of the start of combustion (SOC), which occurs shortly after the fuel injection. However, the SOC is very difficult to determine precisely. The existing approaches for SOC detection have sensor based and mode based estimation schemes ([15], [18]). But none are currently available for practical application, because they either are too expensive, or have low predictive capability. In this research, the traditional knock sensor is proposed to be used for combustion phase detection, and instead of detecting the SOC, this research suggests to detect the 75% of mass fraction burned (MFB75) location, because the combustion signals at the MFB75 position are usually much stronger than those at the SOC.

1.2 Research Overview

1.2.1 Model-based estimation of flow characteristics using an IPMC beam

An ionic polymer-metal composite (IPMC) beam is capable of producing an electric signal closely correlated with its mechanical movement, due to the redistribution of mobile ions inside the IPMC material. Motivated by the potential application of this intrinsic sensing characteristic to flow property measurements in automotive engines, this research investigates the feasibility of detecting the start and end of a pulsating flow and its fluid characteristics using an IPMC beam-based sensor. A dynamic model was developed for the IPMC beam under fluid flow. The model consists of multiple rigid elements connected by rotational springs, and under suitable conditions, has a closed-form solution that enables efficient estimation of fluid properties and flow parameters with the least-squares minimization approach. The proposed fluid estimation scheme was validated using experimental results with different fluid media, and it was found that the estimated fluid drag coefficients, which are highly correlated to fluid viscosity, have good agreement with their actual values. This is very important for automotive applications where the characteristics of the fuel blend (such as gasoline and ethanol) need to be identified in real time.

1.2.2 AFR tracking with fuel content estimation for lean burn flex fuel engines

This research presents an optimal control method of tracking the desired air-to-fuel ratio (AFR) based upon the adaptively estimated biofuel content for internal combustion engines equipped with the lean NOx trap (LNT) aftertreatment system. The fuel content (or percentage of biofuel) is adaptively estimated based upon the exhaust oxygen (air-to-fuel ratio) sensor signal under both the normal engine operations with lean combustion and the LNT regeneration operations with the closed loop AFR control. The engine system was modeled as a third order linear system, a first order system for engine transportation delay, a first order system for exhaust manifold filling dynamics, and a first order system for oxygen sensor dynamics. A linear quadratic Gaussian (LQG) controller integrated with an integral control was developed to track the desired engine AFR during the LNT regeneration period based upon the Kalman state estimation. The robust stability of the closed loop tracking control system with the biofuel content estimation is guaranteed over the entire biofuel range by using the robust stability criteria for the LPV (linear parameter variation) system, where the biofuel content and the engine speed are considered as the variable parameters. Several adaptive control schemes were studied through simulations, and the selected control strategies were evaluated through dynamometer tests for a lean burn spark ignition (SI) engine. The best performance was achieved by using the gain-scheduled adaptive scheme.

1.2.3 Detecting MFB75 and biodiesel blend of a direct injection diesel engine by using knock sensor signal

The fuel efficiency and the exhaust emissions of a diesel engine directly depend on its combustion phase. Existing approaches for the combustion phase detection of a diesel engine are mainly based upon high cost in-cylinder pressure sensors. This study focuses on developing a method to estimate the point of 75% of mass faction burned (MFB75) by using a traditional knock sensor signal. It is motivated by the observation through experiment data that the knock signal can be correlated to MFB75 location well. The proposed MFB75 estimation approach mainly uses the information from the integration of the knock signal, which is an indicator of the knock intensity. It is observed that the knock intensity usually has abrupt increase around MFB75 location. Therefore, the difference of the knock integration over each crank angle is calculated and used to estimate the MFB75 point based upon certain principles proposed in this research. The proposed approach was validated using the experimental data. It was found that the proposed approach demonstrates consistent and accurate estimation capability of MFB75. In addition to the MFB75 estimation, the study also shows that the knock sensor signal can be used as a secondary estimation of fuel content.

1.3 Organization

This dissertation is organized as the following: Chapter 2 investigates the feasibility of detecting the start and end of pulsating flow property measurements and the fluid characteristics in automotive engines by using an IPMC beam-based sensor. Chapter 3 presents an optimal AFR tracking method based upon the adaptively estimated biofuel content for internal combustion engines equipped with lean NOx trap (LNT) aftertreatment systems. In Chapter 4, the combustion characteristics of biodiesels will be studied by using a knock sensor, along with an approach for closed-loop combustion in flex fuel diesel engine. The conclusions and the future works are addressed in Chapter 5.

CHAPTER 2 IPMC BEAM FUEL FLOW CHARACTERISTICS SENSING

2.1 Introduction

In order to improve engine fuel efficiency with reduced exhaust emissions, advanced sensor technologies are widely used for engine management systems (EMS). Prime examples of advanced sensors used in EMS are the mass air flow (MAF), manifold air pressure (MAP), in-cylinder ionization, and exhaust oxygen sensors. The mass air flow in the engine intake manifold and the exhaust oxygen fraction before the three way catalytic converter are used to control the fuel injection quantity to meet the desired air-to-fuel ratio requirement at the given engine load and speed condition, while the in-cylinder ionization sensor is used to provide the in-cylinder combustion information for feedback control [19], [20]. The existing flow sensors, especially the pulsating flow sensors, operate based upon the Coriolis effect, gear-type positive displacement, piston displacement, ultrasonic measurement, or pressure increase [21]. These technologies are capable of providing accurate laboratory-grade measurements in a well-controlled environment but are not suitable to be used in a production environment such as engine fuel systems.

With the application of the biofuels (such as ethanol and biodiesel) on the horizon, detecting the fuel flow and contents (e.g., blend fraction of gasoline and ethanol) becomes a critical technology for maximizing the engine efficiency with reduced emissions [21], [22]. This is because the combustion characteristics are quite different for different fuel contents. One approach used to estimate biofuel contents is to measure the fluid viscosity or drag coefficient since different biofuel blends have distinct viscosity values. It is desirable to obtain such measurements *in situ* and in real time. A key obstacle preventing existing lab-grade sensors from being used *in situ* is their sizes, calling for new, miniaturized flow sensors that are amenable to the integration with engine fuel systems. With the advances in new materials and microfabrication technologies, micro flow sensors have been developed based on a number of transduction principles, such as hot-wire anemometry [23], piezoresistivity [24], and capacitance change [25]. Miniaturized strain gages could also be potentially integrated with a beam structure [26], [27] for flow measurement.

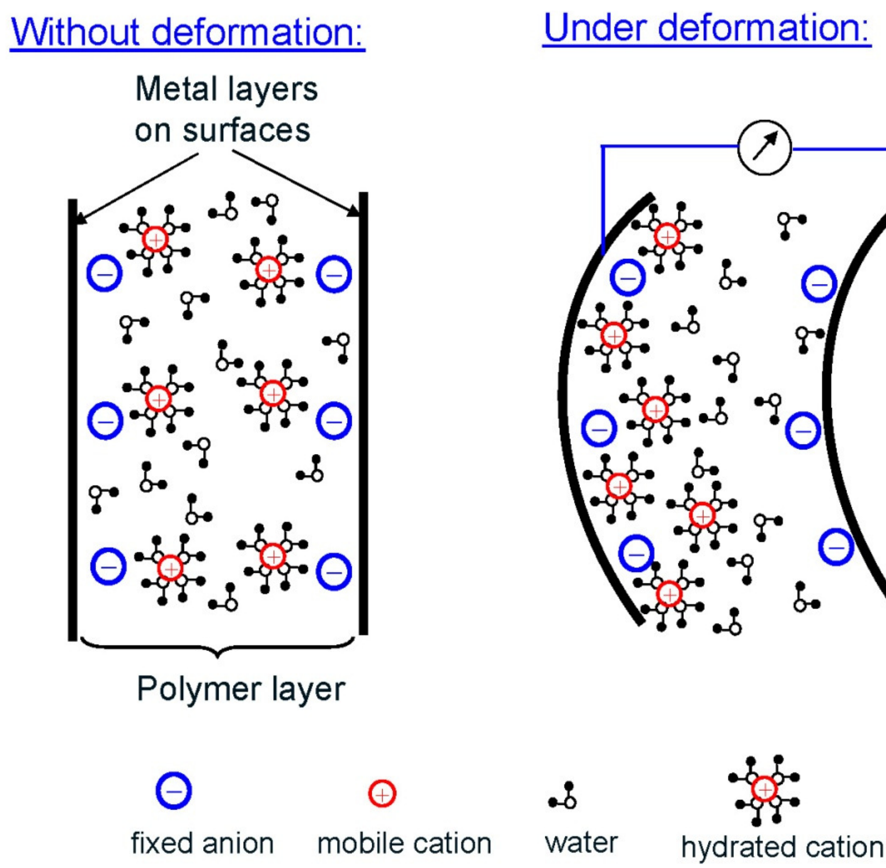

Figure 2-1 Illustration of the sensing mechanism of the IPMC material (For interpretation of the references to color in this and all other figures, the reader is referred to the electronic version of this dissertation)

In this research we propose the use of an ionic polymer-metal composite (IPMC) beam and a model-based estimation algorithm as a potential approach to *in-situ* measurement of flow properties. IPMC materials have intrinsic sensing and actuation characteristics [9], [10]. As illustrated in Figure 2-1, an IPMC has three layers, with an ion-exchange polymer membrane sandwiched by metal electrodes. Inside the polymer, (negatively charged) anions covalently fixed to polymer chains are balanced by mobile, (positively charged) cations. Deformation under a mechanical perturbation redistributes the cations, producing a detectable electric signal (short-circuit current) that is well correlated with the mechanical stimulus. Many researchers have studied the fabrication [28]-[30], characterization, and modeling [31]-[36] of IPMC sensors and actuators. There has also been proof-of-concept exploration of using IPMCs as mechanical sensors for force, pressure, displacement, and velocity measurement in medical applications, structural health monitoring, and robotics [37]-[42]. Recent years have seen significant interest in using IPMC materials for underwater actuation [43]-[51], sensing [37], [40], and energy harvesting [52], [53].

We have chosen the IPMC material for flow sensing in this work for several reasons. First, IPMC has direct mechanosensory property, which minimizes the complexity in both the sensor construction and the readout circuit. For example, its readout circuit is much simpler than that required for capacitive flow sensing. Low mechanical and electrical complexity in sensor construction will facilitate the adoption of IPMC in practical applications such as engine fuel systems. Another advantage related to the direct mechanosensory property is the relative ease in modeling the sensor beam dynamics, since we only need to consider a uniform IPMC beam. In contrast, a strain gage-based flow sensor will typically require embedding the gage in another structural beam, and such a hybrid structure will entail much more complex modeling, which hinders efficient model-based parameter estimation as proposed in this work. Another advantage of IPMC sensors is that, unlike hot-wire or piezoresistive sensors, they automatically capture the flow polarity. Finally, the softness of IPMC material allows it to respond to small flows and thus attain high measurement sensitivity.

This research focuses on the potential application of IPMC beams in detecting the start and end of pulsating flows as well as their fluid media characteristics in internal combustion engines. This application requires IPMC beams to respond to various fluid media differently. Therefore, a series of experiments was designed and conducted to study the characteristics of IPMC beams oscillating in different fluids. The test results show that the IPMC sensor output (short-circuit current) varies as the fluid medium changes, which indicates that the proposed IPMC sensor is able to distinguish different types of fluid media.

In order to extract flow information and fluid properties from the IPMC sensor output, an accurate dynamic model is required for an IPMC beam oscillating in a fluid medium. Modeling of the IPMC beam dynamics has been studied in the context of actuation [46]-[49]. To fully capture the flexible beam dynamics, an infinite-dimensional model is generally required. For practical implementation purposes, however, a finite-dimensional model is desirable. The latter can be achieved by considering the first few dominant vibration modes [46]-[48], or approximating a flexible beam with multiple, serially connected rigid elements [54]-[56]. While linear beam models are only applicable to small deformations, the multi-segment approach can effectively address large deformations with low computational complexity [56]. In addition, compared to the mode summation-based method [46], the latter approach can more easily accommodate nonlinear force terms such as the drag. Therefore, we have adopted the multi-segment modeling approach in this research.

Under appropriate conditions, we show that there exists a closed-form solution for the beam dynamics, and the solution is linear with respect to the fluid property (product of drag coefficient and fluid density) that we are interested in estimating. The correlation of the IPMC sensor output to the beam dynamics is provided in [32], where one can see that the sensor's output signal is approximately proportional to the beam tip velocity when the oscillation frequency is relatively low. Based on the solution for the beam tip velocity, a least-squares minimization procedure is taken to obtain the fluid property estimation, which is readily computed based on the measured IPMC sensing current. We have applied the approach to estimate the properties of different fluid media in pulsating flows, and the identified parameters demonstrate good agreement with their actual values.

The rest of this research is organized as follows. In Section 2.2 we present the IPMC sensing characteristics under different fluid media. In Section 2.3, the dynamic model for the IPMC beam is described. The parameter estimation approach using the least squares minimization is developed in Section 2.4, and experimental results are presented in Section 2.5. Conclusion and other discussions are provided in Section 2.6.

2.2 IPMC Sensor Characteristics in Flows

In this section, a series of experiments was performed to study the sensing behavior of an IPMC beam associated with a pulsating flow. We first describe the method for sensor fabrication and signal conditioning, and then present the results on characterizing the IPMC beam dynamics and its sensing response using high-speed imaging analysis. Finally, we show the IPMC sensor responses in pulsating flows of several different fluid media.

2.2.1 IPMC sensor: fabrication and sensing circuit

The IPMC used in this study was fabricated with Nafion-117, a commercial ion-exchange material from DuPont, by following the general ion-exchange and electroless electrode plating processes described in [29]. First, oxygen and argon plasma treatment was applied to roughen the surface of the Nafion film [57], followed by cleaning with boiling acid (HCl) and then with boiling deionized water (*sample preparation*). After these preparation steps, the sample was placed in $[Pt(NH_3)_4]Cl_2$ for over 3 hours to incorporate the platinum complex cations into the polymer (*ion-exchange*). Then, the reducing agent $NaBH_4$ was applied to the membrane in a water bath of 60 ˚C, which reduced the platinum complex ions to platinum near the membrane surfaces (*electrode plating*). The ion-exchange and electrode plating processes were repeated several times until the electrodes were sufficiently strong and thick, as indicated by the surface resistance. The final thickness of the IPMC was about 250 μm. Samples of desired lateral dimensions were then cut with a razor. Little pre-bending, if any, was observed for the samples used in the experiments.

Figure 2-2 shows the schematic of the circuit used to measure the short-circuit current of an IPMC sensor. The circuit uses a two-tier amplification scheme. The first operational amplifier (op-amp) converts the short-circuit current into a voltage, while the second op-amp provides gain adjustment through a tunable resistor. A low-noise, low-bias precision op-amp (OPA 124 from Texas Instruments) was adopted for the first-tier amplification, to reduce both the noise and the spurious DC bias in the sensor output. The measured spurious DC bias was about 0.0054 μA, which was negligible when compared to the actual sensing signals (order of μA) in our work. For Op-amp2 in Figure 2-2, a LM 324 from National Semiconductor was used. The output $v_2(t)$ is related to the current signal $i(t)$ via $v_2(t)=(R_3R_1/R_2)\ i(t)$. The components we used have the following values: R_1 = 470 kΩ, R_2 = 10 kΩ, and R_3 is adjustable from 0 to 50 kΩ.

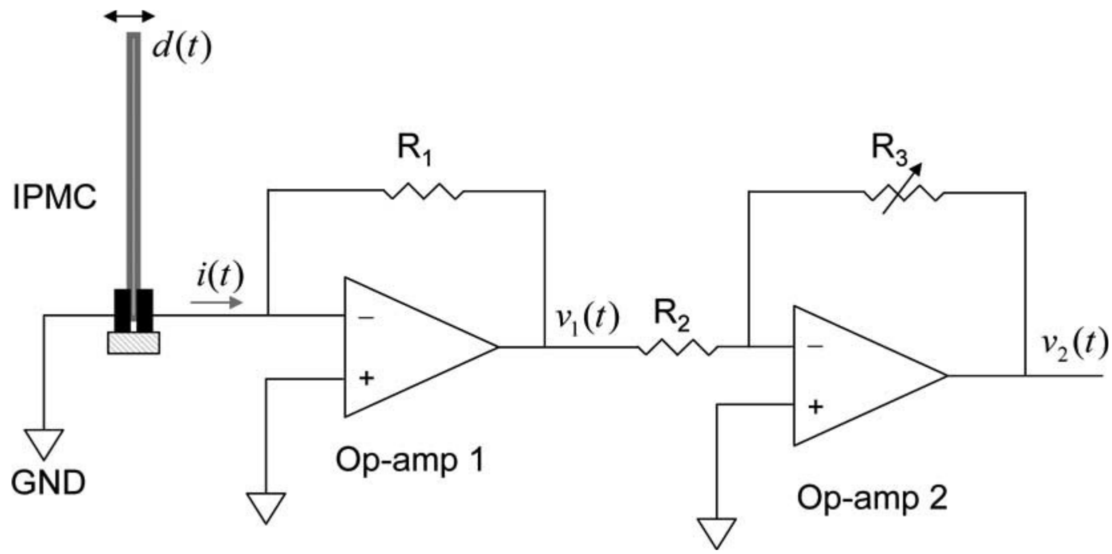

Figure 2-2 Schematic of the circuit for measuring short-circuit current output of an IPMC sensor

2.2.2 High-speed imaging-based characterization

Figure 2-3 shows the schematic of the setup for the high-speed imaging system. A high-speed camera (Photron, Model Fastcam APX RS) was used to record the horizontally vibrating IPMC beam at the rate of ten thousand frames per second. A high-repetition pulsed copper vapor laser (Oxford Lasers, Model LS20-50) was fired to illuminate the beam vibration. The visible laser illumination was directed to the IPMC beam via a fiber optic cable. The tip displacement of the IPMC beam was extracted from the images using an Optimas image processing analysis software. The sensor output response was taken from the short-circuit current measured between the two electrodes of the IPMC beam. A dSPACE system (dSPACE, DS1104) was used for data acquisition and processing.

Figure 2-4 shows the top view of a rectangular IMPC sample (long edge facing up) in the air medium. The dimensions of the beam were 26.9 mm by 4 mm by 0.25 mm (length by width by thickness). One end of the beam was securely clamped by a fixture, allowing the other end to freely vibrate. The cantilevered beam was initially rested at its default position along the beam axis. Then, it was perturbed manually with about 60 degrees clockwise from its default position.

As soon as the beam was released from that position, it oscillated around its base similar to a pendulum swinging around its pivot point. The entire swinging motion was recorded until it gradually returned back to its default position.

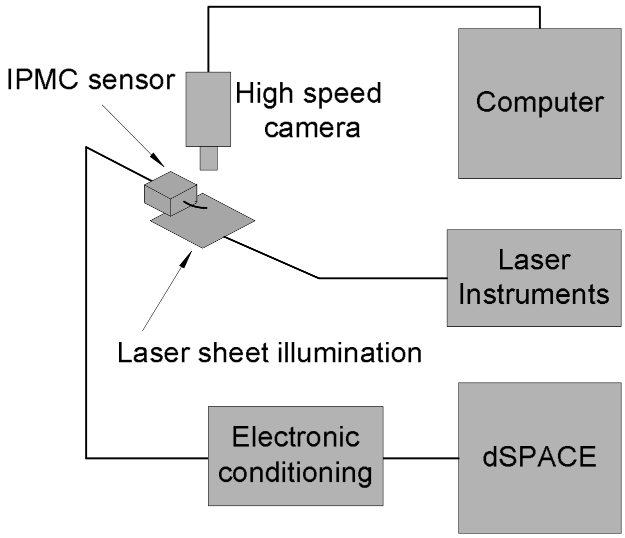

Figure 2-3 Schematic of the high-speed imaging system for characterizing IPMC beam behavior

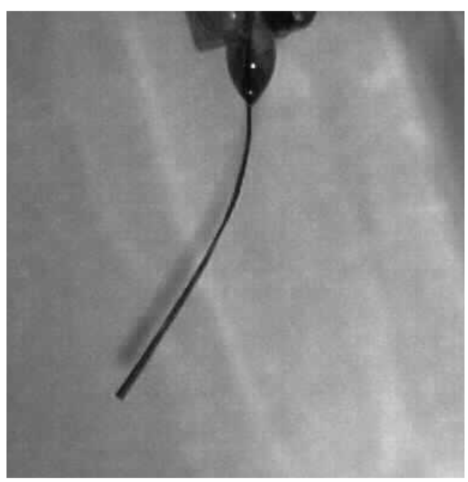

Figure 2-4 An IPMC cantilever beam used in high-speed imaging analysis

Figure 2-5 shows the snapshot images of the IPMC beam in a time sequence after it was released (at t = 0 s), between 0.1 and 0.4 s as the beam vibrated in stagnant air. Also shown in the figure are the trajectories of the tip displacement extracted from the images and the signal obtained by integrating the IPMC sensing current output. The period of the oscillation was about

0.044 second. It is evident that the beam was highly flexible under free vibrations. Due to the slight dissipation in air and the damping in the beam, the peak displacement slowly diminished until the beam finally returned to its rest position; and the peak of the integrated short-circuit current decreased in a similar fashion as the amplitude of the oscillation diminished over time. It can be observed that the integrated short-circuit current correlates very well with the beam tip displacement. This confirms that, at relatively low frequencies, the tip velocity of the IPMC beam can be approximately related to the current output through a static gain, as implied by the physics-based dynamic model for IPMC sensors [32].

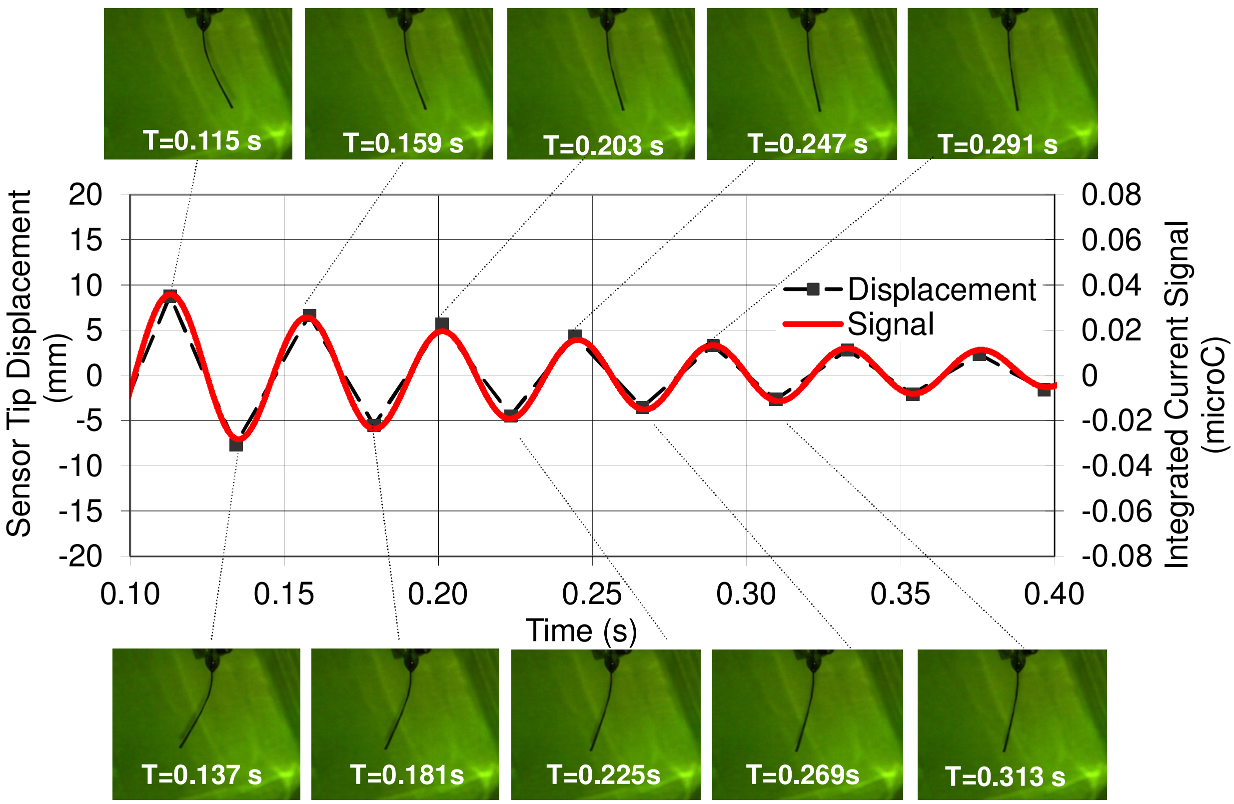

Figure 2-5 The tip displacement captured by the high-speed imaging system and the integrated short-current signal of the IPMC sensor vibrating in air

2.2.3 IPMC responses in different fluid media

Figure 2-6 shows the flow sensor assembly in which an IPMC beam was securely fixed to an adaptor for use in a rigid flow channel. The free length of the IPMC beam was 10 mm. The beam was 4 mm wide and 0.25 mm thick.

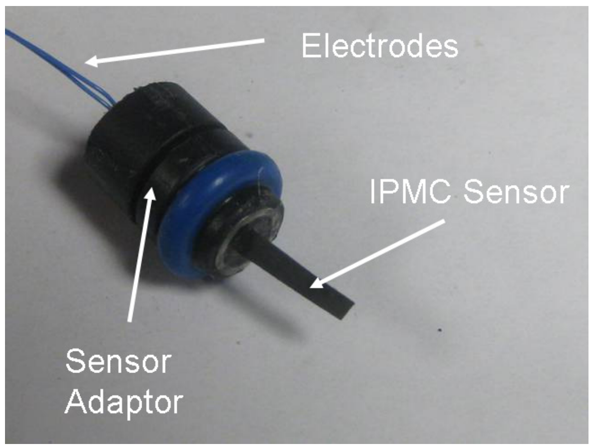

Figure 2-6 An IPMC beam in a sensor assembly

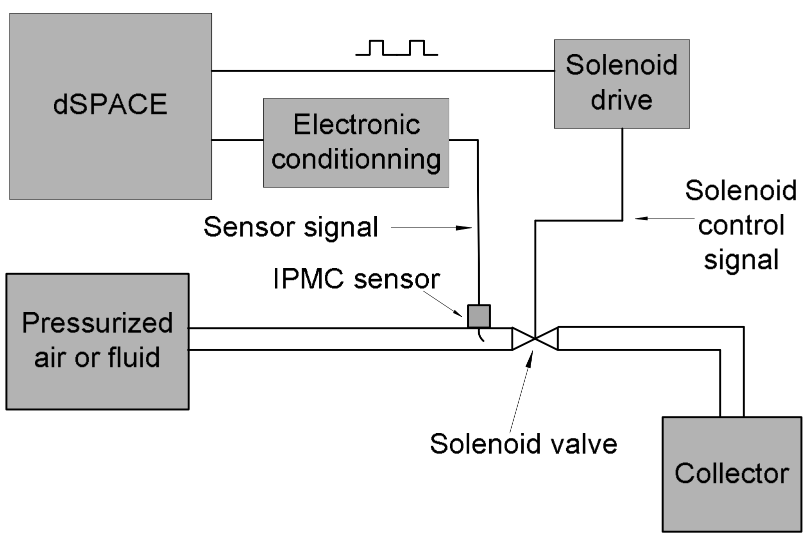

Figure 2-7 Schematic of the experimental setup for characterizing IPMC sensor responses in different fluid media

Figure 2-7 shows the schematic of the experimental setup for characterizing the sensor responses in different fluid media. The bending direction of the beam was aligned with the direction of the pressurized pulsating flow. The IPMC sensor was located at the inlet of the solenoid control valve. The on-off solenoid control signal shown in Figure 2-7 was used to generate the pulsating flow to excite the IPMC sensor.

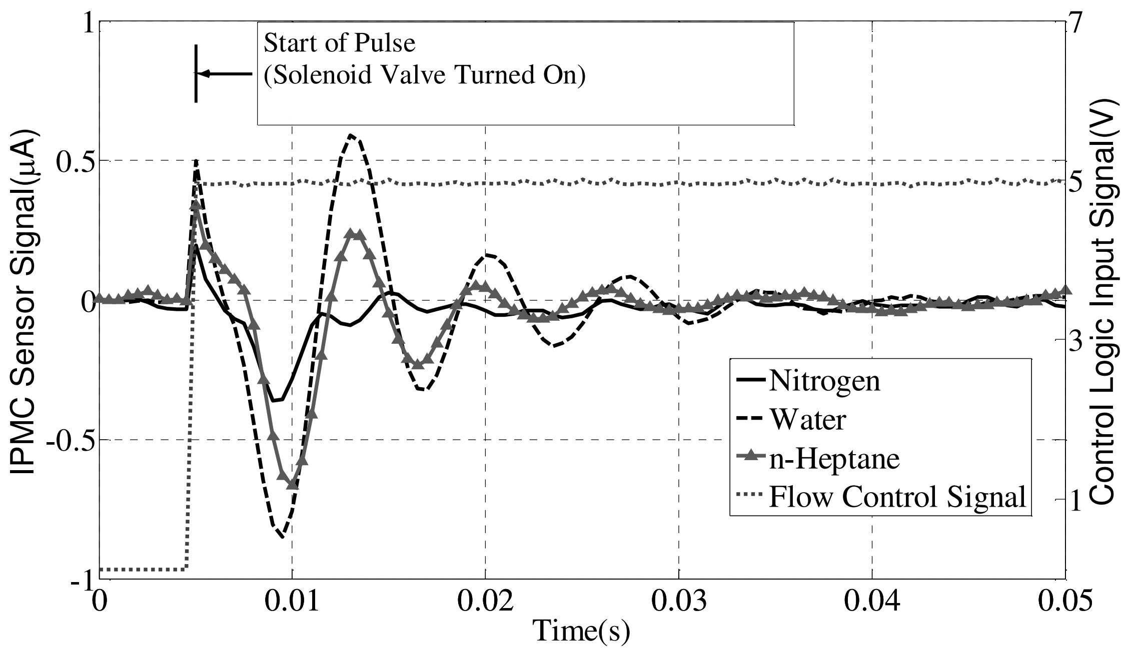

Figure 2-8 IPMC sensor responses after the start of the flow pulse

Three fluid media, nitrogen gas, distilled water, and n-Heptane, were used in the experiments due to their distinct fluid properties such as density and viscosity. Note that n-Heptane is a single-constituent hydrocarbon liquid typically substituted for gasoline in bench testing of gasoline fuel system components, and both its density and viscosity are in the mid-range between those of nitrogen gas and distilled water.

Figure 2-8 shows the responses of the IPMC sensor stimulated by three different fluid media after the solenoid valve was opened. The fluid pressure was regulated at 207 kPa and the solenoid pulse duration (pulsating flow duration) was set to 100 ms. The "Start of Pulse" in the figure indicated the instant when the solenoid was energized (i.e., valve opened). The key information provided by Figure 2-8 is that the IPMC beam signals were quite distinct under the three fluid media. In particular, the peak amplitude and the decay of the damped oscillations were highly correlated with the differences in the fluid media. The signal magnitude was the largest for water, which has the highest density and viscosity among the three fluids. The IPMC sensor responses following the end of pulsating flow (by deactivating the solenoid valve) also demonstrated different characteristics for the tested fluid media, as shown in Figure 2-9.

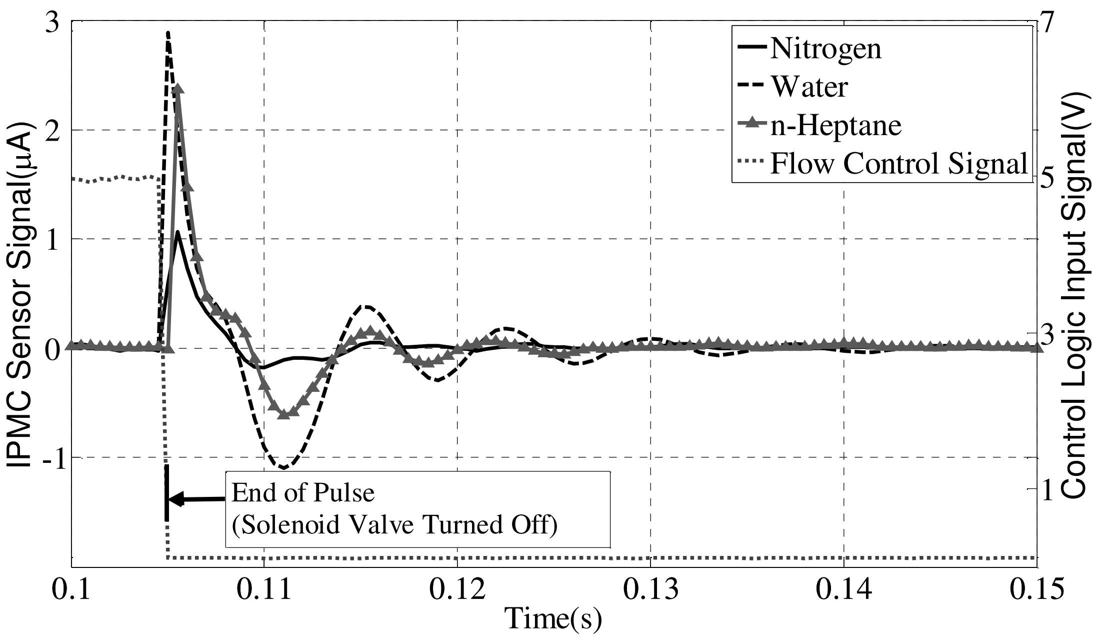

Figure 2-9 IPMC sensor responses following the end of the flow pulse

Besides the fluid properties, the fluid injection pressure (or flow rate) is a key parameter for internal combustion engines. Figure 2-10 shows the IPMC sensor response to an n-Heptane flow at three fluid pressures of 207, 310, and 514 kPa. These pressures correspond to typical conditions found in port fuel injection systems of gasoline engines. While the signals demonstrated similar damping behaviors for the three pressures, their amplitudes were different – the higher the pressure, the larger the signal amplitude. This is reasonable because the fluid flow rate directly impacts the driving force on the IPMC beam movement and thus the sensor output. Figure 2-8 to 2-10 indicate that both the amplitudes and the decay characteristics of the

IPMC sensor output carry useful information about the flow properties. Note that the sensor signal amplitudes and the decay characteristics shown in Figure 2-10 provide a strong indication that an IPMC sensor is not only capable of characterizing pulsating flows, but also possibly capturing various flow conditions.

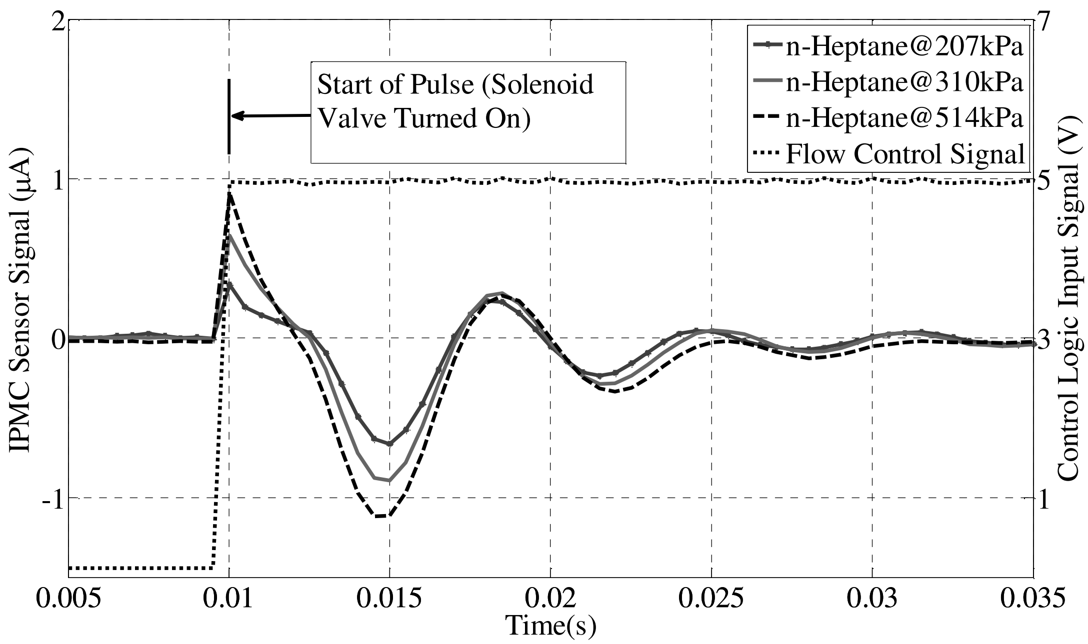

Figure 2-10 IMPC sensor responses to n-Heptane flow under three fluid pressures

2.2.4 IPMC beam responses to cyclic flows

In addition to reacting to pulsating flows with different fluid media and flow rates, another advantage of an IPMC flow sensor is its ability to capture the pulse-to-pulse variations between consecutive events initiated by the solenoid valve. Figure 2-11 shows the sensor response to two consecutive pulsating events of the water flow at 270 kPa. In this test, the solenoid valve was open for 100 ms and the pulse period was also set to 100 ms, providing a 50% duty-cycle pulsating flow. As the solenoid valve was energized by a TTL logic input signal, the sensor movement was induced by the pulsating fluid movement, resulting in distinct vibration signals immediately after the rising and falling edges of the logic pulse, respectively. It can be clearly seen that the sensor provides fairly repeatable signal corresponding to both pulse events. The information embedded in the signal slightly after the rising edge and the falling edges of the consecutive pulses could be useful for interpreting the pulse-to-pulse variations of the pulsating flow. This type of information is very critical to engine fuel flow control and calibrations which directly influence combustion stability. Currently high-fidelity measurement of the pulse-to-pulse flow variation is only available through a laboratory test bench. With the help of the IPMC flow sensor, the flow variation might be possible to measure it in the vehicle environment.

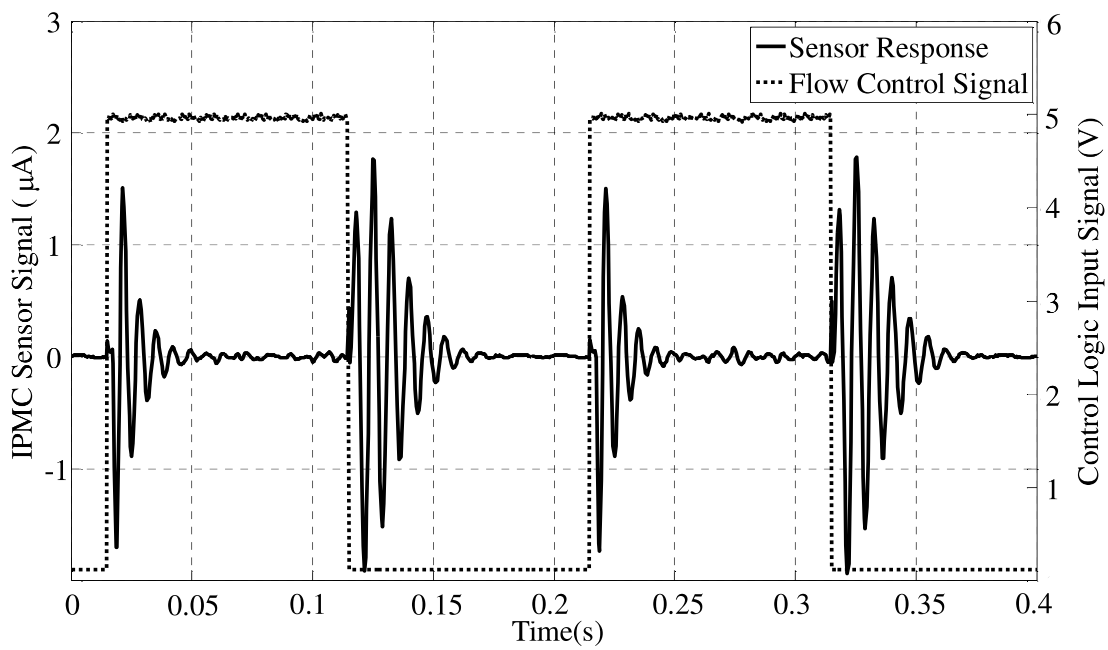

Figure 2-11 IPMC sensor response to two consecutive pulses of water flow

In summary, based upon the above experimental results, the IPMC holds a strong promise for measuring pulsating flow characteristics in internal combustion engines, including flow start and end instants, flow rate, pulse-to-pulse variations, and fluid media properties. In the following section we will discuss a multi-segment model for the IPMC beam dynamics in a fluid medium, which will be useful for estimating fluid characteristics based on the IPMC sensor output.

2.3 A Dynamic Model of an IPMC Beam in Fluid Flow

In order to effectively describe the dynamic responses of an IPMC beam interacting with a fluid flow, a multi-segment dynamic model is adopted in this research. Figure 2-12 illustrates the beam model with N rigid-body elements. The elements have equal length, and each is linked with its neighboring elements through joints modeled by a rotational spring (K_i) and a linear, rotational damper (H_i), where the index i denotes the i^{th} element. The damper collectively models the internal damping of the IPMC beam and the hydrodynamic damping due to the interaction with the surrounding fluid [46]. We have not considered the nonlinear damping effect in the interest of deriving an efficient estimation algorithm for real-time applications. We will further discuss this issue in Section VI. The drag force (F_{Di}) due to the surrounding medium can be modeled as a lumped load applied at the element center of mass.

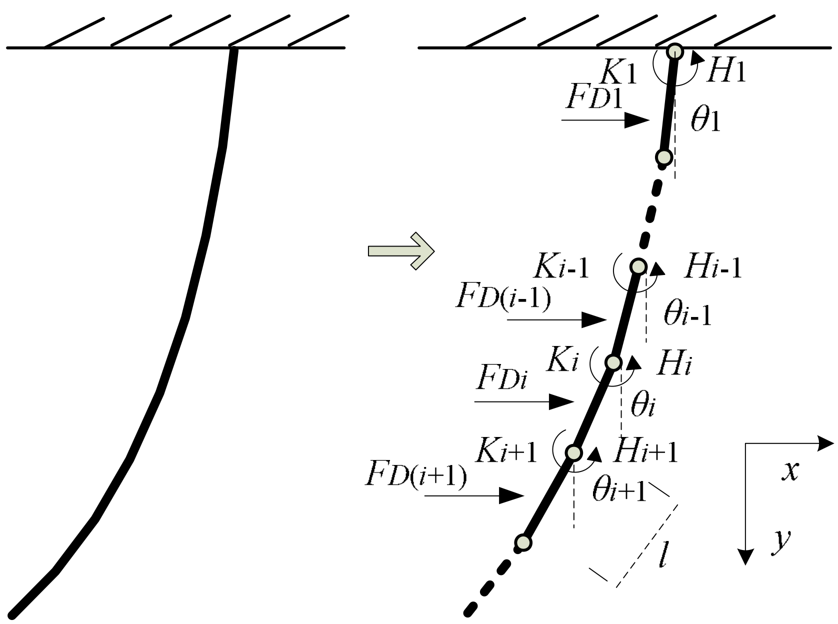

Figure 2-12 A cantilever beam modeled by a finite number of rigid elements

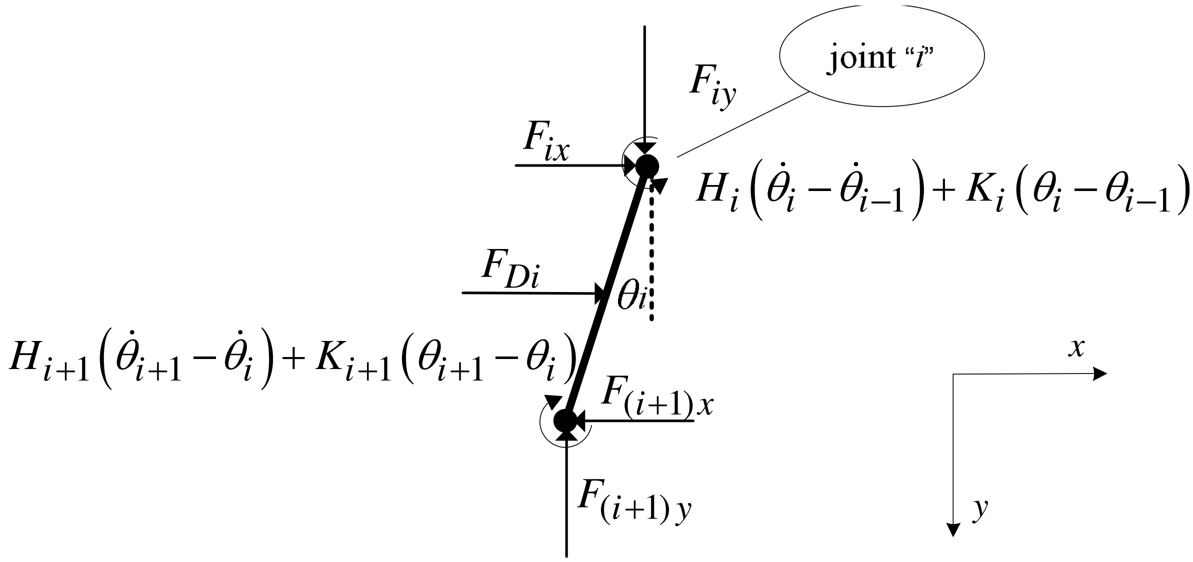

Figure 2-13 Free body diagram of the i^{th} beam element

Figure 2-13 shows the free body diagram for one element, where (x, y) are the coordinates in the inertial frame. For each element, the governing equation can be written in the following form based upon Newton's law

$$\begin{aligned} &J_i\ddot{\theta}_i+H_i\left(\dot{\theta}_i-\dot{\theta}_{i-1}\right)+K_i\left(\theta_i-\theta_{i-1}\right)-H_{i+1}\left(\dot{\theta}_{i+1}-\dot{\theta}_i\right)-K_{i+1}\left(\theta_{i+1}-\theta_i\right) \\ &\quad =F_{iy}\sin\theta_i\frac{l}{2}+F_{ix}\cos\theta_i\frac{l}{2}+F_{(i+1)y}\sin\theta_i\frac{l}{2}+F_{(i+1)x}\cos\theta_i\frac{l}{2},\ (i=1,\cdots,N), \end{aligned} \tag{2.1}$$

where J_i is the moment of inertia for the i^{th} element, l is the length of the beam element, F_{ix} and F_{iy} are the reaction forces at the i^{th} node in the x and y directions, respectively, and $F_{(i+1)x}$ and $F_{(i+1)y}$ are defined similarly for the $(i+1)^{th}$ node. Note that, from Newton's law, the translational motion satisfies the following equations:

$$m_i\cdot a_{ix}=F_{Di}+F_{ix}-F_{(i+1)x}, \tag{2.2}$$

$$m_i\cdot a_{iy}=F_{iy}-F_{(i+1)y}, \tag{2.3}$$

where m_i is the effective mass of beam element i, as defined later in (2.11), and a_{ix} and a_{iy} are the accelerations in x and y directions, respectively, at the center of the mass for element i. To facilitate the derivation of an efficient estimation algorithm for real-time applications, we assume small angular displacements in this study, so that

$$\sin\theta_i \approx \theta_i, \cos\theta_i \approx 1, \ i = 1, 2, \cdots, N. \tag{2.4}$$

Note that the approximation made in equation (2.4) leads to a maximum error of 1.5% when the beam angle is less than or equal to 10 degrees (0.17 rad). With this assumption, both a_{ix} and a_{iy} can be approximated by the following equations.

$$a_{ix} = \sum_{j=1}^{i-1} \ddot{\theta}_j l + \frac{1}{2}\ddot{\theta}_i l, \ i = 1, 2, \cdots, N, \tag{2.5}$$

$$a_{iy} = 0, \ \ i = 1, 2, \cdots, N. \tag{2.6}$$

Note that since $F_{(N+1)y}$ is zero, we have $F_{iy} = 0$, $i = 1, 2, \cdots, N$, from (2.3) and (2.6). On the other hand, from (2.2) and (2.5), F_{ix} in (2.1) can be solved as a linear combination of F_{Dj} and $\ddot{\theta}_j$, $j = 1, 2, \cdots, N$, with $F_{(N+1)x}$=0.

The drag force F_{Di} applied to each element is exerted by the surrounding medium, and it can be expressed as

$$F_{Di} = b \cdot l \cdot C_D \cdot \rho \cdot \frac{\hat{V}_i^2}{2}, \tag{2.7}$$

where b is the beam element width, C_D is the drag coefficient, ρ is the fluid density, and $\hat{V}_i$ is the relative beam velocity with respect to the fluid at the center of the element. Note that $\hat{V}_i = V_0 + V_{xi}$, where V_0 is the fluid velocity, and V_{xi} is the x-direction component of the beam element linear velocity (V_i) at its center of mass. Again, assuming that θ_i is relatively small, we can approximate V_{xi} by V_i.

The moment of inertia J_i, rotational stiffness K_i, and damping coefficient H_i can be expressed in terms of the beam dimensions, and the properties of the beam material and the fluid,

$$J_i = J_e = \frac{m_i \cdot l^2}{12}, \tag{2.8}$$

$$K_i = K_e = \frac{\gamma \cdot b \cdot c^3}{12l}, \tag{2.9}$$

$$H_i = H_e = \xi \cdot 2\sqrt{J_i \cdot K_i} = \xi \cdot 2\sqrt{J_e \cdot K_e}, \tag{2.10}$$

where m_i is the effective mass for element *i*, *c* is the beam element thickness, γ is the (effective) Young's modulus of IPMC material, and ξ is the critical damping ratio accounting for both material damping and hydrodynamic damping. The effective mass m_i represents the sum of the actual mass of element *i* and the added mass for this element due to beam-fluid interactions [46], [60], and it can be expressed as

$$m_i = \rho_e blc, \tag{2.11}$$

where ρ_e represents the effective density of the beam, which depends on the material density, fluid density, and beam geometry. Note that since all the beam elements are identical, they have the same moment of inertia J_e, stiffness K_e, and the damping coefficient H_e.

We can rewrite (2.1) in a compact matrix form:

$$J \cdot \ddot{\theta} + H \cdot \dot{\theta} + K \cdot \theta = \Gamma_b, \tag{2.12}$$

where *J, H*, and *K* are matrices of moments of inertia, damping coefficients, and spring constants, respectively. For the *N*-element beam model, these matrices are expressed as

$$J = \begin{bmatrix} 12(N-1)+4 & 12(N-2)+6 & \cdots & \cdots & 18 & 6 \\ 12(N-2)+6 & 12(N-2)+4 & \cdots & \cdots & 18 & 6 \\ \vdots & \vdots & \ddots & & \vdots & \vdots \\ \vdots & \vdots & & \ddots & 18 & 6 \\ 18 & 18 & \cdots & 18 & 16 & 6 \\ 6 & 6 & \cdots & 6 & 6 & 4 \end{bmatrix} J_e \tag{2.13}$$

$$H = \begin{bmatrix} 2H_e & -H_e & & & \\ -H_e & 2H_e & \ddots & & \\ & \ddots & \ddots & \ddots & \\ & & \ddots & 2H_e & -H_e \\ & & & -H_e & H_e \end{bmatrix} \tag{2.14}$$

$$K = \begin{bmatrix} 2K_e & -K_e & & & \\ -K_e & 2K_e & \ddots & & \\ & \ddots & \ddots & \ddots & \\ & & \ddots & 2K_e & -K_e \\ & & & -K_e & K_e \end{bmatrix}. \tag{2.15}$$

The angular displacement vector θ and the fluid flow-induced torque vector Γ_b are expressed as

$$\theta = \begin{bmatrix} \theta_1 \\ \vdots \\ \theta_i \\ \vdots \\ \theta_N \end{bmatrix}, \Gamma_b = \frac{l}{2} \begin{bmatrix} F_{D1} + 2\sum_{j=2}^{N} F_{Dj} \\ \vdots \\ F_{Di} + 2\sum_{j=i+1}^{N} F_{Dj} \\ \vdots \\ F_{DN} \end{bmatrix}. \tag{2.16}$$

2.4 Least-Squares Fluid Parameter Identification

Assume that all the IPMC beam model parameters defined in (2.13), (2.14), (2.15) are available. We further assume that the fluid flow velocity V_0 in (2.16) is known; in practice, this value could be determined in a number of ways, e.g., based on the applied fluid pressure. We can rewrite (2.12) into the following state-space form, where the product of remaining unknown parameters C_D and ρ appears linearly in the driving term,

$$\dot{x}_b = A_b x_b + B_b u_b, \quad u_b = \bar{V} C_D \rho, \qquad (2.17)$$
$$y_b = C_b x_b, \qquad y_b = \dot{\theta}_N,$$

where

$$x_b = \begin{bmatrix} \theta \\ \dot{\theta} \end{bmatrix}, A_b = \begin{bmatrix} 0_{N\times N} & I_{N\times N} \\ -J_{N\times N}^{-1} \times K & -J_{N\times N}^{-1} \times H_{N\times N} \end{bmatrix},$$
$$B_b = \begin{bmatrix} 0_{N\times N} \\ J_{N\times N}^{-1} \times Q_{N\times N} \end{bmatrix}, C_b = \begin{bmatrix} 0_{1\times(N-1)} & 1 \end{bmatrix},$$

where $I_{N\times N}$ is an identity matrix and

$$Q_{N\times N} = \frac{bl^2}{2} \begin{bmatrix} 1/2 & 1 & \cdots & 1 & 1 \\ 0 & 1/2 & \cdots & 1 & 1 \\ \vdots & \vdots & \ddots & \vdots & \vdots \\ 0 & 0 & \cdots & 1/2 & 1 \\ 0 & 0 & \cdots & 0 & 1/2 \end{bmatrix}, \bar{V} = \begin{bmatrix} (V_0 + V_1)^2 \\ \vdots \\ (V_0 + V_i)^2 \\ \vdots \\ (V_0 + V_N)^2 \end{bmatrix}.$$

Note that the velocity V_i at the center of element i and the beam tip velocity V_{tip} satisfy the following equations,

$$V_i = l\dot{\theta}_i / 2 + \sum_{j=1}^{i-1} l\dot{\theta}_j, \qquad (2.18)$$

$$V_{tip} = \sum_{j=1}^{N} l\dot{\theta}_j. \qquad (2.19)$$

As discussed in Section II, when the vibration frequency is relatively low, the short-circuit current signal i_{short} from the IPMC sensor can be related to the beam tip velocity V_{tip} through a static gain,

$$V_{tip} = \eta \cdot i_{short}, \qquad (2.20)$$

where the gain η can be determined with the formulae presented in [32] or obtained experimentally.

From (2.14) and (2.15), the damping matrix H is proportional to the stiffness matrix K, that is, $H = \beta K$, where β is a scalar. The mode frequencies in system (2.12) can be obtained by using Rayleigh damping theory [58]. System (2.12) can be transformed into its modal coordinates,

$$\ddot{q} + \bar{H}\dot{q} + \bar{K}q = P_b{}^T \Gamma_b, \tag{2.21}$$

where, $q = P_b{}^{-1}\theta$ is the angular displacement vector in the modal coordinates, and $\bar{H} = P_b{}^T H P_b$ and $\bar{K} = P_b{}^T K P_b$ are diagonalized damping and stiffness matrices, respectively. The column vectors, P_{bi} $(i = 1, 2, \cdots, N)$, of the coordinate transformation matrix, $P_b = [P_{b1}, \ \cdots, \ P_{bi}, \ \cdots, \ P_{bN}]$, is the orthonormal mode shape vectors satisfying the following conditions

$$(K - \omega_i^2 J)P_{bi} = 0 \text{ and } P_{bi}^T J P_{bi} = 1, \ i = 1, 2, \cdots, N, \tag{2.22}$$

where ω_i is the i^{th} mode frequency. Recall that we are concerned with pulsating flows in this research. Therefore, within each pulse, the IPMC beam is subject to a constant flow following the initial impact, which implies that the first mode response $P_{b1} = [p_{b11}, \ \cdots, \ p_{bi1}, \ \cdots, \ p_{bN1}]^T$ dominates the beam vibrations. If higher-frequency modes are excited by the initial impact, the responses associated with those modes will be damped out much faster than that of the first mode, in which case one can use the output data beyond the initial impact for parameter estimation. With these considerations, we derive the following relationships between the angular velocities,

$$\frac{\dot{\theta}_1}{p_{b11}} = \cdots = \frac{\dot{\theta}_i}{p_{bi1}} = \cdots = \frac{\dot{\theta}_N}{p_{bN1}}. \tag{2.23}$$

Consequently, from (2.18) and (2.19), the velocity V_i for element i can be expressed in terms of the beam tip velocity V_{tip},

$$V_i = \frac{\sum_{j=1}^{i-1} p_{bj1} + \frac{1}{2} p_{bi1}}{\sum_{j=1}^{N} p_{bj1}} V_{tip}. \tag{2.24}$$

For practical implementation purposes, we can convert the continuous-time model (2.17) to the discrete-time version,

$$\begin{aligned} x_b(k+1) &= \hat{A}_b x_b(k) + \hat{B}_b u_b(k), \\ y_b(k) &= \hat{C}_b x_b(k), \end{aligned} \tag{2.25}$$

for a given sampling period T_s, where $\hat{A}_b = e^{A_b T_s}$, $\hat{C}_b = C_b$, and $\hat{B}_b = \int_0^{T_s} e^{A_b \sigma} B_{bc} d\sigma$. The solution to (2.25) can be obtained as

$$\begin{aligned} &x_b(k) = \hat{A}_b{}^k x_b(0) + \textstyle\sum_{j=0}^{k-1} \hat{A}_b{}^{k-j-1} \hat{B}_b \bar{V}(j) C_D \rho, \\ &y_b(k) = \hat{C}_b x_b(k). \end{aligned} \tag{2.26}$$

Let the initial condition of the state be $x(0) = x_0$. The following equation can be obtained based upon (2.26),

$$\bar{y}_b = \begin{bmatrix} y_b(1) \\ y_b(2) \\ \vdots \\ y_b(n) \end{bmatrix} = \begin{bmatrix} \hat{C}_b \hat{A}_b^1 & \hat{C}_b \hat{A}_b{}^0 \hat{B}_b \bar{V}(0) \\ \hat{C}_b \hat{A}_b{}^2 & \hat{C}_b \sum_{j=0}^{1} \hat{A}_b{}^{1-j} \hat{B}_b \bar{V}(j) \\ \vdots & \vdots \\ \hat{C}_b \hat{A}_b{}^n & \hat{C}_b \sum_{j=0}^{n-1} \hat{A}_b{}^{n-j-1} \hat{B}_b \bar{V}(j) \end{bmatrix} \begin{bmatrix} x_0 \\ C_D \rho \end{bmatrix} = \Phi_b(n) \begin{bmatrix} x_0 \\ C_D \rho \end{bmatrix}, \tag{2.27}$$

where n is the number of signal data points selected for identification. Note that the system matrices $(\hat{A}_b,\ \hat{B}_b,\ \hat{C}_b)$ are known, and the velocity vector $\overline{V}$, as defined following (2.17), can be calculated using equations (2.20) and (2.24). Therefore, the matrix $\Phi_b(n)$ can be obtained based upon the IPMC sensor output. To estimate the fluid property parameter $C_D\rho$ (product of the drag coefficient and fluid density), we seek the solution that minimizes the squared error:

$$\left\| \overline{y}_b - \Phi_b(n) \begin{bmatrix} x_0 \\ C_D\rho \end{bmatrix} \right\|_2 . \tag{2.28}$$

The corresponding solution can be readily computed as

$$\begin{bmatrix} x_{b0} \\ C_D\rho \end{bmatrix} = [\Phi_b{}^T(n)\Phi_b(n)]^{-1}\Phi_b{}^T(n)\overline{y}_b . \tag{2.29}$$

2.5 Experimental Results on Fluid Property Estimation

In this section, we apply the proposed modeling and estimation approach to estimate the fluid property parameter, $C_D\rho$, for two fluid media (water and n-Heptane) based upon the IPMC sensor output signals shown in Figure 2-8 and Figure 2-9. The number of rigid elements in the model impacts both modeling accuracy and computational complexity; a higher number of elements leads to more accurate modeling but entails higher computational cost. The number of rigid elements required to achieve certain accuracy in approximating a flexible beam is highly dependent on the geometry and material properties of the beam [59].

Figure 2-14 shows the simulated responses of the beam tip velocity following an initial impact, when different values of N are adopted for the number of rigid elements. The beam dimensions used in the simulation were the same as those of the IPMC beam used in the experiments, and other simulation parameters were chosen based on general knowledge about beam and fluid properties. The Simulink Simscape toolbox was utilized for the simulation. It can be observed in Figure 2-14 that, as the element number increases, the beam tip velocity trace gradually converges, and that the five-element model achieves a sound tradeoff between modeling accuracy and computational efficiency. Therefore, a model with five rigid elements was adopted in this work.

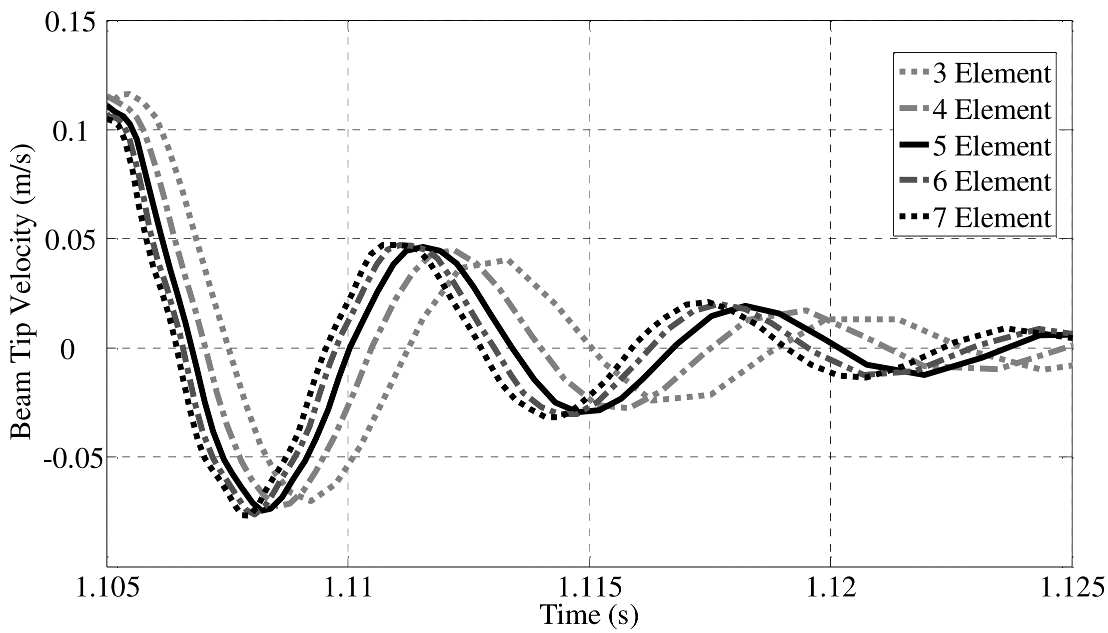

Figure 2-14 Convergence of the model as the number of beam elements increases

Before applying the estimation algorithm, we need to identify a few parameters for the beam model. The effective Young's modulus γ of IPMC was calculated based on the measured beam stiffness, following an experimental procedure described in [61]. The width b and the thickness c of the beam were measured directly, and the length l of each beam element was obtained by the measured beam length divided by 5. The gain η relating the beam tip velocity to the IPMC short-circuit current was estimated based on the results from high-speed imaging analysis (Figure 2-5). Finally, the damping ratio ξ and the effective beam density ρ_e were identified through curve-fitting, as shown in Figure 2-15. In particular, we tuned these two parameters until good agreement was achieved between the simulated beam tip velocity and the measured short-circuit current signal, following the rising edge of the control pulse in a pulsating water flow. These parameters were then used to estimate the fluid property parameter for other cases. Table 2-1 lists all the parameters identified for the beam model.

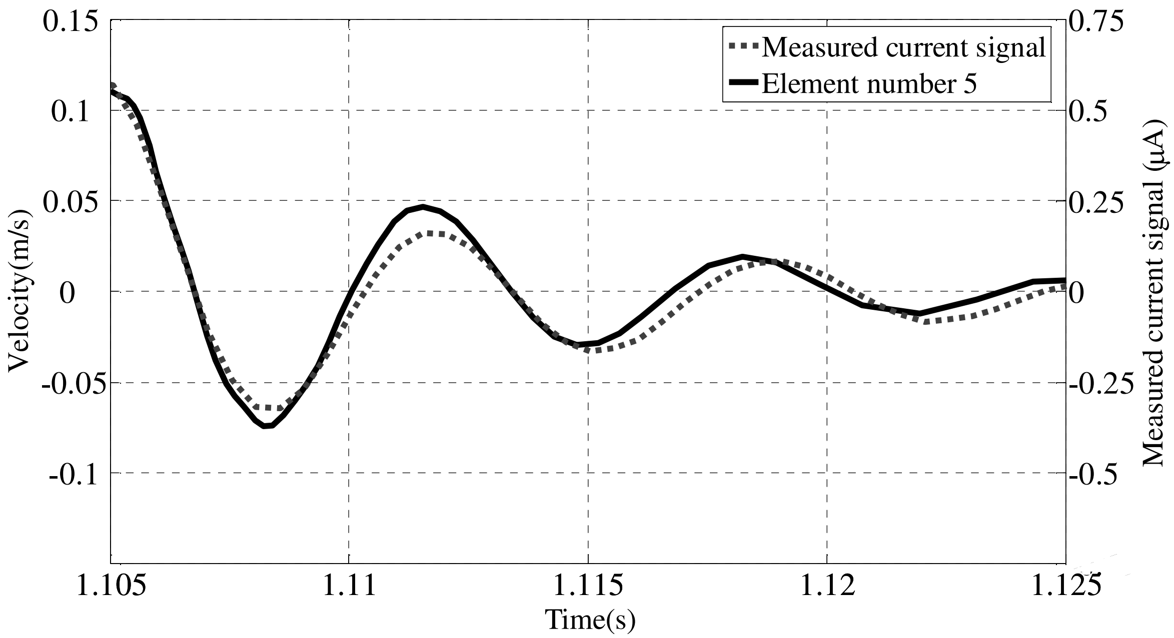

Figure 2-15 Identification of ξ and ρ_e through curve-fitting, where the measured IPMC current was taken from the case of a pulsating water flow, following the activation of the solenoid valve

Table 2-1. Parameters of the experimental IPMC beam.

γ (N/mm^2)	ξ	ρ_e (g/cm^3)	η (m/s/μA)	l (mm)	b (mm)	c (mm)
500	0.14	3	0.22	2	4	0.25

Table 2-2 lists the properties of the two fluids (water and n-Heptane), as well as their measured average velocities. Reynolds numbers (R_e) of the two fluids are obtained as [62]:

$$R_e = \frac{V_0 b}{v}. \tag{2.30}$$

where v is the kinematic viscosity of the fluid. Based upon the obtained Reynolds number, the actual drag coefficient C_D can be found using Figure 8.8 and Table 8.2 in [62]. Note that these drag coefficients were obtained with the assumption of a round, cylindrical beam. Since the IPMC beam is rectangular, we have provided a range of values for C_D in Table 2-2.

Table 2-2. Parameters of the tested fluids.

Liquid	ρ (g/cm^3)	v (mPa·s)	V_0 (m/s)	R_e	C_D
Water	1	1.007×10^{-6}	0.15	595.8	1.1 to 1.3
n-Heptane	0.684	0.564×10^{-6}	0.22	1583.4	0.8 to 1

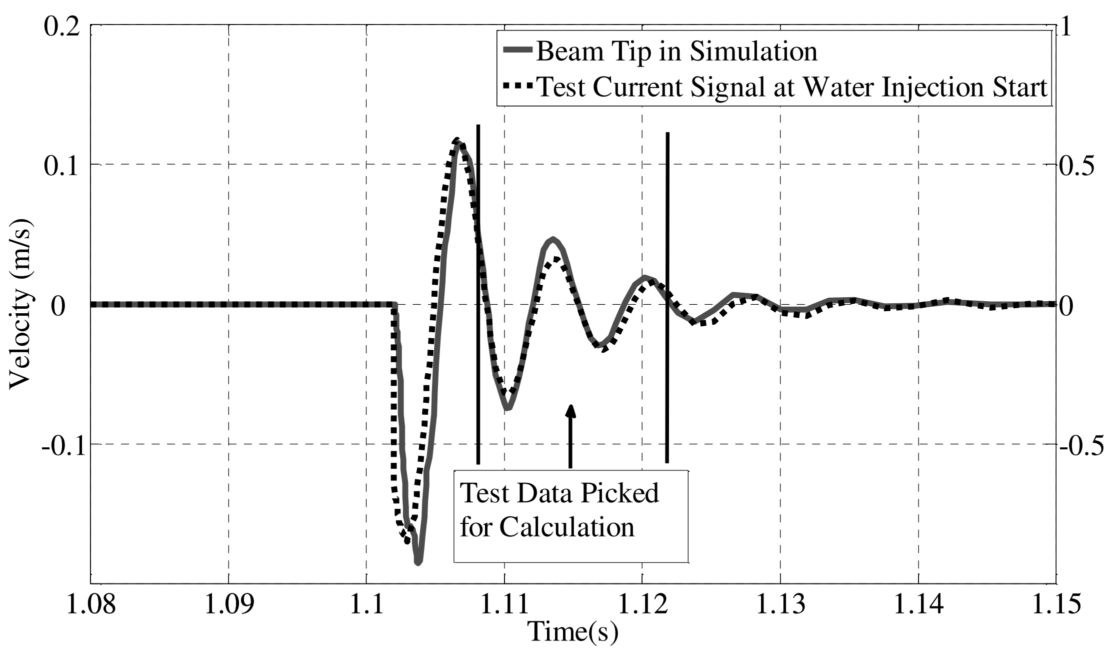

Figure 2-16 Selection of signal segment for parameter estimation, for the case where the beam motion was initiated by the start of a water flow pulse

Next, we will estimate the fluid property parameter $C_D\rho$ for water and n-Heptane using the measured IPMC sensor outputs shown in Figure 2-8 and Figure 2-9, and compare the estimates with the values derived from Table 2-2. The sampling time was 0.5 ms. Figure 2-16 shows the IPMC short-circuit current signal following the start of the water flow, and the simulated beam tip velocity based on the parameters ξ, ρ_e , and $C_D\rho$ that were obtained through curve-fitting. Recall that this was how the beam parameters ξ and ρ_e were identified. Due to the large angular displacement at the start of pulse flow, the current signal does not correlate well with the simulated beam tip velocity immediately following the impact, since small displacement was assumed in the modeling process. In order to better identify the fluid property, we focused on a data segment away from the initial impact. The two vertical lines in Figure 2-16 depict the time interval for which the sensor data was used for parameter estimation.

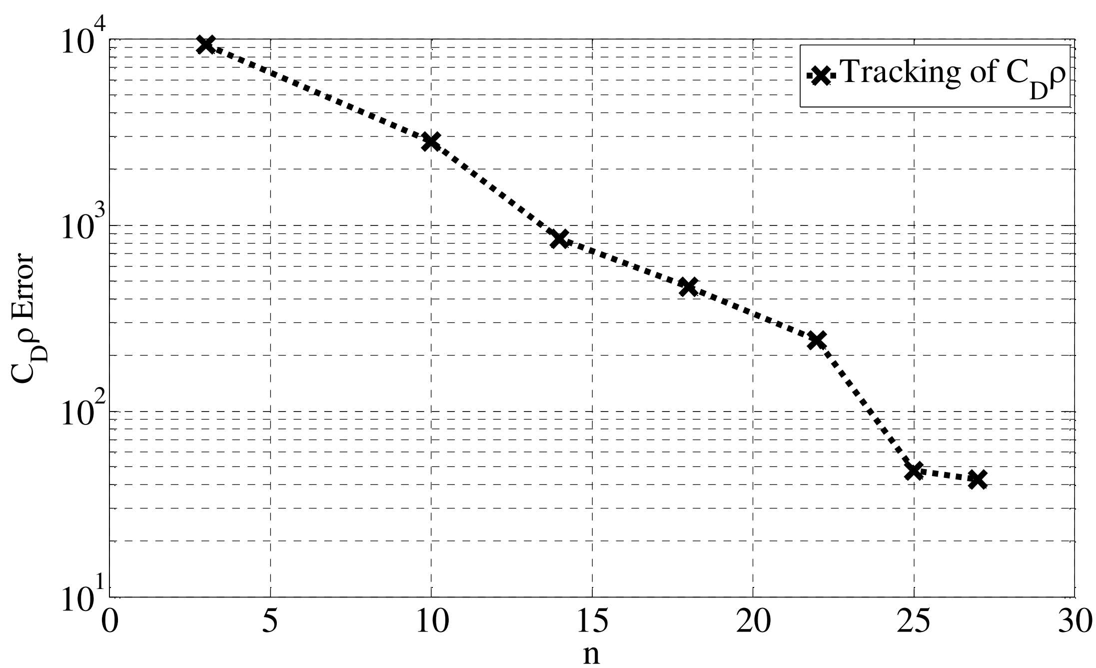

Figure 2-17 Estimation error as a function of data length, for the case where the beam motion was initiated by the start of a water flow pulse

Note that the number n of data points used in parameter identification affects the accuracy of the least-squares estimation. To demonstrate this effect, we took the test data shown in Figure 2-16 and performed estimation with data of different length. Figure 2-17 shows the estimation error as a function of the signal length n. The estimation error is with respect to the midpoint of the calculated range for $C_D\rho$ shown in Table 2-3. It can be seen that the estimation error drops as the signal length increases. But after the signal length is increased to a certain value, the estimation error converges. This is because it takes a certain number of data points to convey the oscillation characteristics. Therefore, the selection of the test data segment (including the data length) plays an important role in determining estimation accuracy and computational complexity. Figure 2-18 shows the selected data segments for parameter estimation for the three other cases. Note that in these cases, ξ and ρ_e identified earlier were used, and the values of $C_D\rho$ were obtained from the least-squares optimization.

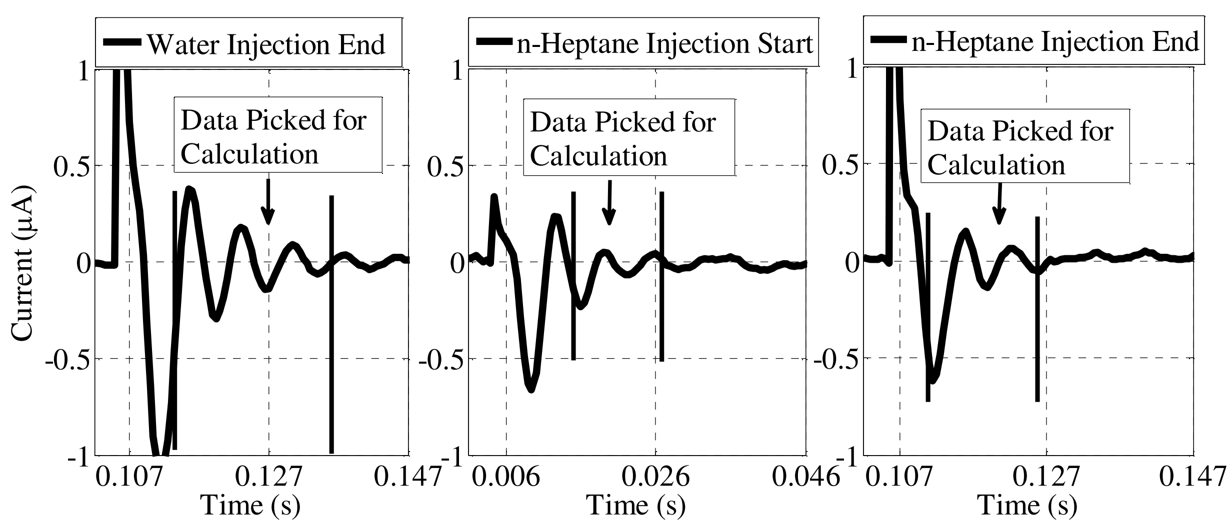

Figure 2-18 Selection of signal segments for parameter identification for the other three cases

The estimated fluid property parameters are summarized in Table 2-3 against the calculated ones. Here the calculated $C_D\rho$ range is obtained based on the data listed in Table 2-2.

It can be seen that the identified parameters are very close to their corresponding calculated values. Furthermore, the identified parameters using the data following the start of the pulses are consistent with those based upon the data following the end of the pulses. This is very important for automotive applications of on-board diagnostics and fuel composition detection.

Table 2-3. Estimated fluid property parameter $C_D\rho$ for water and n-Heptane.

Injection	Fluid	Calculated $C_D\rho$	Estimated $C_D\rho$
Start	Water	1100-1300	1157.4
End	Water	1100-1300	1137.0
Start	n-Heptane	547.2-684	579.3
End	n-Heptane	547.2-684	613.2

2.6 Conclusions and Discussions

Motivated by the potential application of the IPMC beam as flow sensors for automotive engines, this research investigates the feasibility of an efficient algorithm for identifying the fluid properties using the output of an IPMC sensor beam under pulsating flows. A dynamic, multi-segment model for IPMC beam dynamics was developed and solved analytically. The obtained solution, linear in the parameter of interest (product of drag coefficient and fluid density), was then used to identify the fluid parameter through least-squares minimization, where, again, an analytical solution was readily available. The estimation scheme was applied to pulsating flows of two different media, water and n-Heptane, and the estimated fluid parameters showed good agreement with the true parameters for those media.

Our work has shown the promise of using IPMC for measuring flow conditions and fluid properties in pulsating flows. While the study was motivated by emerging automotive applications (such as detecting the composition of fuel blends), it can be extended and applied to flow sensing in other areas including biomedical systems. One such example could be the measurement of flow characteristics in blood vessels (pulsating flow in nature). On the fabrication side, with the advances being made in lithography-based microfabrication [30], [63], and [64], IPMC sensors can be scaled down to the micrometer range to accommodate the aforementioned applications. On the algorithm side, the dynamic model and the associated estimation scheme proposed in this work naturally accommodate scaling.

We now discuss several characteristics of IPMC materials as relevant to their proposed use in this research. The first is the bandwidth of an IPMC sensor. Since the sensing property is enabled by the redistribution of ions under mechanical stimuli, one might be concerned about the IPMC sensing bandwidth (the actuation bandwidth of IPMC is typically below 10 Hz). In fact, the bandwidth of IPMC sensors is sufficiently high for most applications envisioned in this research. For example, as it can be seen in Figure 2-8 to Figure 2-11, the output of an IPMC sensor beam that is 10 mm long, 4 mm wide, and 0.25 mm thick can clearly capture the motion of the beam vibrating at about 150 Hz. For property measurement of a flow (especially, a pulsating flow), one can design the geometry of the IPMC beam, so that its resonant frequency is high enough to allow significant mechanical motion in the frequency range of interest. We note, however, as the sensor is scaled down (e.g., by making it shorter) to obtain high resonant frequencies, the signal conditioning and amplification circuit needs to be properly enhanced to accommodate the generally weaker output from a small sensor.

It should be noted that fabrication of IPMC materials is yet not fully mature. For example, sample properties may have batch-to-batch variations, and material behaviors can change over time. As a result, one will need to calibrate individual sensors and periodically recalibrate them to obtain accurate sensor parameters in practical applications. On the other hand, IPMC fabrication is a very active research area and it is anticipated that, with further development, IPMCs will have much reduced batch-to-batch variation and much improved long-term behavioral stability. Furthermore, the model-based estimation algorithm proposed in this research exploits salient features (e.g., the damping characteristics) of the beam dynamics, which greatly reduces the importance of the absolute signal amplitude and thus mitigates the impact of the non-ideal behavior of IPMCs. We also want to point out that the modeling approach and the estimation algorithm presented in this research are applicable to other beam-shaped flow sensors and thus not limited to IPMC sensors.

Our current study has not considered the effect of surrounding fluid media on IPMC physical and mechanosensory properties. This did not seem to have a big impact on the presented work since, in each experiment, the IPMC sensor had relatively short time in contacting with the fluid. In long-term applications, one will need to address the potential influence of the fluid media on the sensor behavior. One approach is to coat or package the IPMC sensor beam so that it is isolated from the fluid. An alternative is to characterize the mechanical and sensing properties of the IPMC beam in each fluid and incorporate those properties in model-based estimation. In this work, we have also ignored the phase lag between the IPMC current output and the tip velocity. Such dynamics [32] can be incorporated to improve the estimation accuracy, especially for applications involving high-frequency beam oscillations.

In the interest of obtaining analytical solutions and thus efficient estimation algorithms for real-time applications, we have adopted several approximations and simplifications in the modeling and estimation approach. When offline estimation is acceptable, or when adequate computing power is available, one can consider extending the approach in a few directions, to improve the accuracy in the beam dynamics modeling and in the fluid property estimation.

First, instead of using the multi-segment modeling approach presented in this research, one can consider using nonlinear finite element methods to solve the nonlinear beam dynamics, which can potentially lead to more accurate solutions. Second, we have assumed a constant added-mass in this research. In extension, one could incorporate the fluid density-dependence of the added mass in the inertia matrix. The resulting estimation problem will be much more sophisticated, but it offers the possibility to simultaneously estimate the fluid density and the drag property. Third, nonlinearities can be included to improve the model fidelity across wider ranges of operating conditions and fluid properties. Besides dropping the small angular displacement assumption, an interesting question to investigate is nonlinear hydrodynamic damping. For example, the Keulegan-Carpenter (KC) number [65] in our setting was estimated to be about 0.5 and the frequency parameter was about 2400. Nonlinear damping, where the damping coefficient depends on the oscillation amplitude and frequency, could exist for such a combination of KC number and frequency parameter [66]. In our work, nonlinear damping has not been considered, which is partly justified by the fact that in many applications of interest (e.g., estimating a pulsating flow in an engine fuel system), the resulting amplitudes and frequencies of beam oscillations have relatively small variations. For other applications where the vibration characteristics could vary significantly, it will be of interest to examine nonlinear damping.

Finally, we note that, while this work has focused on the sensing of pulsating flows, IPMC sensors can also be used to measure continuous flows. In the latter setting, the flutter instability of an IPMC beam when the flow speed exceeds critical values can be potentially exploited to extract the flow information. For example, the measurement of the flutter frequency (easily available from IPMC output) can be used to infer either the flow speed (if fluid properties, such as viscosity, are known) or the fluid properties (if the flow speed is known).

CHAPTER 3 AFR TRACKING WITH BIOFUEL CONTENT ESTIMATION

3.1 Introduction

The interest of biofuels is due to its renewable characteristics and low emissions [3], [67] such as particulate matter (PM). For diesel engines, biodiesel is commonly blended with petroleum based diesel. Because its physical properties and chemical compositions are quite different from the petroleum based diesel [68]-[70], the blend of biodiesel and petroleum based diesel has quite different combustion characteristics. Similarly, for gasoline engines, the ethanol is blended with petroleum based gasoline, leading to quite different combustion characteristics. In order to optimize the combustion process for a given biofuel blend, it is necessary to identify the biofuel content so that the combustion process can be optimized through fuel injection timing and mass for diesel engines and through fuel mass and spark timing for gasoline engines. It is also worth mentioning that biofuel contains less energy content by volume than that of conventional petroleum based fuel. Therefore, the injected fuel quantity needs to be increased to meet the same engine load requirement compared to the petroleum based fuel.

There are several approaches that can be used to estimate the fuel content. References [4]-[6] estimate the fuel content based upon the oxygen sensor signals, [7] proposes using the in-cylinder pressure signal, [8] uses the ionization signal to estimate the fuel content, and the ionic polymer-metal composite beam sensor was used to estimate the fuel content through identifying the fuel viscosity in [71]. In this research, the oxygen sensor signal was used to adaptively estimate the biofuel content for a flex fuel lean burn engine. A similar technique has been used for gasoline engines [6], where the AFR (air-to-fuel ratio) of gasoline engines is maintained at the stoichiometric level through the closed loop control. However, neither the diesel engines nor the lean burn SI engines regulate AFR. This introduces an additional degree of difficulty to estimate the fuel content since it has to be completed with the AFR fluctuation. It will be even more challenging with an aging oxygen sensor with slow transient response. However, during the regeneration of the LNT (lean NOX Trap) aftertreatment system, the engine AFR is controlled in a closed loop for flex fuel lean burn engines, which provides an opportunity to accurately estimate the fuel content.

The LNT technology is designed to significantly reduce the engine NOx (nitric oxide and nitrogen dioxide) emissions for lean burn engines, such as diesel engines [11], [12] and [72]. In order to reduce the NOx emissions, an LNT catalyst is utilized to store the NOx emissions during lean operation, and when the stored NOx reaches a certain level, the LNT needs to be regenerated through rich AFR operation. During the short rich operation period, the LNT catalyst releases its stored NOx and regenerates its storage capacity, where the released NOx is converted into non-polluting nitrogen due to the rich AFR.

The rich AFR can be achieved either by using post injection [73] or by extending the main injection [74] to increase fuel injection mass. The quantity of injection needs to be controlled in a closed loop to regulate the AFR to the desired level based upon the oxygen sensor signal. The control strategies for the closed loop AFR control have been widely studied; see [6] for PI control, [22] for sliding mode control, [75] for adaptive control, and [76] for LPV control. In this research, an adaptive LQ tracking controller was proposed for biofuel lean burn engines to regulate the AFR during the LNT regeneration process, the biofuel content is estimated using a gradient based adaptive law [77]. The advantage of the LQ tracking control is that it constitutes a linear feedback control that can be easily computed and implemented with estimated state information subjected to system uncertainties and measurement white Gaussian noise [78]. In order to eliminate the steady state error, an integral action was introduced in the LQ controller.

The lean burn engine system was approximated in this research by a third order linear system with a transport delay between the engine combustion chamber and the exhaust manifold, exhaust manifold filling dynamics and the oxygen sensor dynamics. Since the mass air flow measurement and adaptive fuel content estimation introduces uncertainties into the system, the robust stability of the closed loop system was also studied in this research. The robust stability analysis of uncertain linear systems has received a lot of attention, particularly in the context of uncertain linear systems with time-varying parameters [79]-[83]. Most of the existing approaches use quadratic stability analysis, which is known as a sufficient condition for the stability of linear systems with arbitrarily fast time-varying parameters, because it does not take into account bounds on the time-derivatives of the varying parameters [79]-[80]. This research investigates the robust stability of the closed loop systems with linear parameter variations (LPV) inside a polytope with the bounded variation rate [82]-[83].

Several adaptive control schemes were studied through simulations with respect to the tracking control and adaptive estimation performance. The developed tracking control with adaptive biofuel content estimation was validated through dynamometer experiments of a lean burn SI engine. The best performance was reached with the adaptive gain-scheduling scheme. The gain-scheduled adaptive estimation is not only able to track the desired AFR during the fast fuel content transition but also is able to reduce the estimated fuel content fluctuation induced by oxygen sensor noise.

The main contribution of this research is the application of the adaptive LQ tracking control to regulate the AFR during LNT regeneration with guaranteed robust stability with respect to the varying fuel content estimation error and engine speed. The proposed control strategy was demonstrated on the engine dynamometer for a flex fuel lean burn engine equipped with LNT regeneration aftertreatment system.

The rest of this research is organized as follows. In Section 3.2 the system model is discussed and Section 3.3 presents the proposed adaptive estimation and tracking control algorithms. The robust stability analysis of the closed loop system is discussed in Section 3.4. Section 3.5 provides the simulation study results, the experiment validation is described in section 3.6, and Section 3.7 addresses the conclusions and future work.

3.2 Engine System Model

The lean burn engine system is modeled as a direct fuel injection engine with the exhaust manifold filling dynamics and oxygen sensor dynamics, see Figure 3-1, where the physical engine dynamics is shown in the solid box called plant. To simplify the control design process, the engine model describes the dynamics from u to x_3. In the actual application the control input will be converted into the fuel mass $\dot{m}_{fuel}$ based upon the measured air charge mass $\dot{\hat{m}}_{air}$ and adaptively estimated fuel content $\hat{\alpha}$.

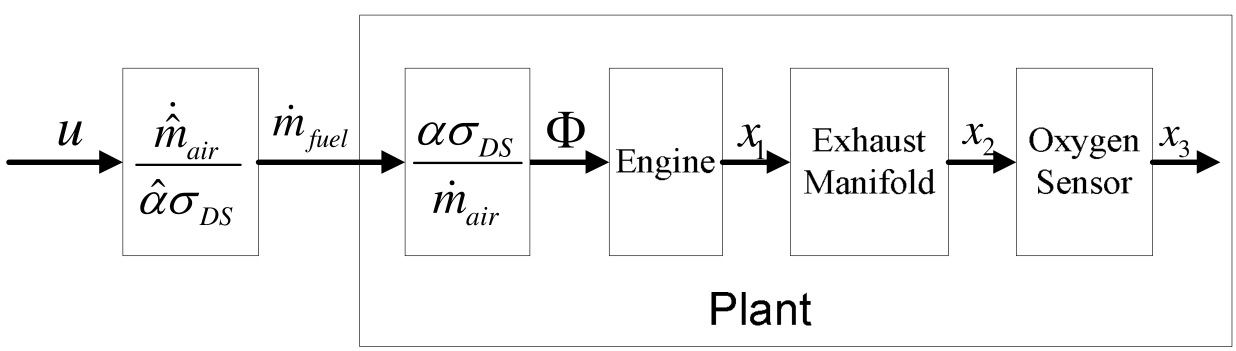

Figure 3-1 Engine system modeling

The input Φ in the solid box is the equivalence fuel-to-air ratio defined by

$$\Phi = \frac{\dot{m}_{fuel}}{\dot{m}_{air}} \sigma_{DS} \cdot \alpha, \tag{3.1}$$

where $\dot{m}_{air}$ is the air mass charged into the cylinder; σ_{DS} is the stoichiometric air-to-fuel ratio for the petroleum based fuel; and α is the stoichiometric gain between petroleum fuel and biofuel blend defined by

$$\alpha = \frac{\sigma_{BD}}{\sigma_{DS}}, \tag{3.2}$$

where σ_{BD} is the stoichiometric air-to-fuel ratio for the given biofuel blend. The injected fuel $\dot{m}_{fuel}$ is calculated based upon the measured charged mass $\dot{\hat{m}}_{air}$ and the estimated fuel gain $\hat{\alpha}$ as shown below,

$$\dot{m}_{fuel} = \frac{\dot{\hat{m}}_{air}}{\hat{\alpha}\sigma_{DS}} u, \tag{3.3}$$

where, u is the equivalence fuel-to-air ratio calculated by the controller, and will be defined in the following section.

The transport delay between the cylinder and exhaust manifold can be modeled using the following first order transfer function

$$G_1(s) = \frac{1}{1+\tau_1 s}, \tag{3.4}$$

where τ_1 is the time constant for the transport delay, which accounts for the time from the instant of the fuel injection to the opening of the exhaust valve. The exhaust manifold filling dynamics is also modeled as the first order dynamics as follows

$$G_2(s) = \frac{1}{1+\tau_2 s}, \tag{3.5}$$

where τ_2 is the time constant of the charge filling dynamics and is a function of the effective length of the exhaust manifold and the exhaust flow rate. In this research, τ_2 is measured from the time that the exhaust valve opens to the oxygen sensor signal changes. The oxygen sensor dynamics is also modeled as the first order dynamics as below

$$G_3(s) = \frac{1}{1+\tau_3 s}, \tag{3.6}$$

where τ_3 is the time constant of the sensor dynamics. Note that τ_3 increases as the sensor gets old.

Therefore, the system transfer function from input equivalence ratio $U(s)$ to the output equivalence ratio $Y(s)$ measured by the oxygen sensor is

$$Y(s) = X_3(s) = \frac{1}{(1+\tau_1 s)(1+\tau_2 s)(1+\tau_3 s)} \frac{\alpha\sigma_{DS}}{\dot{m}_{air}} M_{fuel}(s), \tag{3.7}$$

where $M_{fuel}(s)$ is the Laplace transformation of $\dot{m}_{fuel}$. Equation (3.7) can also be expressed as

$$\begin{aligned} Y(s) &= \frac{1}{(1+\tau_1 s)(1+\tau_2 s)(1+\tau_3 s)} \frac{\dot{\hat{m}}_{air}\alpha}{\dot{m}_{air}\hat{\alpha}} U(s) \\ &= \frac{1}{(1+\tau_1 s)(1+\tau_2 s)(1+\tau_3 s)} (1+\delta)U(s), \end{aligned} \tag{3.8}$$

where $U(s)$ is the Laplace transformation of u, and $\delta = \frac{\dot{\hat{m}}_{air}\alpha}{\hat{\alpha}\dot{m}_{air}} - 1$ represents the system uncertainty due to the estimation error of the fuel content $\hat{\alpha}$ and measurement error of the air charge mass $\dot{\hat{m}}_{air}$. In addition, the fuel injection shot-to-shot variations are modeled as the system noise input w, and the oxygen sensor measurement noise is represented by v. This leads to the following nominal state space model with $\delta = 0$,

$$\begin{aligned} \dot{x} &= A_c x + B_c u + B_c w \\ y &= C_c x + v \end{aligned}, \tag{3.9}$$

where

$$A_c = \begin{bmatrix} -\frac{1}{\tau_1} & 0 & 0 \\ \frac{1}{\tau_2} & -\frac{1}{\tau_2} & 0 \\ 0 & \frac{1}{\tau_3} & -\frac{1}{\tau_3} \end{bmatrix}, \quad B_c = \begin{bmatrix} \frac{1}{\tau_1} \\ 0 \\ 0 \end{bmatrix}, \; C_c = \begin{bmatrix} 0 & 0 & 1 \end{bmatrix}.$$

Linear system (3.9) is then discretized into the following discrete state space model with a sample period of 0.025 s.

$$\begin{aligned} x(k+1) &= Ax(k) + Bu(k) + Bw(k) \\ y(k) &= Cx(k) + v(k) \end{aligned}. \tag{3.10}$$

Note that, both the input noise $\{w(k), k = 0,1,...\}$ and measurement noise $\{v(k), k = 0,1,...\}$ are assumed to be zero mean and mutually independent random vectors such that

$$\begin{aligned} &E\{w(k)\} = 0,\ W = E\{w(k)w(k)\} > 0 \\ &E\{v(k)\} = 0,\ V = E\{v(k)v(k)\} > 0 \end{aligned} \tag{3.11}$$

where W and V are the corresponding covariance matrices.

3.3 Control Strategy Development

The proposed control algorithm used to regulate the combustion air-to-fuel ratio with the presence of unknown biofuel content is an adaptive LQG tracking controller as shown in Figure 3-2, where the adaptive scheme is used to estimate the fuel gain α (or content); the Kalman state estimator is used to estimate system state vector x, and the optimal LQ tracking controller is used to track the desired equivalence ratio r based upon the estimated states.

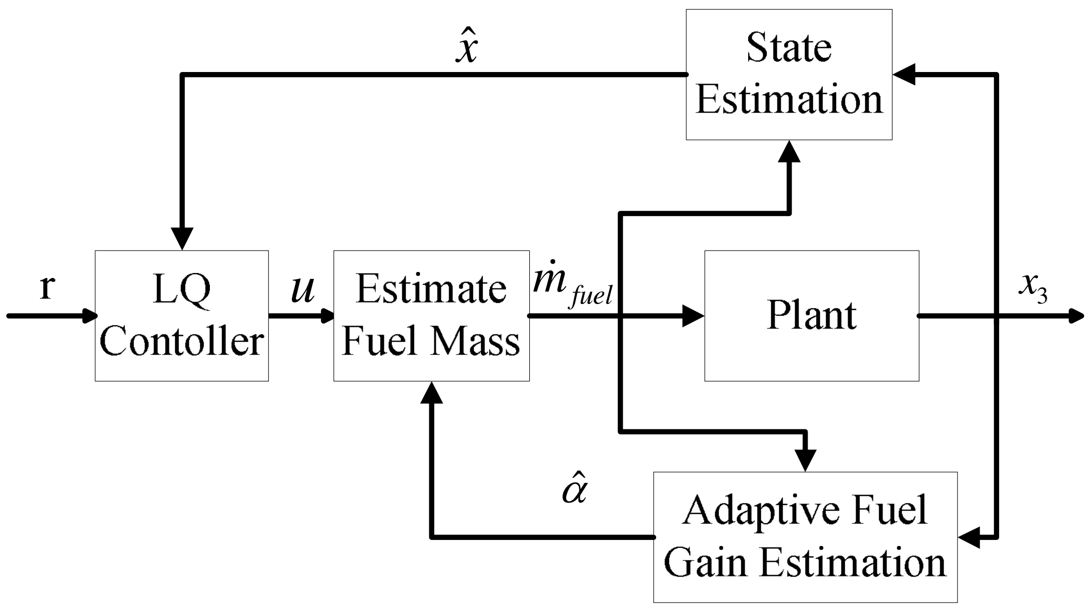

Figure 3-2 Adaptive LQG tracking control system

3.3.1 Adaptive fuel gain estimation

In equation (3.7), assuming that the injected fuel mass for conventional fuel is known, the air mass can be measured by a mass flow sensor, and state x_3 is the fuel-to-air ratio measured by the oxygen sensor at the exhaust manifold. The only unknown term is the fuel gain α . We can reorganize equation (3.7) into the below form,

$$X_3(s) = \alpha G(s)\frac{1}{\dot{m}_{air}}M_{fuel}(s) = \alpha\phi(s), \tag{3.12}$$

where

$$G(s) = \frac{\sigma_{DS}}{(1+\tau_1 s)(1+\tau_2 s)(1+\tau_3 s)}, \phi(s) = G(s)\frac{1}{\dot{m}_{air}}M_{fuel}(s).$$

Discretizing transfer function $G(s)$ defined in equation (3.12) yields the following discrete transfer function

$$X_3(z) = \alpha G(z)\frac{1}{\dot{m}_{air}} M_{fuel}(z) = \alpha Z(z) \tag{3.13}$$

Based upon the gradient method introduced in [77] that minimizes the instantaneous cost

$$J(\hat{\alpha}) = \frac{(x_3(k) - \hat{\alpha}(k-1)z(k))^2}{2m_s^2(k)}, \tag{3.14}$$

where $z(k)$ is the inverse "z" transformation of $Z(z)$, the adaptive law is obtained as

$$\hat{\alpha}(k) = \begin{cases} \hat{\alpha}(k-1) + \Gamma\varepsilon(k)z(k), & \text{for } \forall\hat{\alpha} \in [\underline{\alpha}, \overline{\alpha}] \\ \hat{\alpha}(k-1), & \text{otherwise} \end{cases}, \tag{3.15}$$

where constant $\underline{\alpha}$ and $\overline{\alpha}$ represent the lower and upper bounds of the estimated $\hat{\alpha}(k)$, respectively; Γ is the adaptive gain; and $\varepsilon(k)$ is defined by

$$\varepsilon(k) = \frac{x_3(k) - \hat{\alpha}(k-1)z(k)}{m_s^2(k)}. \tag{3.16}$$

where $m_s^2(k) = 1 + 0.01z^T(k)z(k)$ is chosen to guarantee the bounded estimation of $\hat{\alpha}(k)$.

It is well known that the convergence of the estimate $\hat{\alpha}$ is guaranteed by the persistent exciting $\phi(t)$ assumption [77], where $\phi(t)$ is the inverse Laplace transform of $\phi(s)$ in (3.12). Since $\phi(t)$ is a scalar function, as long as the fuel flow is great than zero, or $\dot{m}_{fuel} > 0$, there exist $\xi > 0$ and $T_0 > 0$ such that

$$\int_t^{t+T_0} \phi(\tau)\phi^T(\tau)d\tau \geq T_0\xi \tag{3.17}$$

for $t \geq 0$. Since the above integral is always invertible, the condition for the persistent excitation is always satisfied, and hence, the estimation convergence is guaranteed.

3.3.2 Kalman state estimation

The Kalman state estimation is a stochastic filter that provides the optimal state estimation for a linear system subject to Gaussian noise inputs. For a given initial state $\hat{x}(0)$ and the current measurement $y(k)$, the Kalman estimate states can be expressed in the following form

$$\hat{x}(k+1) = A\hat{x}(k) + Bu(k) + K_f[y(k+1) - C\hat{x}(k)]. \tag{3.18}$$

The Kalman estimation gain K_f can be calculated from the following equation

$$K_f = HC^T[CHC^T + V]^{-1}, \tag{3.19}$$

where the state error covariance matrix H is solved by the following algebraic Riccati equation

$$H = A[H - HC^T(CHC^T + V)^{-1}CH]A^T + BWB^T. \tag{3.20}$$

3.3.3 LQ tracking control with integral

In this section, an LQ controller was developed to track the desired equivalence fuel-to-air ratio. In order to eliminate the steady state error, an integral control was introduced into the LQ controller by defining the tracking error $e(k)$ as

$$e(k+1) = e(k) + y(k) - r(k) = e(k) + Cx(k) - r(k). \tag{3.21}$$

Augmenting state vector $\tilde{x}(k) = \begin{bmatrix} x(k) \\ e(k) \end{bmatrix}$ yields the following state equation

$$\begin{aligned} \tilde{x}(k+1) &= \tilde{A}\tilde{x}(k) + \tilde{B}u(k) + dr(k) \\ y(k) &= \tilde{C}\tilde{x}(k) \end{aligned}, \tag{3.22}$$

where

$$\tilde{A} = \begin{bmatrix} A & 0_{3\times 1} \\ C & 1 \end{bmatrix}, \quad \tilde{B} = \begin{bmatrix} B \\ 0 \end{bmatrix}, \quad \tilde{C} = [C \quad 0], \quad d = \begin{bmatrix} 0_{3\times 1} \\ -1 \end{bmatrix}.$$

The cost function of the LQ controller is defined as

$$J = \underset{N\to\infty}{E}\left\{\sum_{k=0}^{N-1}[\tilde{x}(k)^T Q\tilde{x}(k) + u(k)^T Ru(k)]\right\}, \tag{3.23}$$

where the weight matrices Q and R are given so that $Q = Q^T \geq 0$, and $R = R^T > 0$. Then, the optimal control is

$$u(k) = -\tilde{K}\tilde{x}(k) + K_r r(k), \tag{3.24}$$

where

$$\tilde{K} = [\tilde{B}^T S\tilde{B} + R]^{-1}\tilde{B}^T S\tilde{A}, \tag{3.25}$$

and S is the solution to the following algebraic Riccati equation

$$S = \tilde{A}^T[S - S(\tilde{B}(\tilde{B}^T S\tilde{B} + R)^{-1}\tilde{B}^T S]\tilde{A} + Q, \tag{3.26}$$

K_r in equation (3.24) is calculated by

$$K_r = \left[\tilde{B}^T S\tilde{B} + R\right]^{-1}\tilde{B}^T F_1, \tag{3.27}$$

and

$$F_1 = -\left[I - \tilde{A}^T + \tilde{A}^T SF_3F_2\right]^{-1}\tilde{A}^T SF_3F_2 d, \tag{3.28}$$

where $F_2 = \tilde{B}^T R^{-1}\tilde{B}$, $F_3 = \left[I + F_2 S\right]^{-1}$, and I is an identity matrix.

Define the dimension of x, y and u as n_x, n_y and n_u, respectively. Partition the state feedback matrix in terms of its first n_x columns and its last n_y columns,

$$\tilde{K} = \left[K_x \quad K_e\right]. \tag{3.29}$$

Then, the optimal control law can be written as follows

$$u(k) = -\left[K_x \quad K_e\right]\begin{bmatrix} x(k) \\ e(k) \end{bmatrix} + K_r r(k). \tag{3.30}$$

Since not all states are measurable, recall the Kalman state estimate $\hat{x}(k)$ and replace $x(k)$ with $\hat{x}(k)$ in equation (3.30). Then, the LQG control law can be expressed as below

$$u(k) = -K_x\hat{x}(k) - K_e e(k) + K_r r(k). \tag{3.31}$$

3.4 System Robust Stability Analysis

The robust stability of the closed loop system, shown in Figure 3-2, in the presence of system uncertainty δ is analyzed using the approach introduced in [83] for linear parameter variation systems. For the stability analysis, the system noise input w and the oxygen sensor measurement noise v in equation (3.10) are set to zero. Replacing the control input with u defined in equation (3.31), equation (3.10) can be expressed as

$$x(k+1) = Ax(k) + B\left[-K_x\hat{x}(k) - K_e e(k) + K_r r\right](1+\delta(k)), \tag{3.32}$$

where the estimated state $\hat{x}$ and the tracking error e can be expressed as

$$\begin{aligned}\hat{x}(k+1) &= A\hat{x}(k) + K_f[Cx(k+1) - C\hat{x}(k)] \\ &+B\left[-K_x\hat{x}(k) - K_e e(k) + K_r r\right](1+\delta(k)),\end{aligned} \tag{3.33}$$

Then, equations (3.32), (3.33), and (3.21) can be written into the state space form

$$x_{CL}(k+1) = A_{CL}x_{CL}(k) + B_{CL}r, \tag{3.34}$$

where

$$x_{CL}(k) = \begin{bmatrix} x(k) \\ \hat{x}(k) \\ e(k) \end{bmatrix}_{n\times 1}, \quad B_{CL}(k) = \begin{bmatrix} (1+\delta(k))BK_r \\ (1+\delta(k))(B+K_f CB)K_r \\ -1 \end{bmatrix}_{n\times 1},$$

$$A_{CL} = \begin{bmatrix} A & -(1+\delta(k))BK_x & -(1+\delta(k))BK_e \\ K_f CA & \begin{matrix} A-K_f C \\ -(1+\delta(k))(B+K_f CB)K_x \end{matrix} & -(1+\delta(k))(B+K_f CB)K_e \\ C & 0 & 1 \end{bmatrix}_{n\times 1}$$

, and the order of the closed loop system is $n=7$. Define

$$A_0 = \begin{bmatrix} A & -BK_x & -BK_e \\ K_f CA & \begin{matrix} A-K_f C \\ -(B+K_f CB)K_x \end{matrix} & -(B+K_f CB)K_e \\ C & 0 & 1 \end{bmatrix}, \tag{3.35}$$

$$\Delta A = \begin{bmatrix} 0_{3\times 3} & -BK_x & -BK_e \\ 0_{3\times 3} & -(B+K_f CB)K_x & -(B+K_f CB)K_e \\ 0_{1\times 3} & 0_{1\times 3} & 0 \end{bmatrix}, \tag{3.36}$$

so that the closed loop system matrix is

$$A_{CL} = A_0 + \delta(k)\Delta A. \tag{3.37}$$

Since the reference input does not affect the system stability, the closed loop system (3.34) with $r=0$ is investigated as follows

$$x_{CL}(k+1) = A_{CL}(\delta(k))x_{CL}(k). \tag{3.38}$$

It is clear that A_{CL} is a linear function of $\delta(k)$, and therefore, system (3.39) is a linear parameter varying system and the robust stability can be analyzed using the approach described in [83]. This study focuses on the effect of the fuel content estimation to stability with the air flow measurement error. Note that the air flow estimation can also be improved by using the speed-density approach. From equation (3.8), δ can be expressed as follows.

$$\delta(k) = \frac{\dot{\hat{m}}_{air}(k)\alpha(k)}{\dot{m}_{air}\hat{\alpha}(k)} - 1. \tag{3.39}$$

Let ε_{air} be the percentage error bound for the charged mass air measurement. It is easy to get that

$$\delta(k) \in \begin{bmatrix}\delta_{\min} & \delta_{\max}\end{bmatrix} = \left[(1-\varepsilon_{air})\frac{\sigma_{BD}-\sigma_{DS}}{\sigma_{DS}} \quad (1+\varepsilon_{air})\frac{\sigma_{DS}-\sigma_{BD}}{\sigma_{BD}} \right]. \tag{3.40}$$

Define

$$A_1 = A_0 + \delta_{\min}\Delta A, \tag{3.41}$$

$$A_2 = A_0 + \delta_{\max}\Delta A, \tag{3.42}$$

so that the time varying matrix (3.37) can also be expressed in the following form

$$A_{CL}(\beta(k)) = \sum_{i=1}^{2} \beta_i(k) A_i, \tag{3.43}$$

where $\beta(k) \in \begin{bmatrix}\beta_1(k) & \beta_2(k)\end{bmatrix}^T$ is the vector of time-varying parameters in the unit simplex

$$\Lambda_2 = \left\{ \beta \in \mathbb{R}^2 : \sum_{i=1}^{2} \beta_i(k) = 1,\ \beta_i \geq 0,\ i = 1, 2 \right\}. \tag{3.44}$$

The rate of variation of the parameters

$$\Delta\beta_i(k) = \beta_i(k+1) - \beta_i(k),\ i = 1, 2 \tag{3.45}$$

is assumed to be limited by a priori defined bound $b > 0$ such that

$$-b \leq \Delta\beta_i(k) \leq b,\ i = 1, 2 \tag{3.46}$$

with $b \in [0,\ \ 1]$. The case $b = 0$ indicates $\beta(k)$ is frozen, so that the system becomes a linear time-invariant system. While $b = 1$ implies that $\beta(k)$ is allowed to vary arbitrarily inside Λ_2. Therefore, the bound on the variation rate of $\delta(k)$ can be expressed as

$$-b(\delta_{\max} - \delta_{\min}) \leq \delta(k+1) - \delta(k) \leq b(\delta_{\max} - \delta_{\min}). \tag{3.47}$$

Meanwhile, it is also easy to find from (3.44) and (3.45), the following is satisfied

$$\sum_{i=1}^{2} \Delta\beta_i(k) = 0. \tag{3.48}$$

To model the domain of the bound on time-difference, the vector $(\beta(k), \Delta\beta(k))^T \in \mathbb{R}^{2x2}$ can be assumed to belong to the compact set

$$\Psi_b = \left\{ \begin{array}{l} \xi \in \mathbb{R}^{2\times 2} : \xi \in co\{g^1, \cdots, g^M\}, \\ g^j = \begin{pmatrix} f^j \\ h^j \end{pmatrix}, f^j \in \mathbb{R}^2, h^j \in \mathbb{R}^2, \\ \sum_{i=1}^{2} f_i^j = 1 \; with \; f_i^j \geq 0, i = 1, 2, \\ \sum_{i=1}^{2} h_i^j = 0, \; j = 1, \cdots, M \end{array} \right\}, \tag{3.49}$$

where the vectors g^j for $j = 1, \cdots, M$ can be found to be

$$\begin{bmatrix} g^1 \cdots g^M \end{bmatrix} = \begin{bmatrix} f^1 \cdots f^M \\ \hline h^1 \cdots h^M \end{bmatrix} = \left[\begin{array}{cccccc} 1 & 1 & 0 & 0 & b & 1-b \\ 0 & 0 & 1 & 1 & 1-b & b \\ \hline 0 & -b & 0 & b & -b & b \\ 0 & b & 0 & -b & b & -b \end{array}\right] \tag{3.50}$$

with $M = 6$, see [83]. Once the columns of the set Ψ_b are defined, the convex can be expressed as

$$(\beta(k), \Delta\beta(k))^T = \sum_{j=1}^{M} \begin{pmatrix} f^j \\ h^j \end{pmatrix} \gamma_j(k), \tag{3.51}$$

where $\gamma(k) \in \Lambda_M$, and Λ_M has the similar expression as Λ_2.

Choose the Lyapunov matrix $P(\beta(k))$ and $\Omega(\beta(k))$ to have the following affine parameter-dependent structure

$$P(\beta(k)) = \sum_{i=1}^{2} \beta_i(k) P_i = \sum_{j=1}^{M} \gamma_j(k) \bar{P}_j, \tag{3.52}$$

$$\Omega(\beta(k)) = \sum_{i=1}^{2} \beta_i(k) \Omega_i = \sum_{j=1}^{M} \gamma_j(k) \bar{\Omega}_j, \tag{3.53}$$

where $\bar{P}_j = \sum_{i=1}^{2} f_i^{\,j} \bar{P}_i$, and $\bar{\Omega}_j = \sum_{i=1}^{2} f_i^{\,j} \bar{\Omega}_i$. Similarly, $A_{CL}(\beta(k))$ also can be converted as

$$A_{CL}(\beta(k)) = \bar{A}_{CL}(\gamma(k)) = \sum_{j=1}^{M} \gamma_j(k) \bar{A}_j \tag{3.54}$$

with $\bar{A}_j = \sum_{i=1}^{2} f_i^{\,j} A_i$. According to reference [83], if there exist, for $j = 1, \cdots, M$, matrices $\bar{\Omega}_j \in \mathbb{R}^{n \times n}$ and, for $i = 1, 2$, symmetric positive-definite matrices $P_i \in \mathbb{R}^{n \times n}$ such that

$$\begin{bmatrix} \sum_{i=1}^{2} (f_i^{\,j} + h_i^{j}) P_i & \bar{A}_j \bar{\Omega}_j \\ \bar{\Omega}_j^{\,T} \bar{A}_j^{\,T} & \bar{\Omega}_j + \bar{\Omega}_j^{\,T} - \sum_{i=1}^{N} f_i^{\,j} P_i \end{bmatrix} > 0 \tag{3.55}$$

for $j = 1, \cdots, M$ and

$$\begin{bmatrix} \sum_{i=1}^{2} (f_i^{\,j} + f_i^{\,l} + h_i^{j} + h_i^{l}) P_i & \bar{A}_l \bar{\Omega}_j + \bar{A}_j \bar{\Omega}_l \\ \bar{\Omega}_j^{\,T} \bar{A}_l^{\,T} + \bar{\Omega}_l^{\,T} \bar{A}_j^{\,T} & \Theta_{jl} \end{bmatrix} > 0 \tag{3.56}$$

with $\Theta_{jl} = \bar{\Omega}_j + \bar{\Omega}_j^T + \bar{\Omega}_l + \bar{\Omega}_l^T - \sum_{i=1}^{2} (f_i^{\,j} + f_i^{\,l}) P_i$ for $j = 1, \cdots, M-1$ and $l = j+1, \cdots, M$, then system (3.39) is exponentially stable.

3.5 Model Calibration and Simulation Validation

3.5.1 Engine dynamometer test setup

The proposed LQ tracking control with adaptive estimation was validated on a lean burn SI flex fuel engine. The specifications of the target single cylinder are listed in Table 3-1.

Table 3-1: Engine system parameters

Engine displacement	0.4 liter
Compression Ratio	12.5
Engine Speed	1500 rpm
σ_{DS} (gasoline)	14.6
σ_{DB} (E85)	9.7
τ_1	0.08 second
τ_2	0.06 second
τ_3	0.2 second

Figure 3-3 Engine dynamometer setup shows the engine dynamometer test setup used for generating engine model calibrations and closed loop control tests. The engine has a DI fuel injection system. Two fuel tanks, one filled with gasoline and the other filled with E85, were connected to a fuel pipe line through a fuel switch valve as illustrated in Figure 3-4. Both fuel tanks were regulated at 5 MPa by two high pressure Nitrogen bottles. The engine was operated at 1500 rpm with 5 bar IMEP (indicated mean effective pressure). The engine responses were recorded by the A&D combustion analysis system (CAS). Table 3-1 lists the calculated engine model parameters obtained from the test data.

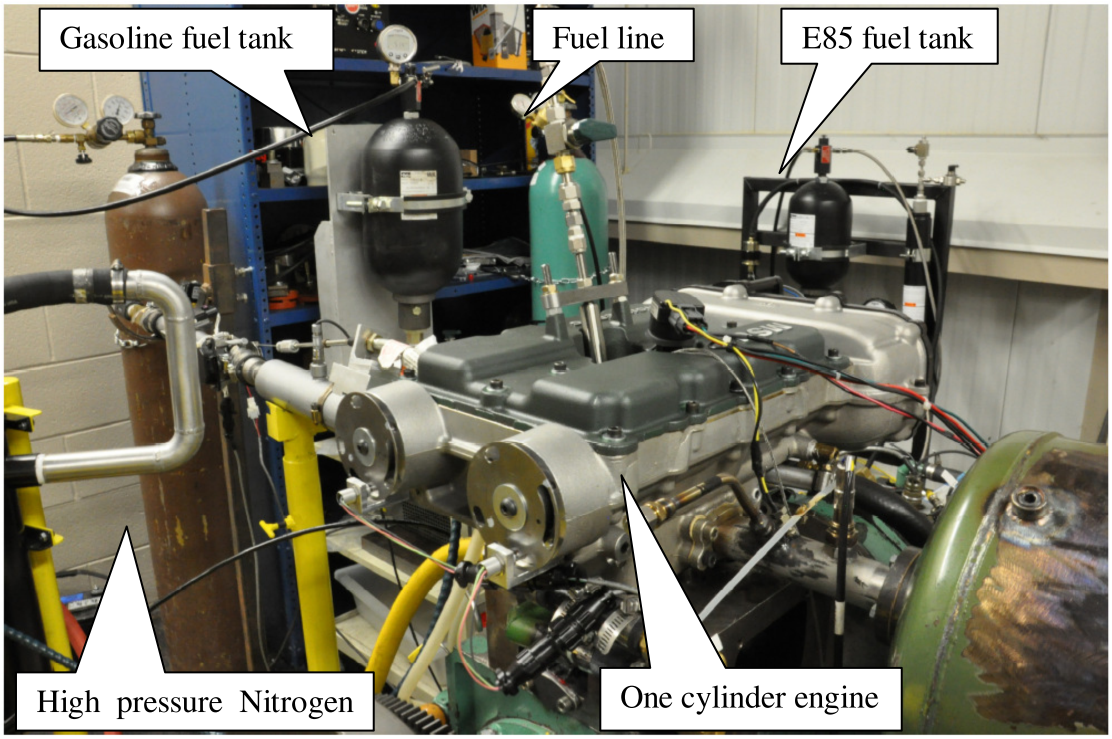

Figure 3-3 Engine dynamometer setup

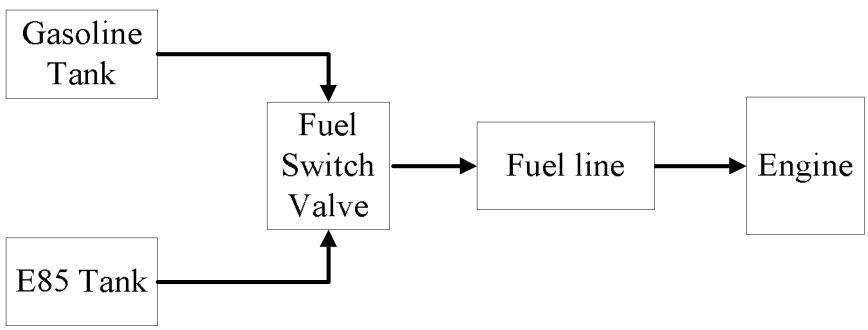

Figure 3-4 Fuel system diagram

3.5.2 Stability validation

Table 3-2 lists the values of the parameters used for the controller design. The excitation noise covariance matrices W and V were selected assuming that the exciting noise w is usually much larger than the measurement noise v. The LQ control weighting matrices Q and R were selected based upon the closed loop system response time and its relative stability.

Table 3-2: Control parameters

Q	R	W	V
$\begin{bmatrix} 1 & 0.012 & 0.012 & 0.012 \\ 0.012 & 1 & 0.012 & 9.6 \\ 0.012 & 0.012 & 250 & 60 \\ 0.012 & 9.6 & 60 & 2.6 \end{bmatrix}$	100	1	0.0005

The resulting Kalman state estimation gain is

$$K_f = [4.0543\ 3.2287\ 0.6467]^T \tag{3.57}$$

and the resulting controller is given as below,

$$\begin{aligned} K_x &= [0.3426\ 0.2944\ 1.1345] \\ K_e &= 0.1526 \\ K_r &= 2.2992 \end{aligned} \tag{3.58}$$

The system stability analysis was completed by finding the feasible solutions for equations (3.55) and (3.56) using the Matlab LMI toolbox. Two positive definite symmetric matrices P_1 and P_2 were found with b equal to 1, see (3.59). The result indicates that $\beta(k)$ is allowed to vary arbitrarily fast inside Λ_2, which consequently leads to the conclusion that $\delta(k)$ can vary arbitrarily for $\delta(k) \in [\delta_{\min} \quad \delta_{\max}]$ based upon (3.47). The system robust stability is guaranteed even when the fuel content is changed from one fuel (gasoline) to the other (E85) in one time step. This is almost impossible in reality.

$$P_1 = \begin{bmatrix} 0.40 & -0.05 & -0.06 & 0.23 & 0.05 & -0.08 & -0.03 \\ -0.05 & 0.55 & -0.08 & 0.15 & 0.23 & -0.01 & -0.10 \\ -0.06 & -0.08 & 0.07 & -0.02 & -0.03 & 0.05 & -0.13 \\ 0.23 & 0.15 & -0.02 & 1.28 & 0.48 & 0.04 & -0.12 \\ 0.05 & 0.23 & -0.03 & 0.48 & 0.85 & 0.04 & -0.12 \\ -0.08 & -0.01 & 0.05 & 0.04 & 0.03 & 0.07 & -0.12 \\ -0.03 & -0.10 & -0.13 & -0.12 & -0.09 & -0.12 & 1.44 \end{bmatrix} \tag{3.59}$$

$$P_2 = \begin{bmatrix} 0.39 & -0.05 & -0.06 & 0.26 & 0.10 & -0.07 & -0.03 \\ -0.05 & 0.55 & -0.08 & 0.14 & 0.23 & -0.01 & -0.10 \\ -0.06 & -0.08 & 0.07 & -0.01 & -0.03 & 0.05 & -0.13 \\ 0.26 & 0.14 & -0.01 & 1.30 & 0.48 & 0.04 & -0.13 \\ 0.10 & 0.23 & -0.03 & 0.48 & 0.83 & 0.03 & -0.09 \\ -0.07 & -0.01 & 0.05 & 0.04 & 0.03 & 0.07 & -0.12 \\ -0.03 & -0.10 & -0.13 & -0.13 & -0.09 & -0.12 & 1.44 \end{bmatrix}$$

For the practical applications, the engine transport delay and exhaust manifold filling dynamics are parameter-varying. To be more specific, the transport delay and the exhaust manifold filling dynamics can be modeled as a function of engine speed and they can be approximated as follows,

$$\tau_1 = \tau_{10} \times \frac{1500}{N_{eng}} \tag{3.60}$$

$$\tau_2 = \tau_{20} \times \frac{1500}{N_{eng}} \tag{3.61}$$

where N_{eng} is the current engine speed, τ_{10} and τ_{20} are the time constant values for the engine transport delay and the exhaust manifold filling dynamics when the engine is operated at 1500 rpm.

In order to show that the closed loop system is stable under varying engine speed, the closed loop system robust stability under varying fuel gain estimation errors and engine speeds was studied. The engine speed was varied between 600 and 5500 rpm. In this case the parameter varying region of the closed loop matrix A_{CL} was defined as shown in Figure 3-5. Using the same stability analysis approach [83] as the one variable case, four positive definite symmetric matrices $P_{i=3\cdots6}$ were found for b equal to 1, which indicates that the system is robustly stable when both transport delays (τ_1 and τ_2 due to varying engine speed) and the fuel content estimation error vary in full range within one sample period. Matrices $P_{i=3\cdots6}$ .can be found in (3.62). For an alternative solution, a LPV (linear-parameter-varying) control can be designed to guarantee the stability and performance.

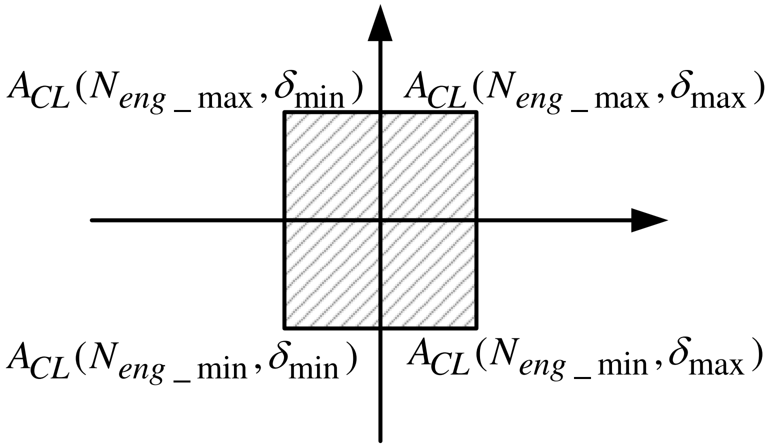

Figure 3-5 Closed loop system matrix A_{CL} varying bound

$$P_3 = 10^{-8} * \begin{bmatrix} 0.38 & 0.16 & -0.16 & 0.40 & 0.19 & -0.12 & 0.33 \\ 0.16 & 0.38 & -0.22 & 0.04 & 0.30 & -0.16 & 0.87 \\ -0.16 & -0.22 & 1.01 & -0.00 & -0.16 & 0.88 & -6.09 \\ 0.40 & 0.04 & -0.00 & 0.69 & 0.11 & 0.01 & -0.86 \\ 0.19 & 0.30 & -0.16 & 0.11 & 0.39 & -0.11 & 0.38 \\ -0.12 & -0.16 & 0.88 & 0.01 & -0.11 & 0.77 & -5.34 \\ 0.33 & 0.87 & -6.09 & -0.86 & 0.38 & -5.34 & 43.85 \end{bmatrix} \tag{3.62}$$

$$P_4 = 10^{-8} * \begin{bmatrix} 0.37 & 0.14 & -0.15 & 0.41 & 0.17 & -0.12 & 0.15 \\ 0.14 & 0.36 & -0.20 & -0.03 & 0.28 & -0.15 & 0.55 \\ -0.15 & -0.20 & 0.97 & -0.01 & -0.15 & 0.84 & -5.84 \\ 0.41 & -0.03 & -0.01 & 0.84 & 0.06 & 0.02 & -0.76 \\ 0.17 & 0.28 & -0.15 & 0.06 & 0.38 & -0.11 & 0.23 \\ -0.12 & -0.15 & 0.84 & 0.02 & -0.11 & 0.73 & -5.13 \\ 0.15 & 0.55 & -5.84 & -0.76 & 0.23 & -5.13 & 42.88 \end{bmatrix}$$

$$P_5 = 10^{-8} * \begin{bmatrix} 0.31 & 0.06 & -0.13 & 0.43 & 0.10 & -0.10 & -0.02 \\ 0.06 & 0.23 & -0.20 & -0.01 & 0.02 & -0.16 & 0.66 \\ -0.13 & -0.20 & 1.14 & 0.01 & -0.14 & 0.98 & -6.90 \\ 0.43 & -0.01 & 0.01 & 0.88 & 0.09 & 0.03 & -1.04 \\ 0.10 & 0.20 & -0.14 & 0.09 & 0.26 & -0.10 & 0.21 \\ -0.10 & -0.16 & 0.98 & 0.03 & -0.10 & 0.86 & -6.04 \\ -0.02 & 0.66 & -6.90 & -1.04 & 0.21 & -6.04 & 49.63 \end{bmatrix}$$

$$P_6 = 10^{-8} * \begin{bmatrix} 0.27 & 0.07 & -0.11 & 0.38 & 0.10 & -0.09 & -0.18 \\ 0.07 & 0.23 & -0.21 & -0.01 & 0.02 & -0.16 & 0.76 \\ -0.11 & -0.21 & 1.11 & 0.04 & -0.15 & 0.96 & -6.76 \\ 0.38 & -0.01 & 0.04 & 0.84 & 0.09 & 0.06 & -1.31 \\ 0.10 & 0.20 & -0.15 & 0.09 & 0.27 & -0.11 & 0.29 \\ -0.09 & -0.16 & 0.96 & 0.06 & -0.11 & 0.84 & -5.91 \\ -0.18 & 0.76 & -6.76 & -1.31 & 0.29 & -5.91 & 48.89 \end{bmatrix}$$

Note that above conclusion is reached based upon the control gain given in equation (3.58). However, if we redesign the state estimator for system (3.10) by placing the poles at

$$[0.90\ 0.89\ 0.88], \tag{3.63}$$

and change the control gain for system (3.22) by placing the poles at

$$[0.94\ 0.86\ 0.85\ 0.84], \tag{3.64}$$

it is infeasible to find the two positive definite symmetric matrices P_1 and P_2 when b is equal or greater than 0.72. This indicates that the closed loop system with adaptive estimation may not be stable if the estimation and control gain is not properly chosen.

3.5.3 Simulations results

For lean burn engine simulations, the AFR is not controlled in a closed loop except during the LNT regeneration, while the Kalman state estimation updates the estimated state vector under all engine operational conditions. The LNT regeneration enabling threshold and actuator saturation were not considered for this study. Instead, a recorded lean burn engine AFR signal was used as the reference AFR input, along with the mass air flow signal. Three adaptive estimation schemes were used in the simulations as follows:

1) Regular scheme: the fuel content estimation is updated for adaptive control with one adaptive gain all the time.
2) Semi-active scheme: the fuel content estimation is active only during the LNT regeneration process.
3) Dual-gain scheme: same as the regular scheme except that two adaptive estimation gains are used, where the small gain is used under the open loop AFR operation and the large gain during the LNT regeneration.

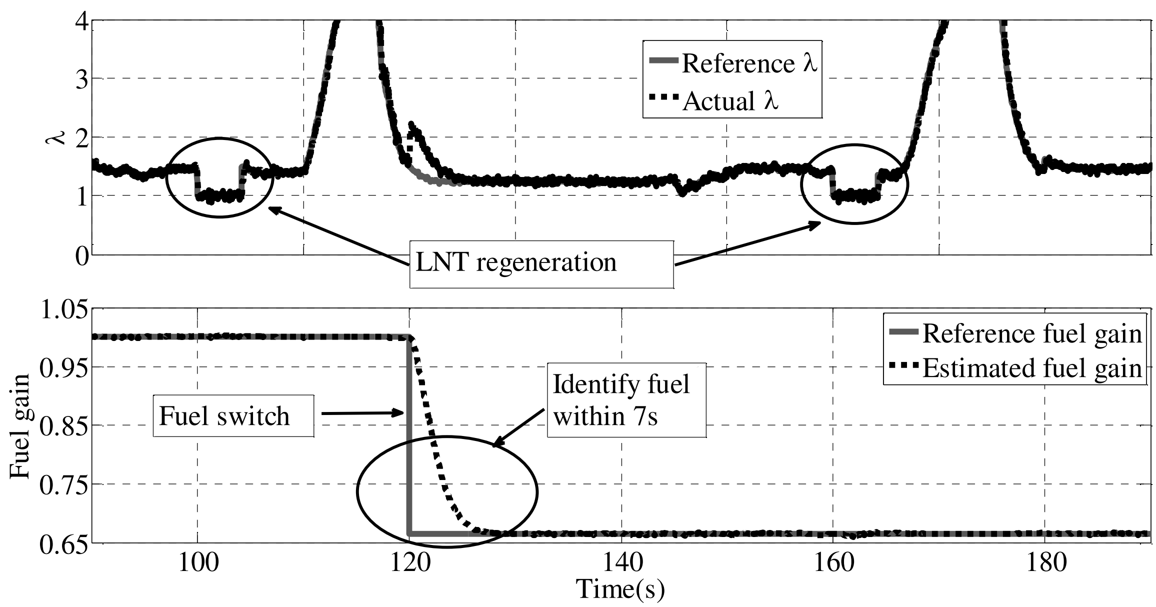

Figure 3-6 Regular scheme with the oxygen sensor on the engine ($\tau_3 = 0.2$)

The remaining section studies the three adaptive schemes. For simplicity, the engine equivalence (fuel-to-air) ratio Φ was converted into the normalized air-to-fuel ratio λ in the simulation plots. Note that $\Phi = 1/\lambda$. To simulate the injector shot-to-shot variation and AFR sensor measurement noise, 3% white noise was added to the injected fuel quantity and 5% white noise to the AFR sensor output.

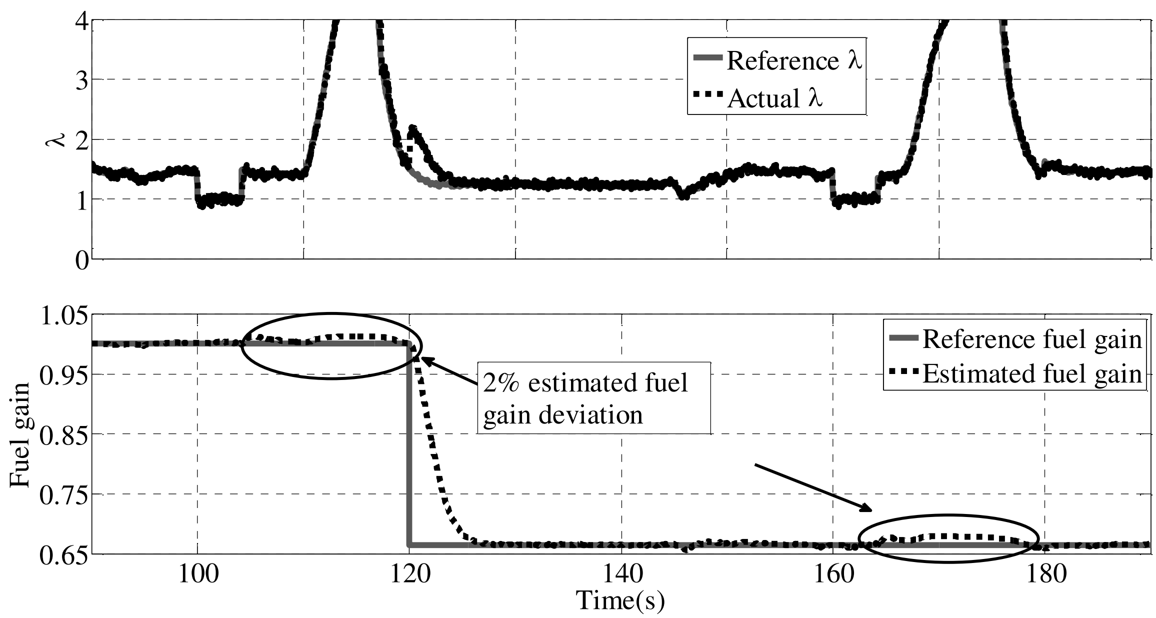

Figure 3-7 Regular scheme with an aged oxygen sensor ($\tau_3 = 0.3$)

Figure 3-6 shows the simulation results of the regular scheme (scheme 1) with the measured oxygen sensor time constant $\tau_3 = 0.2$. The adaptive gain Γ was chosen to be 0.015. The engine was operated under the open loop AFR operation for most of the time, and the four-second LNT regeneration occurred every 60 seconds. During the regeneration, the normalized AFR was controlled in a closed loop and was regulated to be slightly less than one. Gasoline was used at the start of the simulation and was switched to E85 at 200$^{\text{th}}$ second. Since the adaptive estimation was always active, the biofuel content was identified within 7 seconds after the fuel switch. However, with the aged oxygen sensor that adds additional modeling error for the adaptive estimation, the selected adaptive gain ($\Gamma = 0.015$) might be too big to have stable biofuel gain estimation. Figure 3-7 shows the simulation results with an aged oxygen sensor ($\tau_3 = 0.3$), where the fuel content estimation error increases during the transient AFR operations.

In order to reduce the adaptive estimation error during the open loop AFR operation, the second adaptive control scheme (semi-active scheme) estimates the fuel content only during the LNT regeneration with the same adaptive gain as that used in scheme 1 (regular scheme); see Figure 3-8 for the simulation results. It can be observed that the biofuel content converges in several seconds after the LNT regeneration period begins. The advantage of this scheme is that the adaptive estimation is stopped during the open loop AFR operation to eliminate estimation error during the transient AFR operation, however, the disadvantage is that the fuel content is not updated until the next LNT regeneration period, which could lead to large engine fuel and torque control error. Note that accurate engine torque control is very important for hybrid powertrains.

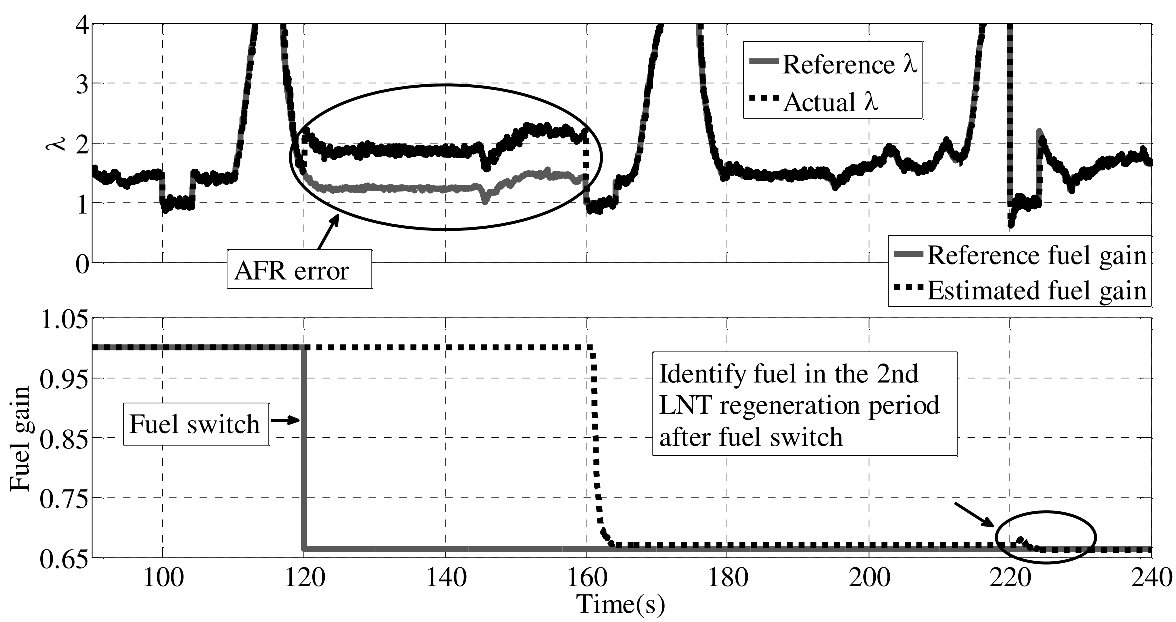

Figure 3-8. Semi-active scheme with an aged oxygen sensor ($\tau_3 = 0.3$)

The third adaptive control scheme (dual-gain scheme) combines the advantages of the previous two schemes. It uses a small adaptive estimation gain ($\Gamma = 0.005$ for this simulation) during the open loop AFR operation and a large adaptive estimation gain ($\Gamma = 0.015$) during the LNT regeneration period. Figure 3-9 shows the simulation results of the dual-gain scheme. The AFR represented by the dotted line is the fuel gain estimated under the same conditions as these in Figure 3-8. It is obvious that the small adaptive gain used during the open loop AFR operation is capable of providing an accurate estimation of the fuel content before the next regeneration event even though the convergence is slow. Note that in an actual engine operation, the fuel content change will not be in a step and it will vary relatively slowly. This can be found in the next section. Therefore, the performance of the third adaptive control scheme could be better.

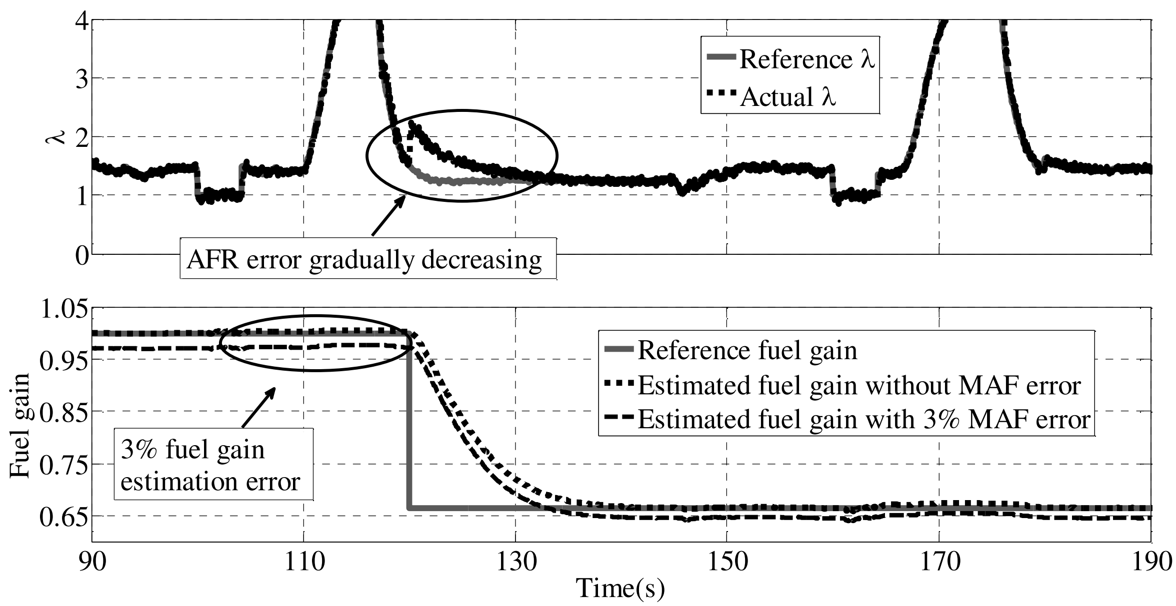

Figure 3-9. Dual-gain scheme with an aged oxygen sensor ($\tau_3 = 0.3$)

The AFR trace represented by the dashed line in Figure 3-9 is the estimated fuel content with 3% mass air flow sensor error, leading to about 3% fuel content estimation error

3.6 Engine Dynamometer Validation

The fuel content transition process for experimental validation was designed to start with one type of fuel (for instance, gasoline), and then with the fuel switched to the other (for instance, E85) in the middle of the test. After the fuel is switched, two types of fuel are mixed in the fuel line around the fuel switch valve and eventually the fuel line is filled with the second fuel. Correspondingly, three combustion stages can be clearly observed through the estimated fuel gain: a) combustion with the first fuel, b) the transition combustion with the mixed two fuels, and c) combustion with the second fuel. The engine throttle was fixed for all tests. Also, since the experimental validation is centered at the AFR control during the LNT regeneration, the engine torque balance was not considered. As a result, the engine spark timing was fixed during the test; otherwise, it could be controlled to keep the engine torque output constant during the LNT regeneration. Similar to the simulations in the previous sections, the closed loop reference AFR was set to 1.0 during the closed loop LNT regeneration, and the open loop reference was set to 1.3 when the engine is not in the LNT regeneration mode. In order to avoid the interaction between transient AFR control and adaptive estimation, the fuel content estimation was disabled during AFR transition for the first 0.6 seconds. The adaptive estimation gain used in the experiments was retuned such that the fuel content fluctuation was minimized under the fixed fuel content with the fastest convergence rate. Note that the retuned adaptive estimation gains are smaller than these used in the simulations due to additional mass-air-flow sensor noise that was not considered in simulations.

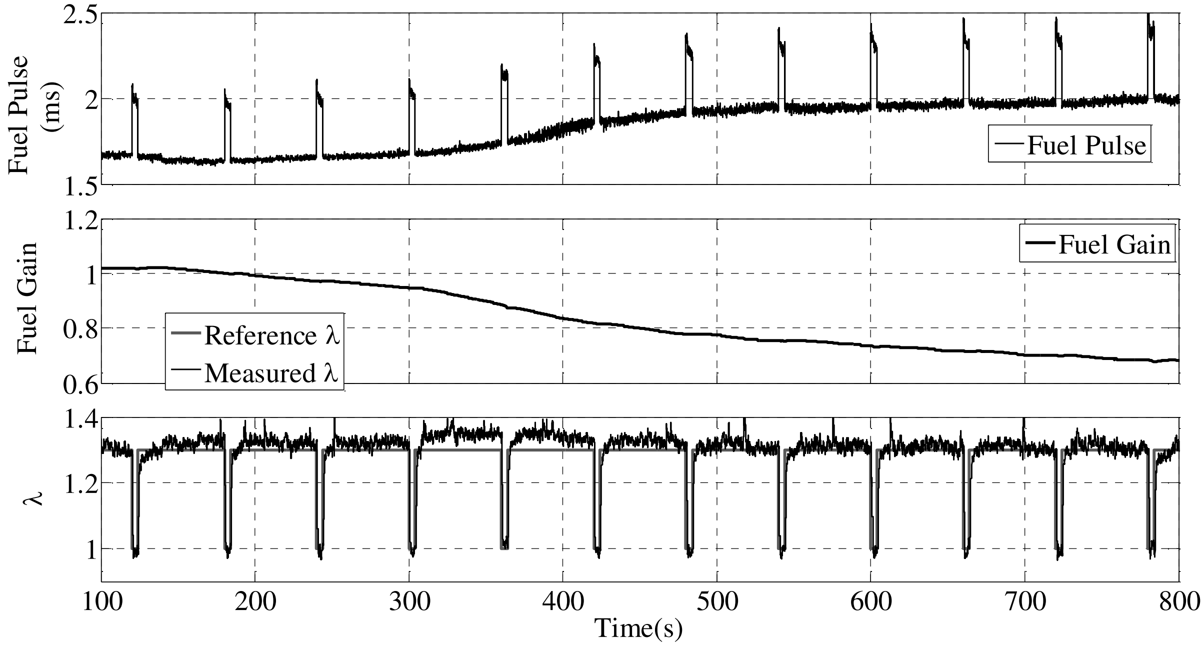

Figure 3-10. a Single adaptive gain for fuel transit from gasoline to E85

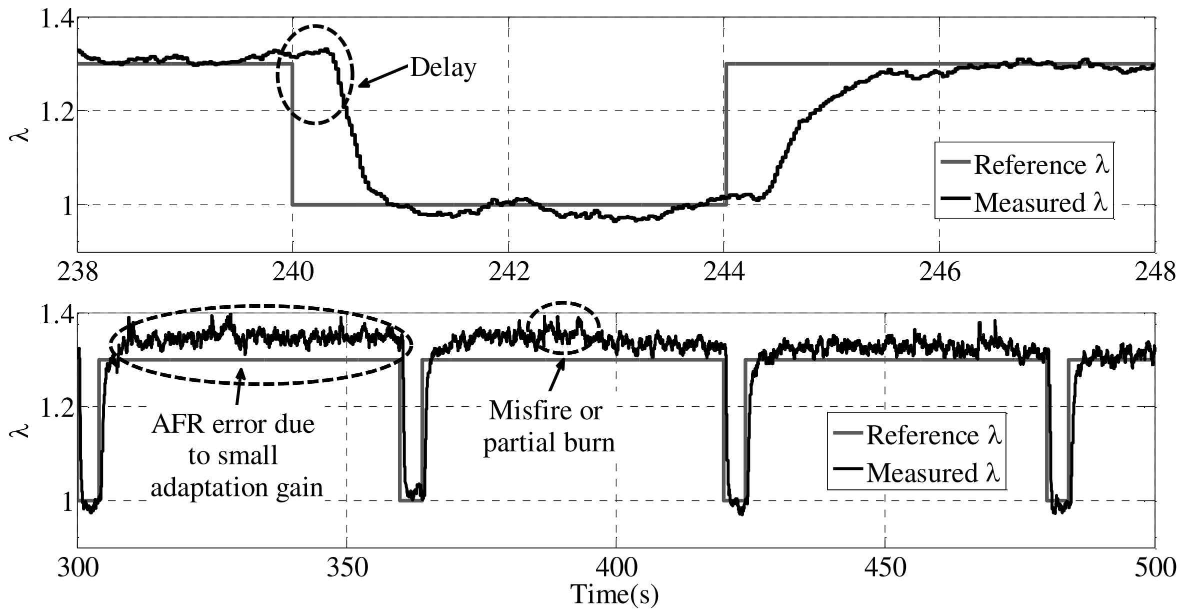

Figure 3-10.b Single adaptive gain for fuel transit from gasoline to E85

The engine dynamometer test started with one adaptive gain scheme with $\Gamma = 0.0025$. Figure 3-10 a-b illustrates the test for the fuel transition from gasoline to E85. The entire transition lasted for about 700 seconds. In Figure 3-10.a, it can be observed that the entire transition consists of three periods, slow, then fast, then slow. With about 40% of the fuel content transition was accomplished during the fast transition period, which is from 300th to 400th second. Due to the adaptive estimation error, the AFR control error exists especially during the open loop control period. Figure 3-10.b shows the details of the AFR signal from 238th to 248th second and from 350th to 500th second. It is easy to see that the measured AFR closely followed the reference signal during the LNT regeneration period due to closed loop control, while during the open loop AFR operation, there was some misfire or partial burn occurred due to the lean limit of the SI engine combustion caused by the fuel estimation error. The key observation from Figure 3-10 is that the majority of the fuel content transition occurs during the open loop AFR operation period. Therefore, it is very important to use appropriate adaptive gain to estimate the fuel content during the open loop AFR operation.

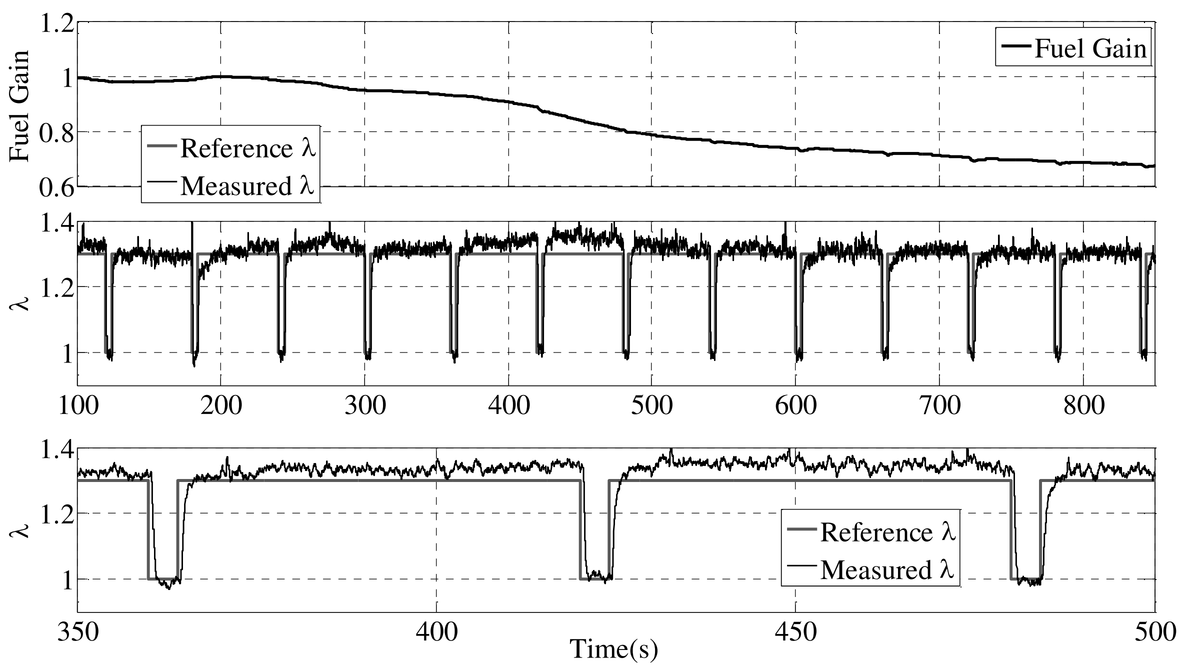

Figure 3-11 Dual adaptive gain for fuel transit from gasoline to E85

Figure 3-11 provides the test results for the dual-gain scheme. Since most of the fuel transition was completed during the open loop AFR operation, the closed loop adaptive gain was kept at 0.0025, while the open loop gain was set at 0.005. The experimental results show certain performance improvement, but the large estimation error exists during the transition.

In order to improve the fuel content estimation performance during the open loop operation, the gain-scheduling scheme for adaptive estimation was proposed. Table 3-3 shows the tuned adaptive gain with respect to AFR error. The corresponding simulation results are shown in Figure 3-12. It can be seen that, with the scheduled adaptive gain, the time for the fuel gain to converge is significantly reduced compared to the dual-gain scheme in Figure 3-9. And the dynamometer test demonstrates a similar improvement as shown in Figure 3-13.

Table 3-3 Scheduled adaptive gain

λ error	0	0.01	0.02	0.03	0.04	0.05
Adaptive gain	1e-4	2.5e-4	5e-4	6.2e-3	0.0125	0.0125

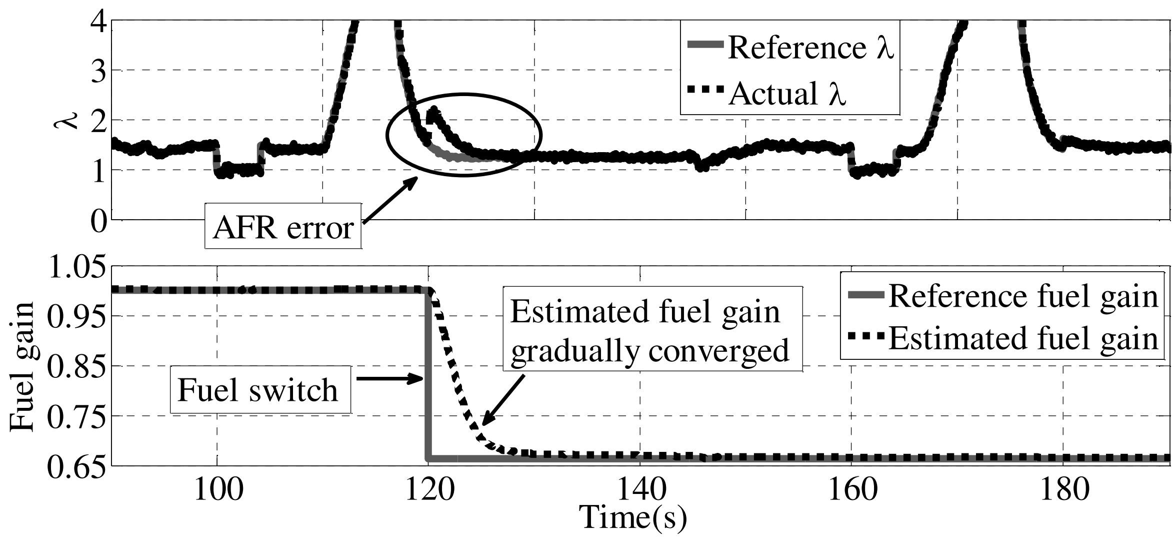

Figure 3-12 Gain scheduling scheme with an aged oxygen sensor ($\tau_3 = 0.3$)

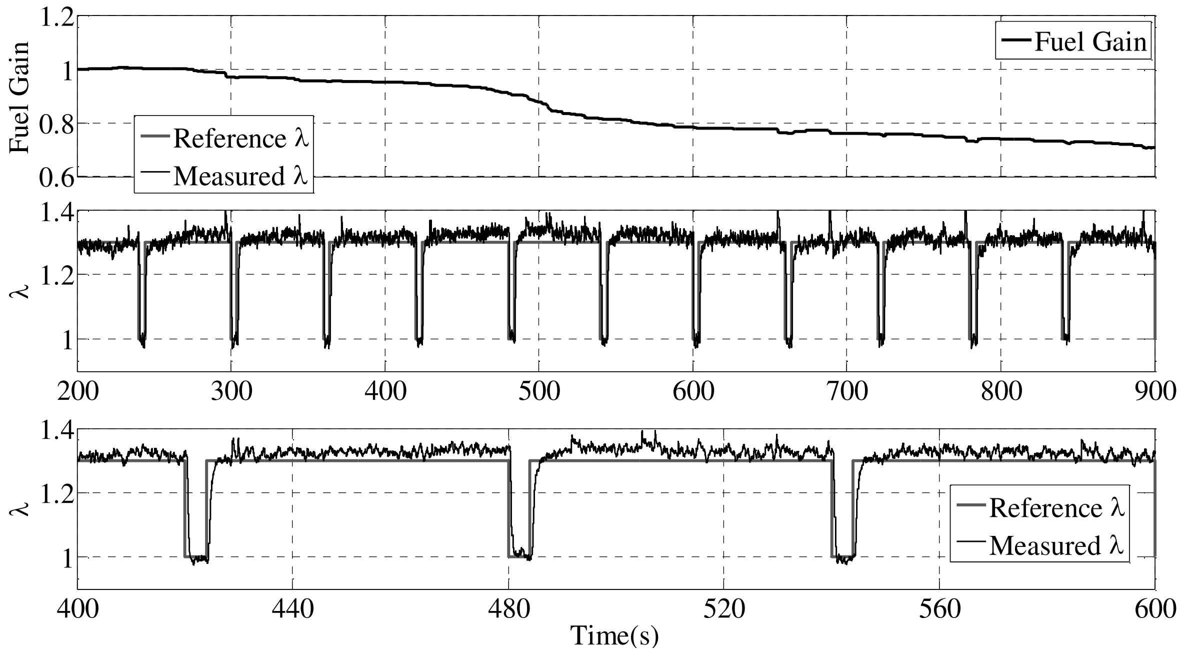

Figure 3-13 Gain scheduling for fuel transit from gasoline to E85

In order to have a quantitative comparison among the three adaptive schemes used in the test, the mean absolute deviation (MAD) of the AFR error of each scheme was calculated and provided in Table 3-4.

Table 3-4 AFR mean absolute deviation

	One gain	Two gain	Gain scheduling
MAD	0.02777	0.02594	0.02476

Finally, the same gain-scheduling adaptive scheme was also tested for the fuel transition from E85 to gasoline. Figure 3-14 illustrates the test result with the same scheduled adaptive gains. Compared with the fuel transition from gasoline to E85, the transition from E85 to gasoline has a much faster initial transition period. It only took 25 seconds for the fuel gain to transition from 0.67 to 0.83, while it took nearly 600 seconds to complete the rest of the fuel transition. This could be due to the fact that E85 has higher viscosity than gasoline. As a summary, the dynamometer experiment results show that the proposed LQ optimal controller with the gain-scheduling adaptive scheme provides the best fuel content estimation with the accurate AFR tracking during the LNT regeneration.

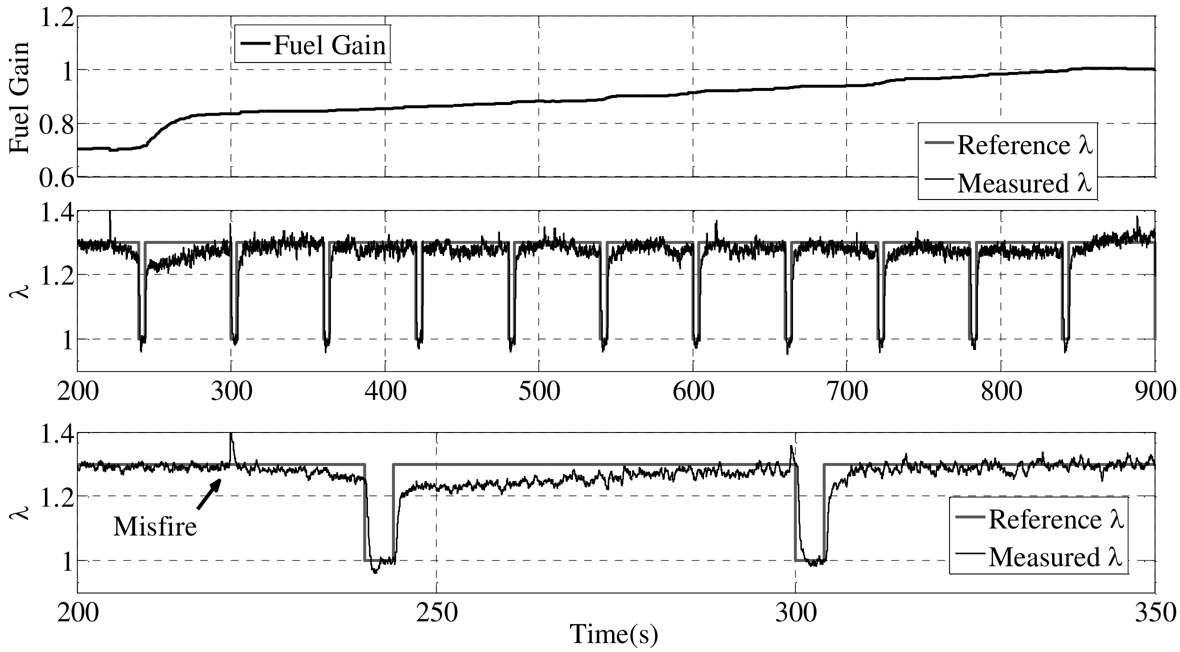

Figure 3-14 Gain scheduling for fuel transit from E85 to gasoline

3.7 Conclusions

This research proposes to use the LQ optimal tracking scheme to regulate the air-to-fuel ratio (AFR) of a biofuel lean burn engine during the lean NOx Trap (LNT) regeneration period based upon the adaptively estimated biofuel content. The robust stability of the closed loop system with adaptive estimation can be analyzed based upon the framework of the linear parameter varying systems. Several adaptive control schemes were studied through both simulation and dynamometer experiments. The results show that the proposed LQ tracking control with the gain-scheduling adaptive estimation provided the best fuel estimation performance (minimal AFR error) and demonstrated the ability to regulate the AFR during the

LNT regeneration for a flex fuel lean burn engine. It was also found that the fuel transition from E85 to gasoline is much faster than the same process from gasoline to E85 for the same configuration.

CHAPTER 4 DETECTING MFB75 AND BIODIESEL BLEND USING A KNOCK SENSOR

4.1 Introduction

Detect the combustion phase of diesel engines is of great interest to researchers, since it can be used as feedback signal for closed loop combustion control to improve fuel efficiency and reduce the exhaust emissions of a diesel engine. In particular, the estimation of the start of combustion (SOC), which occurs shortly after the fuel injection, attracts the most attention. The techniques that can be used to estimate the SOC in diesel engines include using a high speed camera to capture the first appearance of the visible flame, and measuring the sudden rise in-cylinder pressure or temperature caused by the combustion [90]-[92]. However, these detection technologies can only be used in the lab environment due to the high cost and low sensor durability.

Over the past decades, numerous efforts have been devoted to developing the numerical models of the ignition delay, defined as the time interval between the start of injection (SOI) and the SOC. The combustion ignition delay consists of a physical delay and a chemical delay. The physical delay includes the time required for fuel atomization, vaporization and mixing with the air, whereas the chemical delay denotes the processes of pre-combustion reactions of the fuel, air, and residual gas mixture which lead to auto-ignition [90]. In general, these numerical ignition delay models were developed as a function of the mixture pressure, temperature, and composition [93]-[97], and the most commonly used model is based upon the Arrhenius function similar to what was proposed by Wolfer [93] as below,

$$\tau_{id} = AP^{-n} \exp\left(\frac{E_a}{R_u T}\right), \tag{4.1}$$

where P and T are in-cylinder pressure and temperature respectively; E_a is activation energy; R_u is universal gas constant; A and n are calibration parameters. However, those models showed limited predictive ability of ignition delay, compared to experimental results.

As a result, many studies have turned to finding a low cost sensor for SOC detection and estimation. Among them, the traditional knock sensor has been considered as a promising candidate due to its intrinsic relations between the combustion pressure wave and the vibration signals [98]. Reference [99] proposes the use of the wavelet transform of the engine knock signal to detect the SOC. Reference [100] proposes an approach to detect the SOC using the envelop of the knock sensor signal. The knock sensor was also used as an indicator of the SOC for HCCI engines [101]. However, further investigation shows that the knock signal is usually very weak at SOC due to its low sensitivity. Therefore, reference [102] used a lab grade accelerometer sensor for detecting the SOC.

Since SOC is defined as the crank location when 1% fuel is burned, the actual SOC is very difficult to detect due to the early stage of the combustion. Therefore, many studies use the 10% of the mass fraction burned (MFB10) location as the indication of SOC [103], [104]. However, the combustion phase detection robustness can be improved by correlating the knock signal to the combustion phase where rapid combustion occurs. In this case, high signal to noise ratio estimation can be achieved. This study proposes estimating the 75% of the mass fraction burned (MFB75) location using the knock signal.

Two traditional knock sensors (used on 2012 GM Cruze) and one instrumentation accelerometer sensor (Omega ACC793) were used during the study to detect the MFB75. It turns out that the sensitivity of the traditional knock sensor is good enough for this application, which provides a low cost alternative for combustion phase detection. The integration of the knock sensor signal over fixed crank angles was used as the indicator of the knock intensity, while the difference of the knock integration over each crank angle was used to detect the MFB75 location. Two types of fuel, petroleum diesel (B0) and Canola based biodiesel (B100) [3], as well as their blend (B50), were investigated. As a result, the proposed method indicates that MFB75 can be detected consistently.

Besides the study of the combustion phase detection using knock signal, the feasibility of using the knock sensor signal to identify the biodiesel content was also investigated in this study. Note that different biodiesel content leads to different cetane number (CN),which results in different combustion process, such as different SOC, burn rate, burn duration, and so on [67]-[69]. Therefore, in order to optimize the combustion process for biodiesel engines, it is necessary to estimate the blend of the biodiesel in real time. The existing approaches of detecting fuel content are based upon oxygen sensors [105], in-cylinder pressure sensors [7], ionization sensors [8], and the ionic polymer-metal composite beam flow sensor [71]. In this study, three fuel blends, B0, B50, and B100 were used during the combustion tests using a single optical cylinder diesel engine. Note that Canola has higher CN than petroleum diesel. The biodiesel content was estimated based upon the knock integration. The test results show a clear difference between B0 and B50, whereas the difference between B50 and B100 is not as obvious. It was also observed that the estimated MFB75 locations can also be used for fuel blend estimation since biodiesel content also affects the combustion phase. The future work includes the investigation of biodiesel content detection using combined criteria of knock intensity integral and difference (the estimated MFB75).

The rest of this chapter is organized as follows. Section II introduces the engine experiment setup; Section III presents the relationship between knock signal and the combustion phase correlated using the high speed combustion images. The developed MFB75 detection method, as well as the estimated results, is presented in Section IV. The analysis results of the fuel content detection using the knock senor signal is discussed in Section V. Section VI adds the conclusions and the future work.

4.2 Combustion Experiment Setup

Table 4-1: Engine specifications

Bore	95	mm
Stroke	105	mm
Displacement	0.75	liter
Cylinder Number	1	unit
Compression Ratio	17:1	unit

The engine combustion experiments were conducted using a single cylinder optical diesel engine as shown in Fig 1. The engine specifications are listed in Table 4-1. The intake manifold pressure and the intake air temperature were maintained at 1.35 bar and 25˚C, respectively. Note that no external EGR (exhaust gas recirculation) was used in this study. The diesel injector, used in the test, was a Siemens piezo injector using a 6-hole nozzle with holes of 0.185mm with a cone angle of 154 degrees, and the fuel pressure in the common rail was regulated at 125 MPa. One lab grade accelerometer sensor and one knock sensor were mounted directly on the cylinder wall as shown in Fig 2 to minimize the mechanical vibration noise introduced by other engine moving parts. The other knock sensor was positioned on the cylinder head. The in-cylinder pressure signal was measured by a Kistler pressure transducer. All combustion data including knock and pressure signals were recorded by a baseline CAS (Combustion Analysis System) from AND Technologies, and all the signals were sampled at 60kHz.

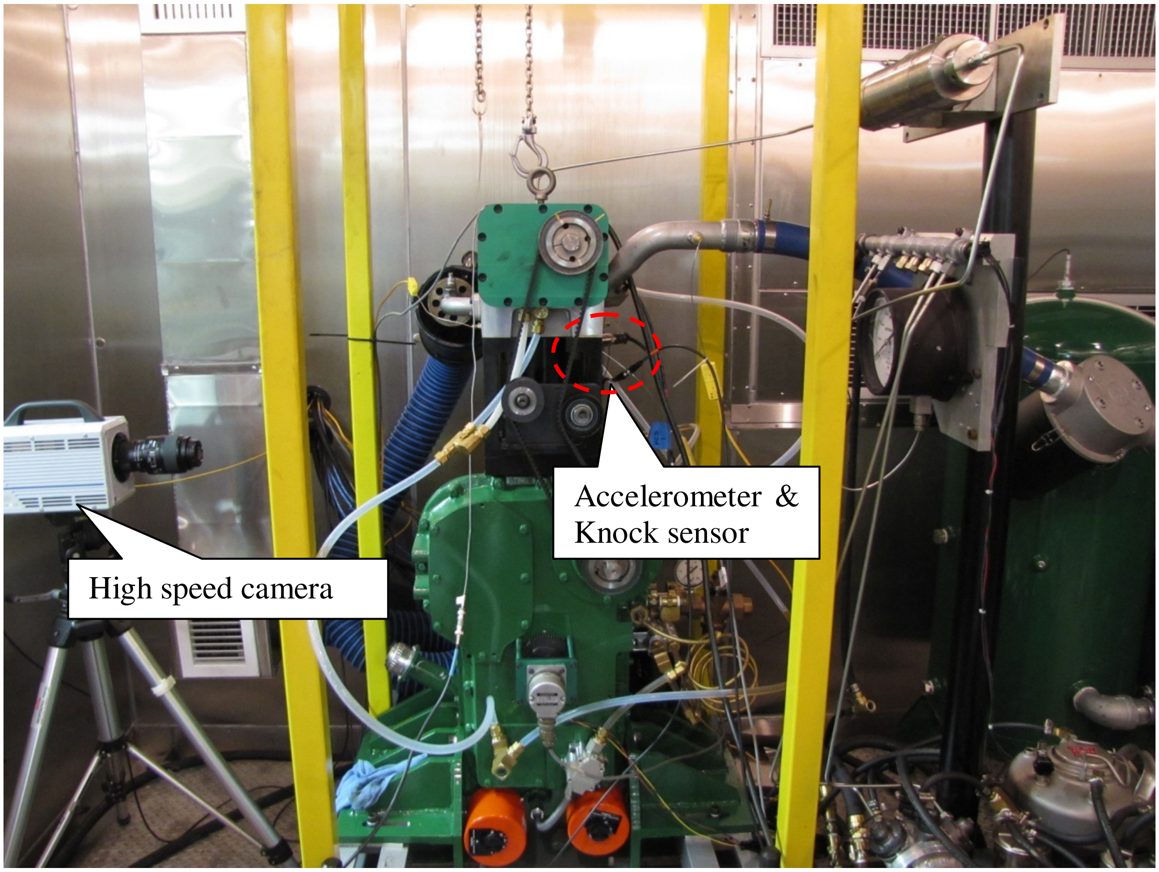

Figure 4-1. Engine dynamometer test setup

The tests were conducted at two engine speeds, 1200 rpm and 1500 rpm. The engine load was maintained at 5 bar IMEP (indicated mean effective pressure) by adjusting the fuel injection pulse width. Two types of fuel injection modes, main injection only and main injection with pilot injection, were used during the study. In order to study the knock sensor responses to different knock intensities, injection timing was changed while the fuel injection pulse was kept constant.

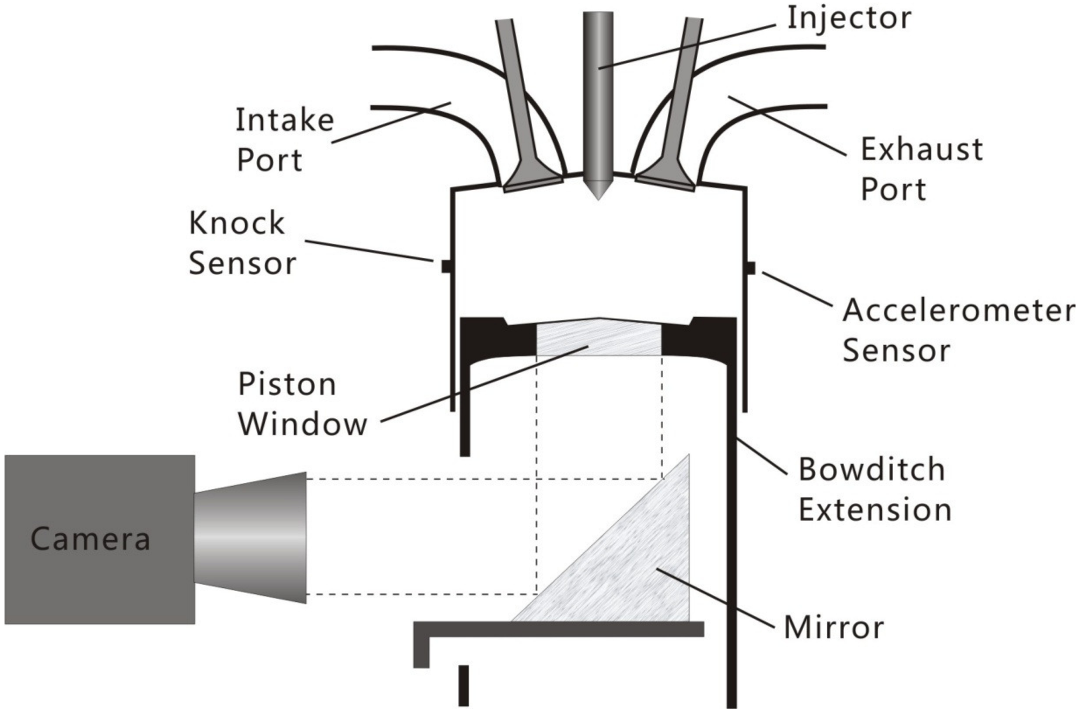

Figure 4-2. Optical test setup diagram

The diesel combustion usually consists of a cold flame phase and a blue flame phase, as well as an explosion flame phase [106], [107]. However, it is difficult to distinguish between the blue flame phase and the explosion flame phase, because there exists no exact-single point of the SOC [106]-[108]. Reference [108] used the infrared and visible imaging techniques simultaneously to study the combustion process from fuel spray to the end of the combustion. In this research, high speed combustion images were obtained through optical engine tests and were used to correlate the knock signal with the combustion phase. The high-speed camera used in this research was a Photron Fastcam APX RS. A shutter speed of 98 μs was used at a frame rate of 10,000 fps with a 512×512 pixel resolution. The frames were synchronized with the data collected by the CAS system by a TTL trigger pulse. Figure 4-2 shows the diagram of the high speed imaging test.

4.3 High Speed Combustion Imaging Tests

As mentioned above, the high speed combustion imaging tests were conducted to investigate relationship between the knock sensor signal and the combustion phase. The combustion phase is represented by MFB in this study. The MFB at the *k*-th interval is calculated as follows [109], [110],

$$MFB_k = \frac{\sum_0^k \Delta P_c}{\sum_0^N \Delta P_c}, \tag{4.2}$$

where ΔP_c represents the pressure rise due to the combustion, and it is calculated by

$$\Delta P_c = \Delta P - \Delta P_v, \tag{4.3}$$

where ΔP is the in-cylinder pressure change, and ΔP_v represents the pressure rise due to the combustion chamber volume change, it is calculated by

$$\Delta P_v = P_k - P_{k-1} = P_{k-1}\left[\left(\frac{V_{k-1}}{V_k}\right)^n - 1\right], \tag{4.4}$$

where P_k is the in-cylinder pressure at the *k*-th step.

It was observed that the knock sensor mounted on the cylinder wall provided a similar level of signal-to-noise (S/N) ratio to that of the accelerometer; whereas the S/N ratio of the knock sensor installed on the cylinder head was very low. The knock sensor mounted on the cylinder wall was used in the rest of the study, and it was filtered by a bandpass filter with cutoff frequencies of 3 kHz and 18 kHz, respectively.

Figure 3 shows the combustion images synchronized with the in-cylinder pressure (*InCylPre*), MFB, and the knock signal. In this combustion case, a 0.5ms fuel pulse was delivered at 12 degrees before top dead center (BTDC). The first visible flame (a tiny orange flame with certain blue flame) was observed around 182nd crank angle degree. It can be seen that this SOC was captured by the knock sensor. The significant flame was developed around the MFB10 location. However, the knock signal did not show high S/N ratio until 191st crank angle degree, where the combustion phase was very close to the point of MFB75. And it can be observed that the majority of the knock signal occurs between MFB75 and MFB90 locations.

A series of validation tests demonstrate similar correlations between the knock sensor signal and the combustion phase as shown in Figure 4-3. Therefore, detection of the MFB75 location using knock sensor signal was proposed in this study.

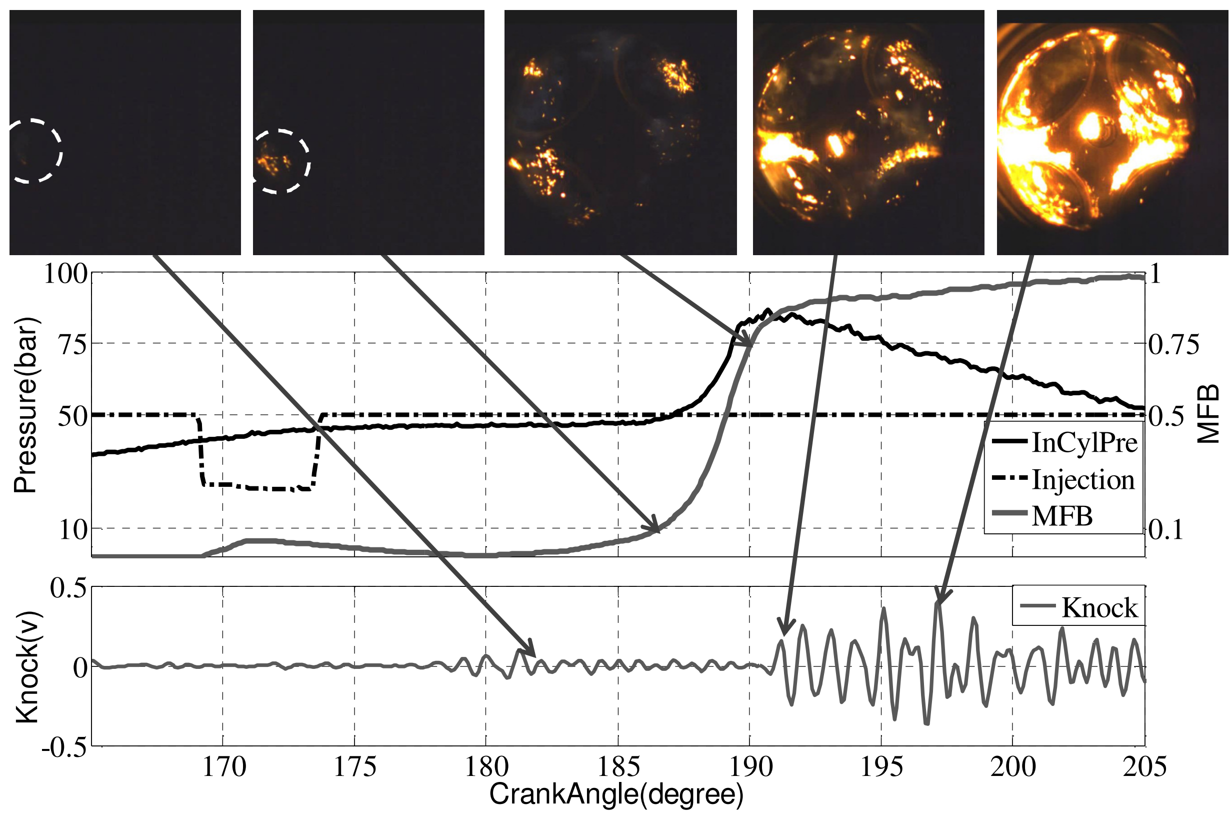

Figure 4-3. high speed images with in-cylinder pressure and knock signals

4.4 MFB75 Detection Method

Figure 4-4 shows a combustion event with relatively high knock intensity, which is evaluated based upon the signal *KnockInt* defined by,

$$KnockInt = \int_{TDC}^{TDC+20} |Knock(\tau)| d\tau \tag{4.5}$$

where τ represents the crank angle; *Knock* is the filtered knock sensor signal; and *KnockInt* represents the knock integration over 20 crank angle degree window starting from TDC. The signal *KnockIntCA*(i) is the integration of the knock signal over one crank degree starting at the i-th crank angle. It is defined by

$$KnockIntCA(i) = \int_{i}^{i+1} |Knock(\tau)| d\tau \tag{4.6}$$

Note that *KnockIntCA* represents the difference of the *KnockInt* over one crank degree.

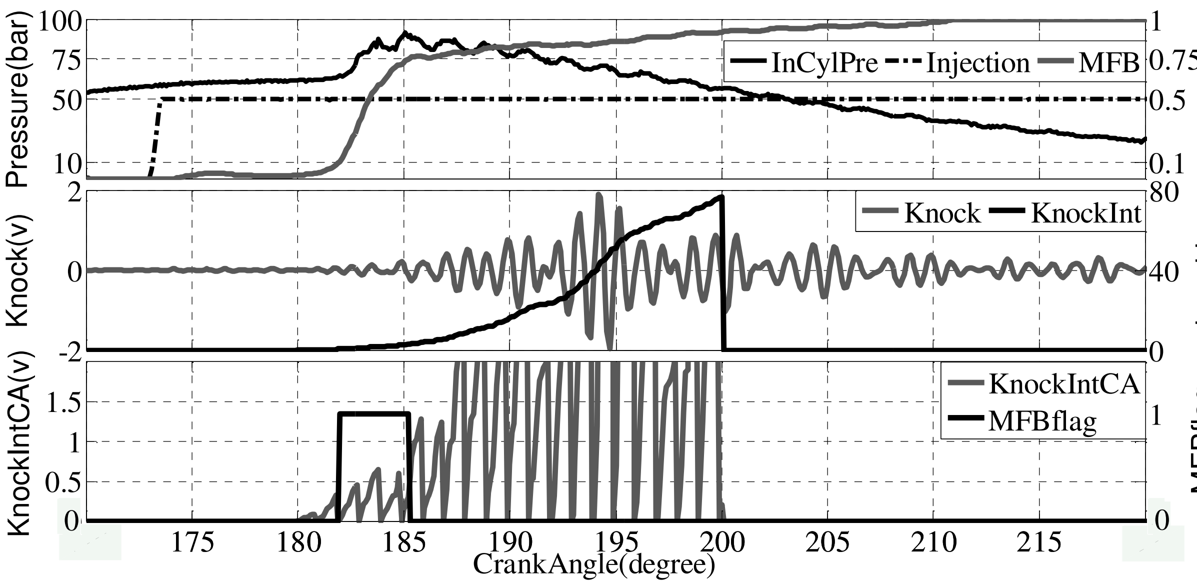

Figure 4-4. MFB75 detection with intense knock

In Figure 4-4, the rising edge of the signal *MFBflag* denotes the location of MFB10, and the falling edge of *MFBflag* denotes the MFB75 location. It can be seen that the MFB75 location is very close to the *KnockIntCA* peak, which is the first *KnockIntCA* peak greater than one. In addition, the following *KnockIntCA* peaks are all greater than one.

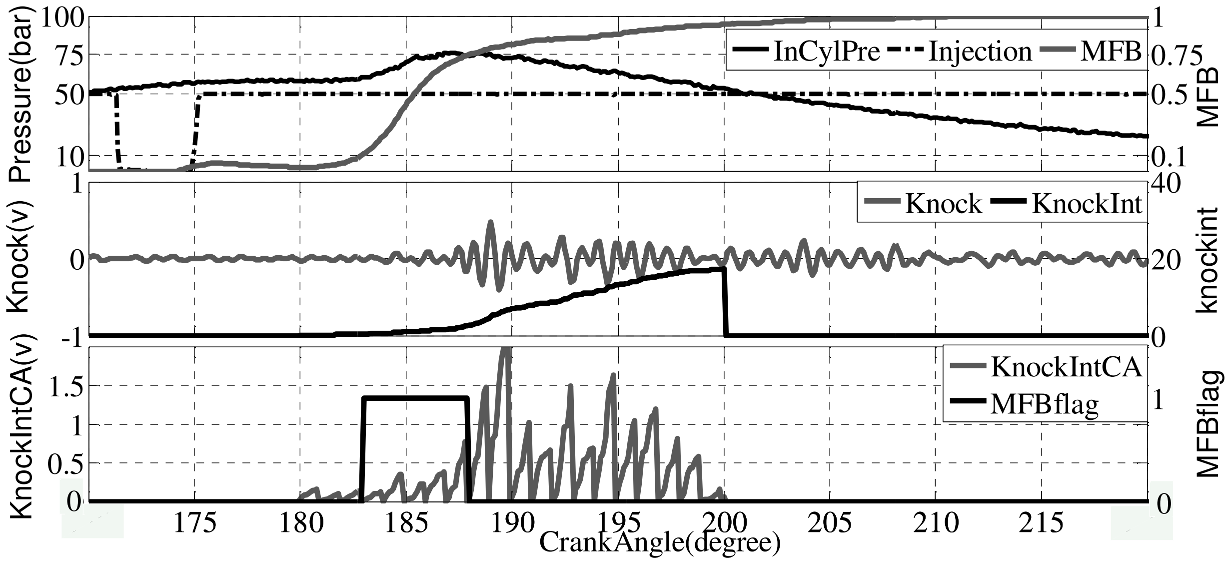

Figure 4-5. MFB75 detection with weak knock

The knock integration shown in Figure 4-4 reaches 80. A similar investigation was conducted for the combustions with relatively weak knock at light load, whose *KnockInt* is less than 20 as shown in Figure 4-5. However, the *KnockIntCA* peak corresponding to the point of MFB75 has the similar characteristics to the case shown in Figure 4-4. In this case, the first *KnockIntCA* peak is around 0.75.

Based upon the above observations, it is proposed to use the following criteria for detecting MFB75 location based upon the knock signal. The MFB75 location can be determined at *i*-th crank angle if

$$KnockIntCA(i-1) \leq KnockIntCA\_Thrsh, \tag{4.7}$$

and

$$\begin{aligned} &KnockIntCA(j) \geq KnockIntCA\_Thresh, \\ &with \quad j = i \cdots i+2 \end{aligned} \tag{4.8}$$

and

$$\frac{KnockIntCA(i)}{\frac{1}{i}\sum_{j=1}^{i} KnockIntCA(j)} \geq \alpha \tag{4.9}$$

where *KnockIntCA_Thresh* and α are two calibration parameters. Figure 4-6 shows the flow chart of the proposed MFB75 estimation algorithm. The physical interpretation of the detection logic is to correlate the sharp increase of *KnockIntCA* to locate the MFB75.

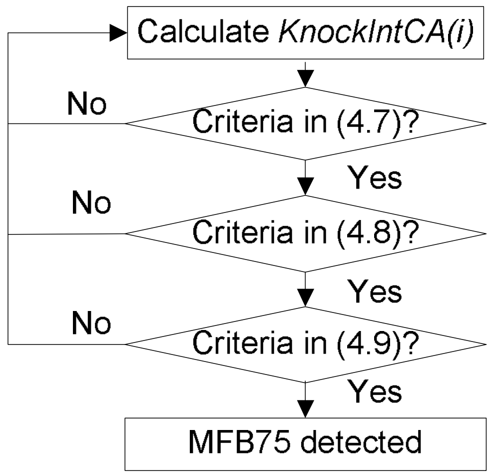

Figure 4-6. MFB75 estimation algorithm working flow chart

Table 4-2: Statistical analysis of the estimated MFB75 location

Fuel	Pilot Injection (degree/ms)	Main Injection (degree/ms)	Mean of MFB75 (degree)	Mean of Detected MFB75 (degree)	MAD	Knock Integration	Engine speed (rpm)
B0	0/0	10/0.5	10.8	10.6	2	20.3	1500
	0/0	13/0.5	9.9	10.8	1.3	18.4	1500
	24/0.35	4/0.5	12.4	11.7	0.9	24.7	1500
	24/0.35	4/0.5	10.5	11.5	1.2	25.8	1200
B50	0/0	10/0.5	8	8.6	0.8	50.7	1500
	0/0	13/0.5	6.7	6.4	0.5	51	1500
	24/0.25	4/0.5	12.5	13.1	1	20.8	1500
	24/0.35	4/0.5	10.3	10.3	0.5	42	1200
B100	0/0	10/0.5	7.1	6.4	1.3	46.5	1500
	0/0	13/0.5	5.3	5.1	0.5	57.7	1500
	24/0.35	4/0.5	11.8	11.1	1.4	27.1	1500
	24/0.25	4/0.5	11.7	13	1.4	19.1	1500
	24/0.25	4/0.45	9.6	10.8	1.3	25.9	1200

Based upon the above detection strategy, statistical analysis was conducted. In this analysis, engine tests with three different fuels, B0, B50, and B100, were conducted at two engine speeds, 1200rpm and 1500 rpm. Several groups of injection parameters were tested in order to study the proposed approach over different knock intensity. For each test, the mean value of the MFB75 location (crank angle) and the mean absolute deviation (MAD), both measured and estimated, were calculated over 40 combustion cycles. In this study, *KnockIntCA_Thresh* was set at 0.7, and α was fixed at 1.5. Table 4-2 provides the analysis results. It can be seen that the estimated meanvalues of MFB75 are very close to the actual ones, and based upon the MAD, it can be concluded that the estimation has good cycle-to-cycle accuracy with largest estimation error equal to 2 degrees. Furthermore, it is observed that the higher the knock intensity, the better the estimation accuracy.

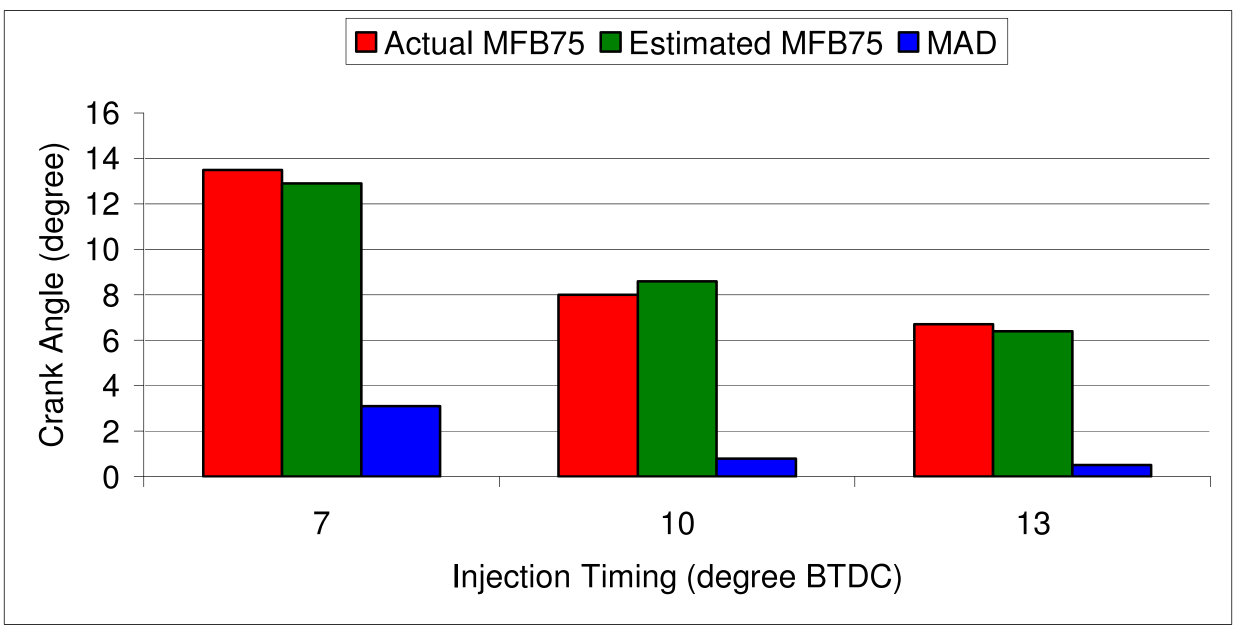

Figure 4-7. MFB75 estimation under same fuel blend

Figure 4-7 shows a comparison result of B50 with three different fuel injection timings, 7, 10, and 13 degrees BTDC with the same fuel injection pulses. It can be found that the MFB75 estimation associated with the 13 degree BTDC injection provided the most accurate result. This is because the injection at 13 degree BTDC led to the largest knock intensity, while the injection at 7 degree BTDC led to the least. In addition, the analysis results also show that when the knock intensity is high, the deviation of the estimated value leans to negative, and vice versa. Therefore, the absolute estimation error can be further reduced by using different KnockIntCA_Thresh and α under different knock intensities, which, in general, is function of engine speed and load condition. The other approach is to generate an offset map as a function of engine speed and load. It is believed through data analysis that the estimation error can be reduced to within one degree.

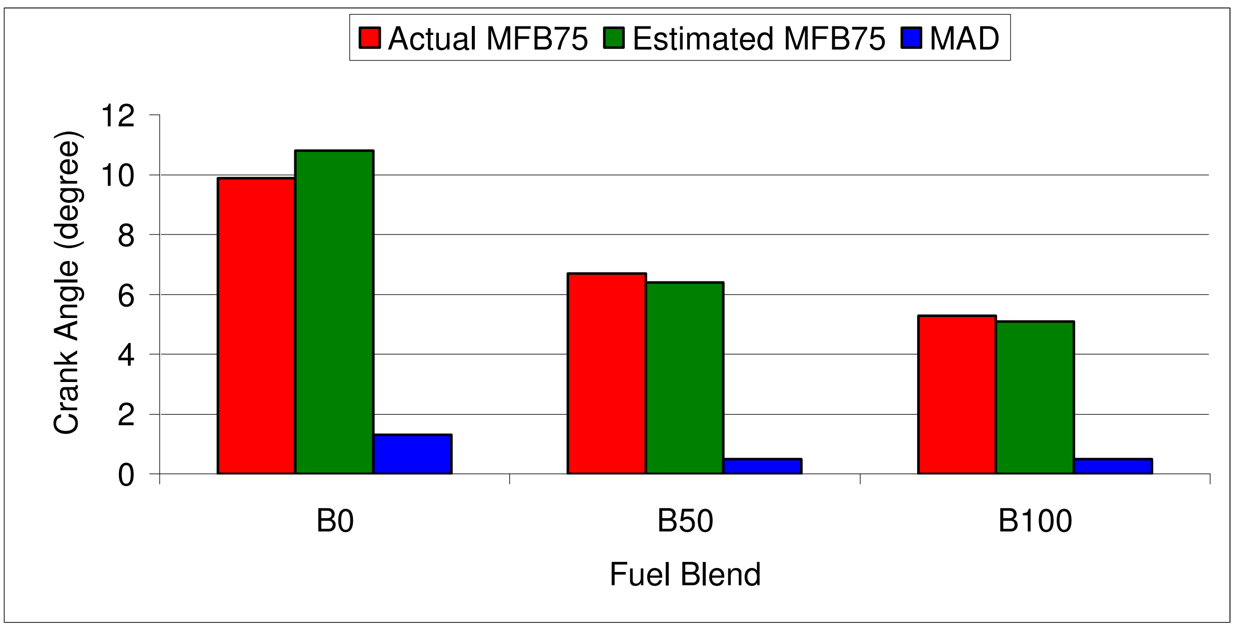

Figure 4-8. MFB75 estimation comparison under same injection conditions

In addition, it was also noticed that for the same fuel injection conditions, the MFB75 location of B100 is the smallest, whereas the one of B0 is the largest as shown in Figure 4-8. This is not only because B100 starts combustion earlier, but it also burns much faster. Therefore, it is possible that the estimated MFB75 can be used to detect the biodiesel fuel content.

4.5 Biodiesel Content Estimation

The interest in detecting the biodiesel content is due to the fact that difference in fuel content leads to different SOC, burn rate, burn duration, etc. This research studies the feasibility of using the knock integration information to estimate the fuel content. Three types of fuel, B0, B50, and B100, were studied in this research.

Figure 4-9 shows the knock integration for the engine combustions of three different fuels under the same engine operational condition. The same fuel pulse, 0.5ms, was used with two different injection timings, 13 and 7 degrees BTDC, which lead to different knock intensities. It can be seen that the differences between three different fuels are quite distinct. B100 has the highest knock intensity in both cases, whereas B0 has the lowest. This is because B100 has highest CN, so that the combustion occurs earlier and burns faster than these of B0 and B50 as shown in Figure 4-10.

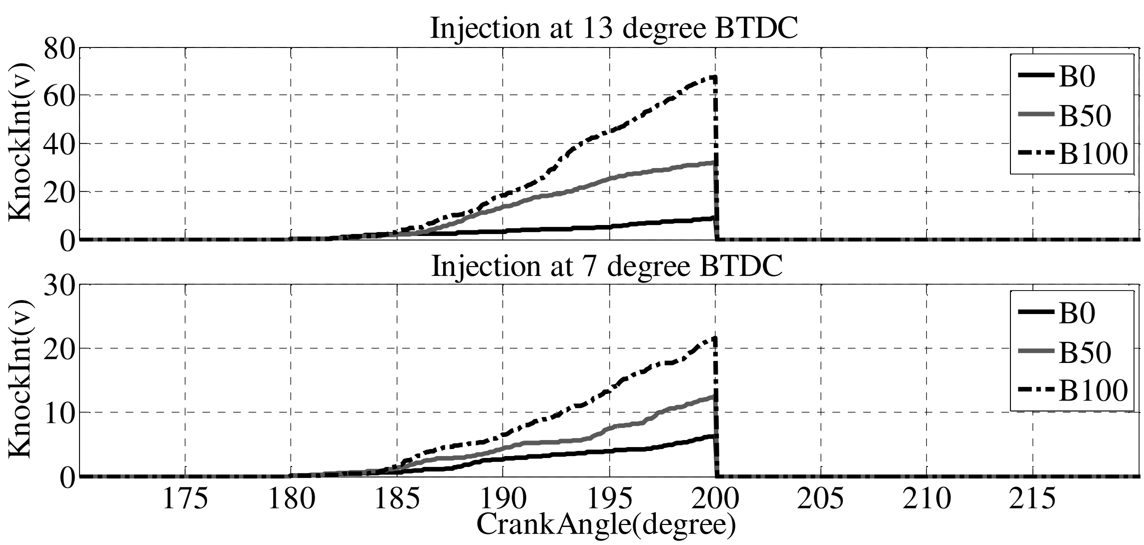

Figure 4-9. Knock integration without pilot injection

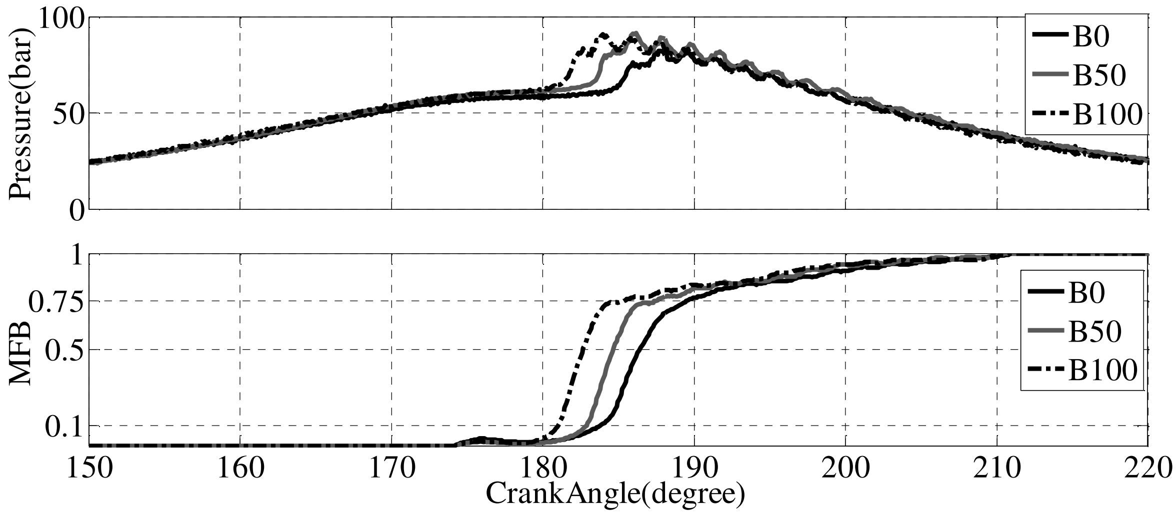

Figure 4-10. In-cylinder pressure and MFB compare

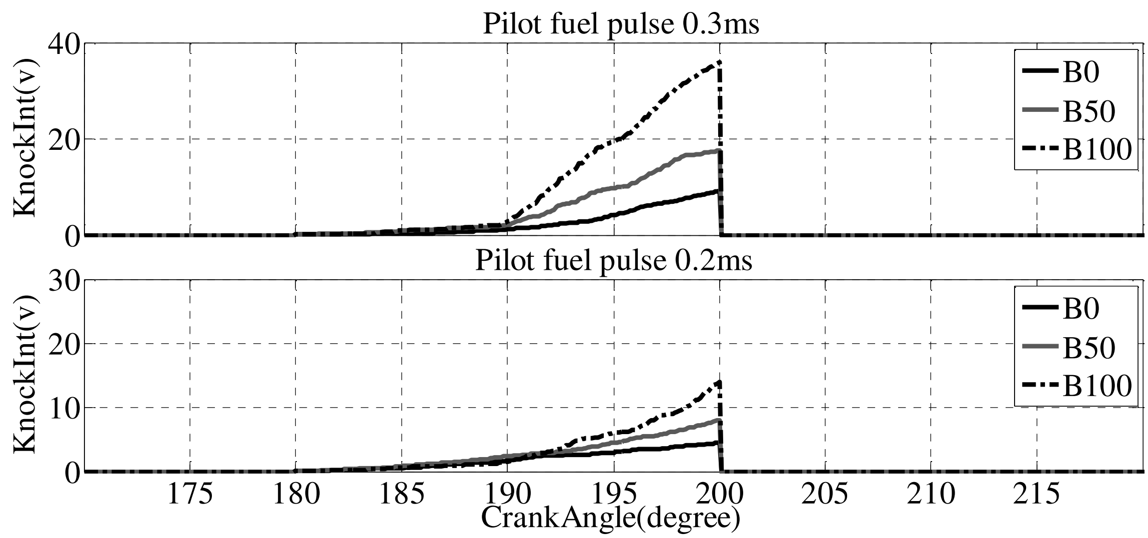

Figure 4-11. Knock integration with pilot injection

Since pilot injection reduces the knock intensity significantly, a study with pilot injection was also conducted in this research. The main injection is a 0.45ms fuel pulse delivered at 4 degrees BTDC. Two different pilot fuel pulses, 0.2ms and 0.3ms, were tested with the injection timing fixed at 24 degree BTDC. Note that, the engine load was close to the data shown in Figure 4-9. With pilot injection, the magnitude of the knock integration reduced dramatically as shown in Figure 4-11. However, the differences in the knock intensity of the three fuels were still as distinct as without the pilot injection.

Since knock is affected by many factors, such as intake air temperature, intake air pressure, injection timing and so on, a statistical analysis was conducted by evaluating the mean value of the knock integration over 40 consecutive combustion cycles, and the results are presented in Table 4-3. Figure 4-12 shows the corresponding statistical analysis for easy comparison.

Table 4-3: Statistical analysis of knock integration

Engine speed (rpm)	Pilot Injection	Main Injection	Knock Integration		
	Timing /Pulse (degree /ms)	Timing /Pulse (degree /ms)	B0	B50	B100
1200	24/0.2	4/0.5	4.4	10.8	12.1
	24/0.3	4/0.5	4.4	13	14.8
	0/0	10/0.5	4.4	12.6	13.4
1500	24/0.2	4/0.5	6	18.5	20.2
	24/0.3	4/0.5	6.3	19.9	20.9
	0/0	10/0.5	16.9	48	48.2
	0/0	13/0.5	18.1	48.6	57.4

The results show a clear difference between B0 and B50, whereas the difference between B50 and B100 is not that obvious except for case #4 at 1500 rpm. Further investigation of the fuel blend between B0 and B50 is necessary. However, the results in Figure 4-8 show that both the actual and the estimated MFB75 location have clear differences among three fuels. Therefore, it is possible to precisely estimate the fuel blend by using both of the above mentioned information, the estimated MFB75 location and the knock integration. In a summary, it is feasible to use the knock sensor signal for estimating the fuel content.

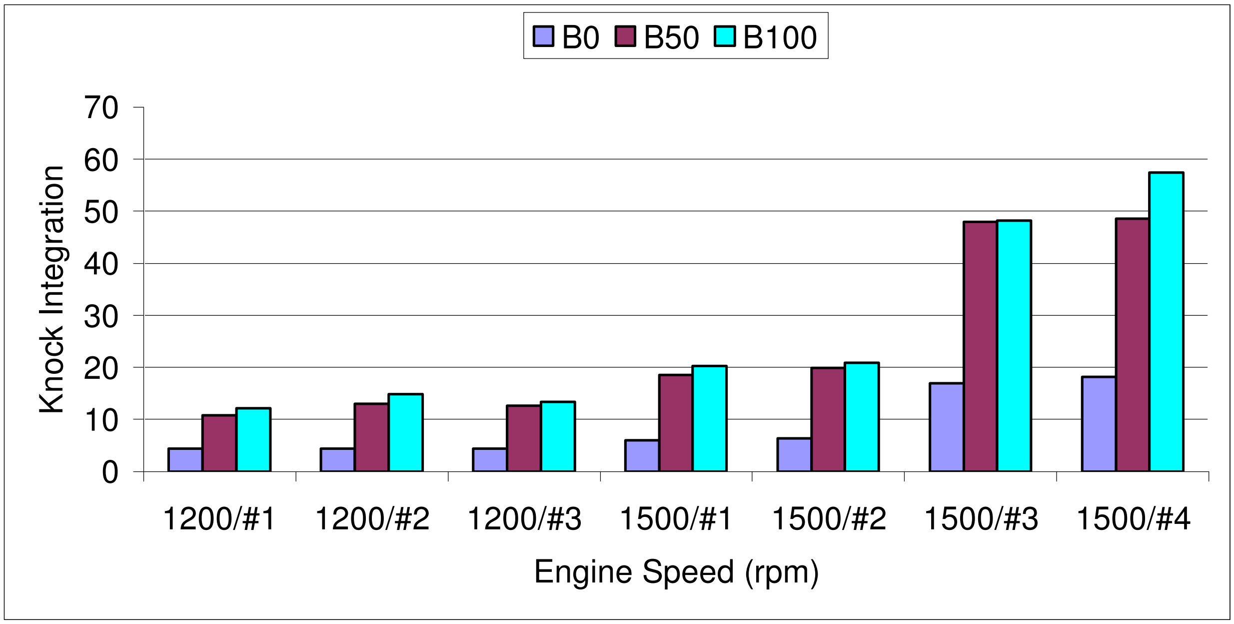

Figure 4-12. Knock integration comparison for three fuel blends

4.6 Conclusions

This study proposes a method to detect the 75% mass fraction burned (MFB75) location using the traditional knock sensor signal. This study was motivated by using a low cost sensor to detect or estimate the combustion phase. The experimental data shows that the knock signal demonstrates certain correlation to MFB location. An estimation algorithm based upon the piecewise knock integral was proposed and validated using the experimental data. It shows that the MFB75 estimation error, using knock sensor signal, is within 2 crank degrees. With the help of calibrating the detecting thresholds as function of engine speed and load, it can be reduced down to one degree. In addition, investigation of using the knock sensor signal to estimate the biodiesel blend was conducted. The results show the feasibility of estimating the biofuel content using the knock sensor signal.

CHAPTER 5 CONCLUSIONS AND FUTURE WORK

5.1 Conclusions

Different blend of biofuel has different start of combustion (SOC), burn rates, and other properties. It is important to detect the fuel blend and optimize the combustion for biofuel engines. This dissertation investigates the control applications to biofuel engines through several different aspects, such as biofuel content estimation, biofuel engine air-to-fuel ratio control, as well as the biofuel engine combustion phase detection.

The first part of this dissertation studied the feasibility of using ionic polymer material composite (IPMC) beams to detect the fuel flow properties (such as fluid density and drag coefficient,) for fuel content estimation. In this study, an IPMC beam flow sensor was developed and tested in a series of pulsating flow experiments, which were used to simulate the fuel injections. The experimental results show that the IPMC beam flow sensor not only is able to detect the start and end of pulsating flow, but also shows distinct responses under different fluid media. This is very important for biofuel engines where the characteristics of the fuel blend need to be identified in real time. A dynamic, multi-segment model for IPMC beam under fluid flow was developed, which was then used to identify the fluid parameters through least-squares minimization. The estimation scheme was evaluated with two different pulsating flows, water and n-Heptane, and the estimated fluid parameters showed good agreement with the true parameters for those media.

The second study used an LQ optimal tracking scheme to regulate the air-to-fuel ratio (AFR) of a biofuel lean burn engine during the lean NOx Trap (LNT) regeneration period based upon the adaptively estimated biofuel content by using the oxygen sensor signal. The robust stability of the closed loop system with adaptive estimation was analyzed based upon the framework of the linear parameter varying (LPV) systems, where both the estimated fuel gain and the engine speed were considered as time varying parameters. Several adaptive control schemes were evaluated through both simulation and dynamometer experiments. The results show that the proposed LQ tracking control with the gain-scheduling adaptive estimation provided the best fuel estimation performance (minimal AFR error) and demonstrated the ability to regulate the AFR during the LNT regeneration for a flex fuel lean burn engine.

The third part of this dissertation studied the use of a low cost knock sensor to detect the 75% mass fraction burned (MFB75) location, and also to estimate the biofuel content. A series of experiments were performed, and the experimental data shows that the knock signal demonstrates certain correlation to the MFB75 location. In this study, an estimation algorithm based upon the piecewise knock integral was proposed and validated using the experimental data. It was found that the MFB75 estimation error is within 2 crank degrees. In addition, the analysis results also show that the deviation of the estimated MFB75 location is highly correlated with the knock intensity. This study also conducted an investigation of the use of the knock sensor signal to estimate the biodiesel blend. The results show that both the knock intensity and the detected MFB75 location hold strong promising feasibility for the biofuel content estimation.

5.2 Recommendations for Future Work

The work presented in this dissertation was at the early stage. There is still a lot of work to be done to continue improving the ideas or methodologies presented in this dissertation, especially for the IPMC beam flow sensor. In order to implement the IPMC beam flow sensor onto automotive engines, several issues must be addressed. For example, the IPMC sensor should be minimized , so that it can be installed into the fuel injector; the sensor signal conditioning method (both hardware and software) should be improved to obtain higher signal to noise ratio (S/N); and a criterion for the sensor signal data selection used for estimation should be developed.

There is still room of improvement for the method of using the oxygen sensor for the LQ optimal tracking control to regulate the air-to-fuel ratio (AFR) of a biofuel lean burn engine during the lean NOx Trap (LNT) regeneration period based upon the adaptively estimated biofuel content. For example, for practical applications, engine torque needs to be regulated to a target value based upon the estimated fuel content during the LNT regeneration.

In terms of using the traditional knock sensor to estimate the MFB75 location, it is believed that the estimation accuracy can be significantly improved with the help of calibrating the detecting thresholds as function of engine speed and load. In addition, the development of an accurate biofuel content estimation algorithm using both estimated MFB75 and knock intensity for biofuel blends is very promising.

BIBOLIOGRAPHY

BIBLIOGRAPHY

[1] P. Jean-Baptiste, and R. Ducrous, "Energy policy and climate change," *Energy policy*, vol. 31, pp. 155-166, 2003.

[2] A. Demirbas, "Progress and recent trends in biofuels," *Progress in Energy and combustion science*, vol. 33, pp. 1-18, 2007.

[3] A. Demirbas, "Importance of biodiesel as transportation fuel," Energy policy, vol. 35, no. 9, pp. 4661-4670, 2007.

[4] D. Snyder, G. Adi, M. Bunce, C. Satkoski, and G. Shaver, "Steady-state biodiesel blend estimation via a wideband oxygen sensor," *The ASME Journal of Dynamic Systems, Measurement and Control*, vol. 131, no. 4, July, 2009, pp. 988-993.

[5] D. Snyder, G. Adi, M. Bunce, C. Hall and G. Shaver, "Dynamic exhaust oxygen based biodiesel blend estimation with an extended Kalman filter," In *proceedings of 2010 American Control Conference*, Baltimore, MD, June, 2010.

[6] K. Ahn, A. Stefanopoulou, and M. Jankovic, "Estimation of ethanol content in flex-fuel vehicles using an exhaust gas oxygen sensor: model, tuning and sensitivity," In *Proceedings of Dynamic Systems and Control Conference (DSCC08)*, Ann Arbor, MI, 2008.

[7] K. Ahn, A. Stefanopoulous, L. Jiang, and H. Yilmaz, "Ethanol content estimation in flex fuel direct injection engines using in-cylinder pressure measurements," *SAE 2010-01-0166*, 2010.

[8] C. Daniels, G. Zhu, W. Mammen, and M. Zhang, "Virtual flex fuel sensor for spark ignition engines using ionization signal," *U.S. Patent 7921704*, April 12, 2011.

[9] Y. Bar-Cohen (ed.), *Electroactive Polymer Actuators as Artificial Muscles: Reality, Potential and Challenges*. Bellingham, WA: SPIE, 2001.

[10] M. Shahinpoor, and K. Kim, "Ionic polymer-metal composites: I. Fundamentals," *Smart Materials and Structures*, vol. 10, pp. 819–833, 2001.

[11] J. Parks, S. Huff, J. Pihi, J. Choi, and B. West, "Nitrogen selectivity in Lean NOx Trap catalysis with diesel engine in-cylinder regeneration," *SAE 2005-01-3876*, 2005.

[12] Y. Kim, J. Sun, and L. Wang, "Optimization of purge air-to-fuel ratio profiles for enhanced Lean NOx Trap control," *Proceeding of the 2004 American Control Conference*, Boston, MA, 2004, pp. 132-137.

[13] D. Assanis, F. Filipi, S. Fiveland, M. Syrimis, "A predictive ignition delay correlation under steady-state and transient operation of a direct-injection diesel engine," 1999 ASME Fall Technical Conf., paper no. 99-ICE-231, ICE vol. 32-2, 1999.

[14] C. Lee, S. Park, and S. Kwon, "An experimental study on the atomization and combustion characteristics of biodiesel-blend fuels," *Energy & fuels*, vol.19, pp. 2201-2208, 2005.

[15] J. Bittle, B. Knight, and T. Jacobs, "Interesting behavior of biodiesel ignition delay and combustion duration," Energy & fuels, vol. 24, pp. 4166-4177, 2010.

[16] D. Schiefer, R. Maennel, and W. Nardoni, "Adavantages of diesel engine control using in-cylinder pressure information for closed loop control," *SAE 2003-01-0364*, 2003

[17] M. Glavmo, P. Spadafora, and R. Bosch, "Closed loop start of combustion control utilizing ionization sensing in a diesel engine," SAE 1999-01-0549, 1999.

[18] M. Jargenstedt, "Detecting start of combustion using knock sensor signals," Master's thesis, Linkoping Univsersity, Department of Electrical Engineering, Vehicle Systems 2000.

[19] S. Prosser, "Automotive sensors: past, present and future," *Journal of Physics: Conference Series*, vol. 76, pp. 012001:1-6, 2007.

[20] G. Zhu, I. Haskara, and J. R. Winkelman, "Stochastic limit control and its application to knock limit control using ionization feedback," *Proceedings of SAE 2005 World Congress,* 2005, Technical Paper No. 2005-01-0018.

[21] A. Gandhi, M. Meinhart, and S. Ortiz, "A summary of flow metering options for injector characterization," *Proceedings of SAE 2009 World Congress,* 2009, Technical Paper No. 2009-01-0747.

[22] S. Pace and G. Zhu, "Air-to-fuel ratio and dual-fuel ratio control of an internal combustion engine," *Proceedings of SAE 2009 World Congress,* 2009, Technical Paper No. 2009-01-2794.

[23] Y. Yang, J. Chen, J. Engel, S. Pandya, N. Chen, C. Tucker, S. Coombs, D. L. Jones, and C. Liu, "Distant touch hydrodynamic imaging with an artificial lateral line," *Proceedings of the National Academy of Sciences*, vol. 103, no. 50, pp. 18891, 2010.

[24] Y. Yang, N. Nguyen, N. Chen, M. Lockwood, C. Tucker, H. Hu, H. Bleckmann, C. Liu, and D. L. Jones, "Artificial lateral line with biomimetic neuromasts to emulate fish sensing," *Bioinspiration & Biomimetics*, vol. 5, pp. 016001, 2010.

[25] A. Dagamseh, T. Lammerink, M. Kolster, C. Bruinink, R. Wiegerink, and G. Krijnen, "Dipole-source localization using biomimetic flow-sensor arrays positioned as lateral-line system," *Sensors and Actuators A*, vol. 162, no. 2, pp. 355-360, 2010.

[26] K. Leang, Y, Shan, S. Song, and K. Kim, "Integrated sensing for IPMC actuators using strain gages for underwater applications," *IEEE/ASME Transactions on Mechatronics*, 2011 (to appear). DOI: 10.1109/TMECH.2011.2105885.

[27] A. Fleming and K. Leang, "Integrated strain and force feedback for high-performance control of piezoelectric actuators," *Sensors and Actuators A*, vol. 161, no. 1-2, pp. 256-265, 2010.

[28] B. Akle, M. Bennett, and D. Leo, "High-strain ionomeric-ionic liquid electroactive actuators," *Sensors and Actuators A*, vol. 126, pp. 173–181, 2006.

[29] K. Kim and M. Shahinpoor, "Ionic polymer–metal composites. Part II. Manufacturing techniques," *Smart Materials and Structures*, vol. 12, pp. 65–79, 2003.

[30] Z. Chen and X. Tan, "Monolithic fabrication of ionic polymer-metal composite actuators capable of complex deformation," *Sensors and Actuators A: Physical*, vol. 157, pp. 246-257, 2010.

[31] C. Bonomo, L. Fortuna, P. Giannone, S. Graziani, and S. Strazzeri, "A model for ionic polymer metal composites as sensors," *Smart Mater. Struct.*, vol. 15, 2006.

[32] Z. Chen, X. Tan, A. Will, and C. Ziel, "A dynamic model for ionic polymer-metal composite sensors," *Smart Materials and Structures*, vol. 16, pp. 1477-1488, 2007.

[33] Z. Chen and X. Tan, "A control-oriented and physics-based model for ionic polymer-metal composite actuators," *IEEE/ASME Transactions on Mechatronics*, vol. 13, no. 5, pp. 519–529, 2008.

[34] Z. Chen, D. Hedgepeth, and X. Tan, "A nonlinear, control-oriented model for ionic polymer-metal composite actuators," *Smart Materials and Structures*, vol. 18, pp. 055008:1-9, 2009.

[35] P. de Gennes, K. Okumura, M. Shahinpoor, and K. Kim, "Mechanoelectric effects in ionic gels," *Europhys. Lett.*, vol. 50, no. 4, pp. 513–518, 2000.

[36] M. Porfiri, "Charge dynamics in ionic polymer metal composites," *J. Appl. Phys.*, vol. 104, no. 10, pp. 104915:1-10, 2008.

[37] A. Abdulsadda and X. Tan, "Underwater source localization using an IPMC-based artificial lateral line," *Proceedings of the 2011 IEEE International Conference on Robotics and Automation*, 2011, pp. 2719-2724.

[38] L. Ferrara, M. Shahinpoor, K. Kim, H. Schreyer, A. Keshavarzi, E. Benzel, and J. Lantz, "Use of ionic polymer-metal composites (IPMCs) as a pressure transducer in the human spine," in *Smart Structures and Materials 1999: Electroactive Polymer Actuators and Devices*; *Proc. SPIE*, vol. 3669, 1999, pp. 394-401.

[39] A. Keshavarzi, M. Shahinpoor, K. Kim and J. Lantz, "Blood pressure, pulse rate, and rhythm measurement using ionic polymer-metal composite sensors," in *Smart Structures and Materials 1999: Electroactive Polymer Actuators and Devices*; *Proc. SPIE*, vol. 3669, 1999, pp.369-376.

[40] T. Ganley, D.L.S. Hung, G. Zhu, and X. Tan, "Modeling and inverse compensation of temperature-dependent ionic polymer-metal composite sensor dynamics," *IEEE/ASME Transactions on Mechatronics*, vol. 16, no. 1, pp. 80-89, 2011.

[41] J. Wang, C. Xu, M. Taya and Y. Kuga, "Bio-inspired tactile sensor with arrayed structures based on electroactive polymers," in *Electroactive Polymer Actuators and Devices (EAPAD) 2008, Proc. SPIE*, Y. Bar-Cohen, Ed., vol. 6927, 2008, pp. 69271B:1-8.

[42] P. Brunetto, L. Fortuna, P. Giannone, S. Graziani, and F. Pagano, "A small scale viscometer based on an IPMC actuator and an IPMC sensor," *Proceedings of 2010 IEEE Instrumentation and Measurement Technology Conference*, 2010, pp. 585-589.

[43] S. D. Peterson, M. Porfiri, and A. Rovardi, "A particle image velocimetry study of vibrating ionic polymer metal composites in aqueous environments," *IEEE/ASME Transactions on Mechatronics*, vol. 14, no. 4, pp. 474-483, 2009.

[44] C. Prince, W.Lin, J. Lin, S. D. Peterson, and M. Porfiri, "Temporally-resolved hydrodynamics in the vicinity of a vibrating ionic polymer-metal composite," *Journal of Applied Physics*, vol. 107, pp.094908, 2010.

[45] M. Aureli, V. Kopman, and M. Porfiri, "Free-locomotion of underwater vehicles actuated by ionic polymer metal composites," *IEEE/ASME Transactions on Mechatronics*, vol. 15, no. 4, pp. 603-614, 2010.

[46] Z. Chen, S. Shatara, and X. Tan, "Modeling of biomimetic robotic fish propelled by an ionic polymer-metal composite caudal fin," *IEEE/ASME Transactions on Mechatronics*, vol. 15, no. 3, pp. 448-459, 2010.

[47] W. Yim, J. Lee, and K. J. Kim, "An artificial muscle actuator for biomimetic underwater propulsors," *Bioinspiration Biomimetics*, vol. 2, pp. S31–S41, 2007.

[48] P. Brunetto, L. Fortuna, S. Graziani, and S. Strazzeri, "A model of ionic polymer–metal composite actuators in underwater operations," *Smart Mater. Struct.*, vol. 17, no. 2, pp. 025 029:1-12, 2008.

[49] K. Abdelnour, E. Mancia, S. Peterson, and M. Porfiri, "Hydrodynamics of underwater propulsors based on ionic polymer metal composites: A numerical study," *Smart Mater. Struct.*, vol. 18, no. 8, pp. 085 006:1–11, 2009.

[50] A. J. MacDaid, K. C. Aw, E. Haemmerle, and S. Q. Xie, "Control of IPMC actuators for microfluidics with adaptive "online" iterative feedback tuning," *IEEE/ASME Transactions on Mechatronics, in press,* 2011 (*DOI: 10.1109/TMECH.2011.2135373*).

[51] K. K. Leang, Y. Shan, S. Song, and K. J. Kim, "Integrated sensing for IPMC actuators using strain gages for underwater application," *IEEE/ASME Transactions on Mechatronics, in press,* 2011 (*DOI: 10.1109/TMECH.2011.2105885*).

[52] M. Aureli, C. Prince, M. Porfiri, and S. D. Peterson, “Energy harvesting from base excitation of ionic polymer metal composites in fluid environments,” *Smart Materials and Structures*, vol. 19, pp. 015003, 2010.

[53] A. Giacomello and M. Porfiri, “Underwater energy harvesting from a heavy flag hosting ionic polymer metal composites,” *Journal of Applied Physics*, vol. 109, pp. 084903, 2011.

[54] J. Chung and H. Yoo, “Dynamic analysis of a rotating cantilever beam by using the finite element method,” *Journal of Sound and Vibration*, vol. 249, no. 1, 147-164, 2002.

[55] N. Wereley, G. Wang, and A. Chaudhuri, “Demonstration of uniform cantilevered beam bending vibration using a pair of piezoelectric actuators,” *Journal of Intelligent Material Systems and Structures*, vol. 22, no. 4, pp. 307-316, 2011.

[56] A. K. Banerjee and S. Nagarajan, “Efficient simulation of large overall motion of beams undergoing large deflection,” *Multibody System Dynamics,* vol. 1, pp. 113-126, 1997.

[57] S. J. Kim, I. T. Lee, and Y. H. Kim, “Performance enhancement of IPMC actuator by plasma surface treatment,” *Smart Materials and Structures*, vol. 16, no. 1, pp. N6–N11, 2007.

[58] W. Thomson and M. Dahleh, *Theory of Vibration with Applications*, 5th ed., Prentice Hall, pp. 163-187, 1998.

[59] P. Heyliger and J. Reddy, “A higher order beam finite element for bending and vibration problems,” *Journal of Sound and Vibration*, vol.126, no. 2, pp. 309-326, 1988.

[60] J. Sader, “Frequency response of cantilever beams immersed in viscous fluids with applications to the atomic force microscope,” *J. Appl. Phys.*, vol. 84, no. 1, pp. 64–76, 1998.

[61] Z. Chen, Y. Shen, N. Xi, and X. Tan, “Integrated sensing for ionic polymer-metal composite actuators using PVDF thin films,” *Smart Structures and Materials*, vol. 16, pp. S262-S271, 2007.

[62] M. Potter and D. Wiggert, *Mechanics of Fluid*, 2nd ed., Prentice Hall, pp. 339-343, 1997.

[63] J. W. L. Zhou, H.-Y. Chan, T. K.H. To, K. W. C. Lai, and W. J. Li, “Polymer MEMS actuators for underwater micromanipulation,” IEEE/ASME Transactions on Mechatronics, vol. 9, no. 2, pp. 334-342, 2004.

[64] G.-H. Feng and R.-H. Chen, “Improved cost-effective fabrication of arbitrarily shaped μIPMC transducers,” *J. Micromech. Microeng.*, vol. 18, pp. 015016, 2008.

[65] G. H. Keulegan and L. H. Carpenter, “Forces on cylinders and plates in an oscillating fluid,” *J. Res. Natl Bur. Stand.*, vol. 60, no. 5, pp. 423-440, 1958.

[66] R. A. Bidkar, M. Kimber, A. Raman, A. K. Bajaj, and S. V. Garimella, “Nonlinear aerodynamic damping of sharp-edged flexible beams oscillating at low Keulegan-Carpenter numbers,” *Journal of Fluid Mechanics*, vol. 634, pp. 269-289, 2009.

[67] J. Szybist, J. Song, M. Alam, and A. Boeham, “Biodiesel combustion, emission and emission control,” *Fuel Processing Technology,* vol. 88, 2007, pp. 676-691.

[68] J. McCrady, A. Hansen, and C. Lee, “Modeling biodiesel combustion using GT-Power,” *An ASABE Meeting Presentation*, Paper Number: 076095, June, 2007

[69] J. McCrady, A. Hansen, and C. Lee, “Combustion and emissions modeling of biodiesel using GT-Power,” *An ASABE Meeting Presentation*, Paper Number: 084045, June, 2008.

[70] D. Snyder, G. Adi, M. Bunce, and G. Shaver, “Fuel blend fraction estimation for fuel-flexible combustion control: uncertainty analysis,” *Journal of Control Engineering Practice*, vol. 18, April, 2010, pp. 418-432.

[71] X. Chen, G. Zhu, X. Yang, D. Hung, and X. Tan, “Model-based estimation of flow characteristics using an ionic polymer-metal composite beam,” *IEEE Trans. Mechatronics.*, submitted for publication (Accepted in 2012).

[72] J. Sun, Y. Kim, and L. Wang, “Aftertreatment control and adaptation for lean burn engine with HEGO sensors,” *International Journal of Adaptive Control and Signal Processing*, vol. 18, 2004, pp. 145-166.

[73] Y. Wang and I. Haskara, “Method and apparatus for controlling engine operation during regeneration of an exhaust aftertreatment system,” *U.S. Patent 0078167*, April 3, 2008.

[74] P. Witze, S. Huff, J. Storey, and B. West, “Time-resolved laser-induced incandescence measurements of particulate emissions during enrichment for diesel Lean NOx Trap regeneration,” *SAE 2005-01-0186*, 2005.

[75] V. Jones, B. Ault, G. Franklin, and J. Powell, “Identification and air-fuel ratio control of a spark ignition engine,” *IEEE Trans. Control Systems Technology*, Vol. 3, No. 1, March, 1995, pp. 14-21.

[76] F. Zhang, K. Grigoriadis, M. Franchek, and I. Makki, “Linear parameter-varying lean burn air-fuel ratio control for a spark ignition engine,” *Transactions of ASME*, Vol. 129, July, 2007, pp. 404-414.

[77] P. Loannou and B. Fidan, *Adaptive Control Tutorial*, SIAM, 2006, pp. 91-121.

[78] E. Mosca, *Optimal, Predictive, and Adaptive Control*, Prentice Hall, 1995, pp.127-231.

[79] B. Barmish, “Necessary and sufficient conditions for quadratic stabilizability of an uncertain system,” *Journal of Optimization Theory and Applications*, Vol. 46, No. 4, August, 1985, pp. 399-408.

[80] A. Ilchmann, D. Owens, and D. Pratzel-Wolters, “Sufficient conditions for stability of linear time-varying systems,” *Systems & Control Letters*, 1987, pp. 157-163.

[81] V. Montagner and P. Peres, “A new LMI condition for the robust stability of linear time-varying systems,” *Proceedings of the 42nd IEEE Conference on Decision and Control*, Maui, Hawaii, Dec. 2003.

[82] R. Oliveira and P. Peres, “Robust stability analysis and control design for time-varying discrete-time polytopic systems with bounded parameter variation,” In *proceedings of 2008 American Control Conference*, Seattle, WA, Jun. 2008.

[83] J. Caigny, J. Camino, R. Oliveira, P. Peres, and J. Swevers, “Gain-scheduled H_2 and H_∞ control of discrete-time polytopic time-varying systems,” *IET Control Theory Application*, Vol. 4, Iss. 3, 2010, pp. 362-380.

[84] K. S. Tyson, J. Bozell, R. Wallace, E. Petersen, and L. Moens, “Biomass oil analysis research needs and recommendations,” *NREL/TP-510-34796*, Golden, CO, National Renewable Energy Laboratory, Jun, 2004.

[85] J. Sheehan, V. Camobreco, J. Duffield, M. Graboski, and H. Shapouri, “An overview of biodiesel and petroleum diesel life cycles,” *NREL/TP-580-24772*, Golden, CO, National Renewable Energy Laboratory, May, 1998.

[86] United States Environmental Protection Agency, “A comprehensive analysis of biodiesel impacts on exhaust emissions,” *EPA420-P-02-001*, draft technical report, 2002.

[87] R. L. McCormich, J. D. Ross, and M. S. Graboski, “Effect of several oxygenates on regulated emissions from heavy-duty diesel engines,” *Environ. Sci. Technol.*, vol.31, pp. 1144, 1997.

[88] R. L. McCormick, C. Tennant, R. R. Hayes, S. Black, A. Williams, J. Ireland, T. McDaniel, M. Frailey, and C. A. Sharp, “Regulated emissions from biodiesel tested in heavy-duty engines meeting 2004 emission standards,” *SAE 2005-01-2200*, 2005.

[89] F. Ponti, D. Moro, V. Ravaglioli, and G. Serra, “Common rail multi-jet diesel engine combustion development investigation for MFB50 on-board estimation,” *SAE 2010-01-2211*, 2010.

[90] J. B. Heywood, *Internal Combustion Engine Fundamentals*. McGraw-Hill, New York, 1988.

[91] J.H. Lee, and N. Lida, “Combustion of diesel spray injected into reacting atmosphere of propane-air homogeneous mixture,” International Journal of Engine Research, 2001. Vol.2, No. 1, pp. 69-80.

[92] C. Aligrot, J.C. Champoussin, N. Guerrassi, “A correlative model to predict autoignition delay of diesel fuels,” SAE Trans. 1997. 106(3): pp. 958-963.

[93] H.H. Wolfer, "Ignition lag in diesel engines," VDI-Forschungsheft 392, translated by Royal Aircraft Establishment, Aug. 1959, Farnborough Library No. 358, UDC 621-436.047.

[94] F.W. Stringer, A.E. Clarke, and J.S. Clarke, 1969, "The spontaneous ignition of hybrocarbon fuels in a flowing system," Proc. Inst. Mech. Eng., 184, Pt. 3J, 1969.

[95] N.A. Henein, and J.A. Bolt, "Correlatin of air charge temperature and ignition delay for several fuels in a diesel engine," SAE Paper No. 690252, 1969.

[96] H.O. Hardenberg, and F.W. Hase, "An empirical formula for computing the pressure rise delay of a fuel from its cetane number and from the relevant parameters of direct-injection diesel engines," SAE Paper No. 790493, 1979.

[97] Y. Itoh, N.A. Henein, "Determination of ignition delay in diesel engines from constant volume vessels data," Proceedings of ASME-ICE Spring Technical Conference, ASME, New York, ICE-Vol. 28-1, pp. 29-34, 1997.

[98] R.K. Barton, S.S. Lestz, and L.C. Duke, "Knock intensity as a function of engine rate of pressure change," SAE Paper No. 700061, 1970.

[99] S. Kim, and K. Min, "Detection of combustion start in the controlled auto ignition engine by wavelet transform of the engine block vibration signal," Meas. Sci. Technol. 19 085407, 2008.

[100] M. Jargenstedt, *Detection of the start of combustion using knock sensor signals*, Master's thesis, Link□ping University Vehicular Systems Dept. of Electrical Engineering, 2000.

[101] J. Chauvin, O. Grondin, E. Nguyen, and F. Guillemin, "Real-time combustion parameters estimation for HCCI-Diesel engine based on knock sensor measurement," Proceedings of the 17th World Congress, the international federation of automatic control, Seoul, Korea, July 6-11, 2008.

[102] C. Polonowski, V. Mathur, J. Naber, and J. Blough, "Accelerometer based sensing of combustion in a high speed HPCR diesel engine," SAE Paper 2006-01-0972, 2006.

[103] J.E. Dec, "Advanced compression-ignition engines-understanding the in-cylinder process," Proceedings of Combustion Institute, vol.32, pp. 2727-2742, 2009.

[104] A.D. Attebery, Investigating the effects of internally trapped residuals on the performance of homogeneous charge compression ignition (HCCI) engine, Master's thesis, Missouri University of Science and Technology, 2012.

[105] X. Chen, Y. Wang, I, Haskara, and G. Zhu, "Air-to-fuel ratio control with adaptive estimation of biofuel content for diesel engine LNT regeneration," American Control Conference, Jun. 27-29, 2012.

[106] L. Pickett, S. Kook, and T. Williams, “Visualization of diesel spray penetration, cool flame, ignition, high temperature combustion, and soot formation using high-speed imaging,” SAE Paper 2009-01- 0658, 2009.

[107] T. Katrasnik, F. Trenc, and S. Opresnik, “A new criterion to determine the start of combustion in diesel engines,” Journal of Engineering Gas Turbine Power, vol.128, pp. 928-933, 2006.

[108] C. Squib, H. Schock, T, Stuecken, M. Poort, K, Crayne, C. Gray, and F. Hamady, “A development of simultaneous infrared and visible imaging techniques with pressure data in an optically accessible diesel engine operating at part load with high EGR,” SAE Paper 2011-01-1395, 2011.

[109] M. Mittal, G. Zhu, and H. Schock, “Fast mass-fraction-burned calculation using the net pressure method for real-time applications,” Proceedings of the Institute of Mechanical Engineers, Part D: Journal of Automobile Engineering, pp 223:389, 2009.

[110] M.F.J. Brunt, and A.L. Emtage, “Evaluation of burn rate routines and analysis errors,” SAE Paper No. 970037, 1997.